
Analysis of magnetohydrodynamic instabilities in the
ASDEX Upgrade tokamak by frequency dependent
modelling of magnetic measurements

Magdalena Maria Bauer



München 2025

Analysis of magnetohydrodynamic instabilities in the
ASDEX Upgrade tokamak by frequency dependent
modelling of magnetic measurements

Magdalena Maria Bauer

Dissertation
an der Fakultät für Physik
der Ludwig-Maximilians-Universität
München

vorgelegt von
Magdalena Maria Bauer
aus Landshut

München, den 30.01.2025

Erstgutachter: Prof. Dr. Hartmut Zohm
Zweitgutachter: Prof. Dr. Piero Martin
Tag der mündlichen Prüfung: 28.03.2025

Zusammenfassung

Diese Arbeit beschäftigt sich mit der Analyse magnetohydrodynamischer (MHD) Instabilitäten in magnetisch eingeschlossenen Plasmen in der Tokamak-Konfiguration. In großen Tokamaks muss eine Disruption, d.h. ein plötzlicher Verlust der thermischen Energie und des Plasmastroms, vermieden oder zumindest abgemildert werden. Da Tearing-Moden, bei denen es sich um resistive MHD-Instabilitäten handelt, mit einer toroidalen Modenzahl $n = 1$ häufig an Disruptionen beteiligt sind, ist ihre Erkennung und Analyse sowohl für ein besseres Verständnis als auch für die Einleitung von Gegenmaßnahmen, die eine Störung abmildern oder vermeiden können, wichtig. Aufgrund der Toroidizität und Plasmaform können $n = 1$ Tearing-Moden mit unterschiedlichen poloiden Modenzahlen m koppeln und mit derselben Frequenz rotieren. Die Bestimmung der poloidalen Modenzusammensetzung solcher gekoppelter Tearing-Moden in Bezug auf Amplituden und Phasen erfordert magnetische Messungen an verschiedenen poloiden Positionen sowie ein Modell zur Berechnung des vorhergesagten magnetischen Störfeldes an der Spulenposition für einzelne poloidale Harmonische. Für rotierende Moden, bei denen induzierte Abschirmströme in den umgebenden leitenden Strukturen die Messungen beeinflussen, werden Mirnovspulen im Tokamak ASDEX Upgrade (AUG) verwendet, die (hauptsächlich) die poloidale Störfeldkomponente messen. Für gelockte Moden, d.h. Moden, die in Bezug auf das Vakuumgefäß nicht rotieren, sind integrierte Radialfeldmessungen notwendig, da die poloidale Störfeldkomponente nicht mit ausreichender Genauigkeit vom poloidalen Gleichgewichtsfeld unterschieden werden kann. Um eine kontinuierliche Modenanalyse durchführen zu können, sind daher magnetische Messungen verschiedener Spulentypen erforderlich, die durch das Modell konsistent beschrieben werden müssen. Dies wird im Niederfrequenzbereich gezeigt, in dem die meisten magnetischen Messungen in AUG verfügbar sind. Ein dreidimensionales FEM-Modell wird verwendet, um die erwarteten virtuellen magnetischen Messungen des Störfelds zu berechnen, das durch eine helixförmige Störstromdichte erzeugt wird, welche kraftfrei auf der resonanten Fläche fließt. Diese ist mit einer variierenden Dicke definiert, um den unterschiedlichen Abstand zwischen benachbarten magnetischen Flussflächen zu berücksichtigen. Relevante leitende Strukturen sind in dem Modell implementiert, während das Plasma – mit Ausnahme der resonanten Fläche – als Vakuum behandelt wird. Zusätzlich zum Einfluss des Vakuumgefäßes und des Passiven Stabilisierungsleiters (PSL) wird die Relevanz der Implementierung von Stützbrücken, welche der mechanischen Stabilisierung des PSLs dienen, und leitender Strukturen mit einer Verbindung zur Wand gezeigt. Durch die lineare Superposition der vorhergesagten magnetischen Messungen von einzelnen poloidalen Harmonischen, welche am besten mit den Messergebnissen übereinstimmt, ergeben sich Amplituden und Phasen der poloidalen Harmonischen. Die daraus resultierenden simulierten Mirnovmessungen zeigen eine hervorragende Übereinstimmung mit ihren Messwerten über einen weiten Frequenzbereich. Die Analyse von zwei Fällen, in denen die $m = 2$ und $m = 3$ Tearing-Moden entkoppelt sind, zeigt die Wichtigkeit poloidaler Seitenbänder mit $\Delta m = \pm 1$. Ferner wird die in einer früheren Arbeit gefundene Variation der Phasenbeziehung zwischen gekoppelten $m = 2$ und $m = 3$ Tearing-Moden von 0 bis π in Abhängigkeit vom Plasma- β bestätigt und die von der Theorie erwartete Phasenbeziehung von π zwischen dem poloidalen Seitenband $m = 1$ und der poloidalen Harmonischen $m = 2$ nachgewiesen. Eine konsistente Beschreibung der virtuellen Spulenergebnisse verschiedener Typen wird durch die Übereinstimmung der simulierten Messungen von Spulen, die das radiale Störfeld messen, mit ihren gemessenen Werten gezeigt, wobei die Amplituden und Phasen der poloidalen Harmonischen aus den Mirnovspulen bestimmt wurden.

Abstract

This thesis presents an analysis of magnetohydrodynamic (MHD) instabilities in magnetically confined plasmas in the tokamak configuration. In large tokamaks, a disruption, i.e. a sudden loss of the plasma thermal energy and current, has to be avoided or at least mitigated. As tearing modes, which are resistive MHD instabilities, with a toroidal mode number $n = 1$ are often involved in disruptions, their detection and analysis is important for both a better understanding and the initiation of countermeasures that can mitigate or avoid a disruption. Owing to toroidicity and shaping, $n = 1$ tearing modes with different poloidal mode numbers m can couple and rotate at the same frequency. Determining the poloidal mode composition of such coupled tearing modes in terms of amplitudes and phases requires magnetic measurements at different poloidal positions and a model to calculate the predicted magnetic perturbation field at the coil position for a single poloidal harmonic. For rotating modes, where induced shielding currents in the surrounding conducting structures affect the measurements, Mirnov coils measuring (mainly) the poloidal perturbation field component are used in the ASDEX Upgrade (AUG) tokamak. For locked modes, i.e. modes that do not rotate with respect to the vacuum vessel, integrated radial field measurements are required as the poloidal perturbation field component cannot be distinguished from the poloidal equilibrium field with sufficient precision. Thus, for a continuous mode analysis, the magnetic measurements of different coil types are required and have to be consistently described by the model, which is proven in the low frequency range, where most of the magnetic measurements in AUG are available. We employ a three-dimensional FEM model to calculate the expected virtual magnetic measurements of the perturbation field produced by a helical perturbation current density flowing force-free on the resonant surface. This surface is defined with a varying thickness to account for the different distance between adjacent magnetic flux surfaces. Relevant conducting structures are implemented in the model, while the plasma around the resonant surface is treated as vacuum. We show the importance of including not only the vacuum vessel and the Passive Stabilisation Loop (PSL), but also the support bridges for mechanical stabilisation of the PSL and additional conducting structures with a connection to the wall. The linear superposition of the predicted magnetic measurements of single poloidal harmonics that best matches the measured results gives the amplitudes and phases of the individual poloidal harmonics. The resulting simulated Mirnov measurements show excellent agreement with their measured values over a wide frequency range. The analysis of two cases where the $m = 2$ and $m = 3$ tearing modes are decoupled shows the importance of considering poloidal sidebands with $\Delta m = \pm 1$. Moreover, the variation of the phase relation between coupled $m = 2$ and $m = 3$ tearing modes from 0 to π depending on the plasma β found in previous work is confirmed and a phase relation of π between the $m = 1$ poloidal sideband and the $m = 2$ poloidal harmonic, as expected by theory, is demonstrated. A consistent description of the virtual coils of different types is proven by the agreement of the simulated measurements of coils measuring the radial perturbation field, where the amplitudes and phases of the poloidal harmonics are determined from the Mirnov coils, with their measured values.

Contents

Zusammenfassung	i
Abstract	iii
1 Introduction	1
1.1 Nuclear fusion on earth	1
1.2 Magnetic confinement fusion	2
1.3 The tokamak principle	3
1.4 Disruptions and the role of tearing modes	5
1.5 Aim and content of this work	6
2 Physical background	7
2.1 The magnetohydrodynamic (MHD) equations	7
2.2 The energy principle of ideal MHD	9
2.3 Resistive MHD	10
2.4 The tearing mode: a resistive MHD instability	11
2.4.1 Tearing modes in a screw pinch	11
2.4.2 Tearing modes in a torus	19
2.4.3 Rotation, braking and locking of tearing modes	23
2.4.4 Influence of a conducting wall on the perturbation magnetic field of a rotating mode	24
2.4.5 Toroidal mode coupling	25
2.5 Role of tearing modes in regards to disruptions	26
2.6 Description of tearing modes in this work	26
3 Measurements of tearing modes	27
3.1 Electron cyclotron emission spectroscopy	27
3.2 Soft x-ray measurement	28
3.3 Magnetic measurements	30
3.3.1 Passive coils for mode detection	30
3.3.2 Passive coils in ASDEX Upgrade	31
3.4 Technical aspects	33
3.5 Necessity for modelling magnetic measurements	34

4	Simulating tearing modes and their measurements with the Finite Element Method (FEM)	37
4.1	Theory and formulation of FEM	37
4.1.1	General theory	37
4.1.2	FEM formulation used in this work	39
4.2	Model set-up in general	41
4.3	Magnetic measurements in a simplified toroidal device with wall	43
4.4	Model description: ASDEX Upgrade	45
4.4.1	Source region	45
4.4.2	Conducting regions	47
4.4.3	Virtual magnetic measurements	50
4.4.4	Influence of conducting structures	53
4.4.5	Influence of the position of the resonant surface	56
4.5	Determination of mode composition	57
4.5.1	Method and application	57
4.5.2	Agreement between simulated and measured Mirnov amplitudes and phases over a wide frequency range	60
4.6	Calibration for consistent description of all coil types	61
4.6.1	Correcting Mirnov with Ballooning coils	61
4.6.2	Optimization of free parameters: scan of R_{saddle} and σ_{vessel}	63
4.7	Possible extensions to the model	66
5	Mode composition with radial field coils	69
5.1	Theoretical distinguishability	69
5.2	Extension for locked modes	71
6	Application of the model	75
6.1	Characterisation of poloidal sidebands of tearing modes	75
6.2	Determination of mode composition for different β	79
6.3	Simultaneous application to Mirnov and radial field coils	83
7	Summary and outlook	87

A Appendix	91
A.1 Mirnov contour	91
A.2 Ballooning coil contour	92
A.3 Calculation of the B-coil area	93
Acronyms	95
Symbols	97
References	99
Acknowledgements	105

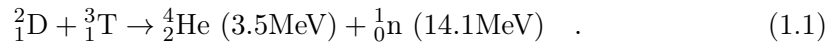
1 Introduction

"Freude am Schauen und Begreifen ist die schönste Gabe der Natur."
"The joy of looking and understanding is the most beautiful gift of nature."
Albert Einstein, (1879-1955)

This quote from Albert Einstein possibly refers to his formula of the equivalence of mass and energy, $E = mc^2$, formulated in the context of the theory of relativity [1]. This work is not about the theory of relativity, but about nuclear fusion research, which is also inspired by nature. The sun's energy originates from the conversion of four protons into a helium nucleus via multiple steps [2, 3]. The mass deficit of the reaction results in an energy release according to Einstein's formula $E = mc^2$. The aim of fusion research is to bring nuclear fusion to earth to convert mass into usable energy, following the example of the sun.

1.1 Nuclear fusion on earth

The most promising fusion reaction to be used for nuclear fusion on earth is the reaction of the nuclei of the hydrogen isotopes deuterium and tritium producing a helium nucleus and a neutron [4]



This reaction is highly advantageous because of its high reaction rate, which is about 24 orders of magnitude larger than the proton-proton reaction powering the sun [5]. The maximum of the cross section of this reaction occurs at energies in the order of 100 keV [4], which is relatively low compared to the gained energy of about 18 MeV. Accelerating deuterium and tritium beams to high energies and then colliding them does not produce a significant amount of energy because elastic Coulomb collisions with a much larger cross section compete with fusion collisions in this energy range. A solution to achieve a positive energy balance is to provide the energy via thermal energy of the particles and let them collide numerously without losing the energy. At thermal energies of more than 10 keV, matter is in the state of plasma, i.e. an ionised gas.

There are three concepts to confine a plasma at the required high temperatures: by gravity as in stars; by magnetic fields; and by inertial confinement. On earth, only the latter two options are possible. In order to obtain energy from the fusion reactions in thermal plasmas, the product of density n , temperature T and energy confinement time τ_E must exceed a temperature-dependent critical value $L_{\text{Lawson}}(T)$ [6]

$$nT\tau_E > \underbrace{\frac{12 T^2}{\langle \sigma v \rangle E_\alpha}}_{L_{\text{Lawson}}(T)} \quad (1.2)$$

where $\langle \sigma v \rangle$ is the temperature dependent D-T reaction rate and E_α is the energy of the charged helium nucleus that remains in the plasma. For magnetically confined D-T plasmas, typical reactor relevant temperatures are in the range of 10 to 20 keV, where $L_{\text{Lawson}}(T)$ is close to its minimum [7], and densities are usually chosen to be about 10^{20} to $2 \cdot 10^{20} \frac{1}{\text{m}^3}$ [8]. Consequently, the energy confinement timescale,

which is defined as the ratio of energy content to heating power and is a measure of the quality of the thermal insulation of the plasma, must be of the order of 5 s [8]. In inertial confinement fusion, which is not considered further in this work, a small pellet is heated resulting in the ablation of the outer layer, the recoil of which heats and compresses the inner part of the pellet. Thus, in inertial fusion, the densities are much higher and the energy confinement timescales are much shorter [9].

1.2 Magnetic confinement fusion

The magnetic confinement of a plasma is based on the fact that charged particles with a charge q_{el} and a velocity \mathbf{v} experience the Lorentz force $\mathbf{F}_L = q_{\text{el}} \mathbf{v} \times \mathbf{B}$ in a magnetic field \mathbf{B} . This results in a gyrating motion of electrons and positively charged ions (in different directions and with different gyration radii) around the magnetic field lines. In the first order, the charged particles are bound to the magnetic field lines, which indicates that ring-shaped magnetic field lines could confine a plasma. However, as will be shown below, a toroidal configuration with only a toroidal magnetic field, \mathbf{B}_ϕ , cannot confine the charged particles due to particle drifts [6]

$$\mathbf{v}_D = \frac{\mathbf{F} \times \mathbf{B}}{q_{\text{el}} B^2} \quad (1.3)$$

where \mathbf{F} is an additional force and B is the magnetic field strength. The torus coordinate system (r, θ, ϕ) and the cylinder coordinate system (R, z, ϕ) are introduced in figure 1.1. The magnetic field strength in a torus with \mathbf{B}_ϕ is mainly given by $B = B_0 R_0/R$, where B_0 and R_0 are the magnetic field strength and the major radius, R , at the magnetic axis at $r = 0$. Thus, there is a toroidal magnetic field gradient in negative major radial direction, with a higher field on the inner side (High Field Side (HFS)) and a lower field on the outer side (Low Field Side (LFS)) of the torus. This leads to a charge-dependent drift $\mathbf{v}_{D,\nabla B} \sim 1/q_{\text{el}} \mathbf{B} \times \nabla B$ in positive (negative) z -direction for $q_{\text{el}} > 0$ ($q_{\text{el}} < 0$) for the direction of \mathbf{B}_ϕ in figure 1.1 [10]. The charge separation generates an electric field, which consequently causes all charged particles to drift outwards, with $\mathbf{v}_{D,E} \sim \mathbf{E} \times \mathbf{B}$ [10]. Thus, the plasma cannot be confined by a pure toroidal magnetic field.

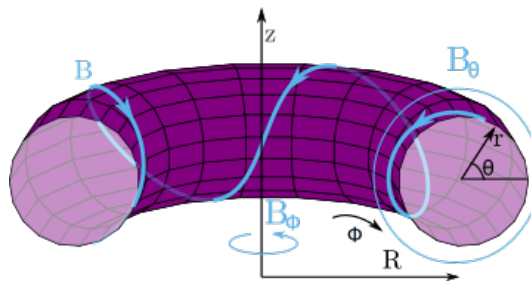


Figure 1.1: Direction of the toroidal magnetic field, \mathbf{B}_ϕ , and the poloidal magnetic field, \mathbf{B}_θ , resulting in helical magnetic field lines (light blue) on a particular magnetic flux surface (purple). The torus coordinates (r, θ, ϕ) , where r is the minor radius, θ the poloidal and ϕ the toroidal angle, and the cylinder coordinates (R, z, ϕ) , where R is the major radius, are introduced. (figure adapted from [11])

The solution to avoid particle loss due to the outward drift is to introduce a poloidal field component, \mathbf{B}_θ , resulting in helically twisted field lines, shown in figure 1.1. The surfaces on which the magnetic field lines lie (cf. purple surface in figure 1.1) are nested within each other, such that the drifts due to the inhomogeneity of the

magnetic field do not lead to a significant charge separation and thus not to the outward drift (cf. chapter 2 in [12]). $\mathbf{v}_{D,\nabla B}$ is still directed in positive (negative) z -direction, but a positively (negatively) charged particle in the upper (lower) half of the torus will now drift to a magnetic flux surface with a larger r and, once in the lower (upper) part of the torus, will drift back to the original flux surface.

Two promising concepts to confine the plasma in a toroidal device are the tokamak and the stellarator concept. In a tokamak, the poloidal magnetic field is generated by a toroidal plasma current, I_p , induced by a transformer coil with the plasma as secondary winding. In a stellarator, the twisted magnetic field is solely produced by external magnetic field coils with complicated three-dimensional shapes. Owing to the more challenging design and construction of a stellarator compared to a tokamak, research on the tokamak was carried out more extensively in the past and therefore has a development advantage (cf. [7]). This work is based on experiments on the tokamak ASDEX Upgrade (AUG).¹ Thus, we will focus on the tokamak principle in the following.

1.3 The tokamak principle

The word 'tokamak' is a Russian acronym for the expression 'toroidal chamber with magnetic coils' (cf. e.g. [12]). Figure 1.2 shows the coil system, the plasma current and the resulting magnetic field of a tokamak. The toroidal field is created by planar coils around the plasma, whereas the poloidal magnetic field is generated by a toroidal plasma current. In order to balance the hoop force of the plasma, that wants to expand the plasma ring, a vertical magnetic field is created by poloidal field coils leading to a shift of the magnetic flux surfaces, called the Shafranov shift [13]. This results in magnetic flux surfaces with a smaller distance on the LFS which is even more pronounced at higher plasma pressure. The poloidal field coils are also used to fix the plasma position and to study different plasma shapes. Several poloidal field coils are installed in AUG. Since an elliptical plasma cross section has improved stability and confinement properties [14], the poloidal cross-sections of experimental plasmas are usually chosen to be non-circular (cf. figure 1.3).

A typical poloidal cross section of the plasma in AUG is presented in figure 1.3 on the left. All magnetic field lines on a magnetic flux surface, some of which are shown in grey, share the same helicity. The separatrix, which separates the confined plasma from the so-called Scrape-Off Layer (SOL), is shown in black. The helicity of the field lines on a specific flux surface is expressed by the safety factor

$$q = \frac{\text{number of toroidal turns}}{\text{number of poloidal turns}} \quad , \quad (1.4)$$

and depends on the minor radius r . It is common to introduce a normalised radial coordinate which serves as flux surface label. Here, we use ρ_{pol} which is defined as

$$\rho_{\text{pol}} = \sqrt{\frac{\Psi - \Psi_{\text{axis}}}{\Psi_{\text{sep}} - \Psi_{\text{axis}}}} \quad (1.5)$$

where $\Psi = \int_{S_{\text{pol}}} \mathbf{B} \cdot \mathbf{dS}$ denotes the poloidal magnetic flux through an area S_{pol} perpendicular to the poloidal direction, which is indicated in figure 1.3. Ψ , Ψ_{sep} and

¹The AUG tokamak is an experiment that operates without tritium in the plasma due to nuclear safety restrictions. The aim of the scientific program is to investigate the physical basis for future fusion devices, which are expected to gain energy from the reaction 1.1.

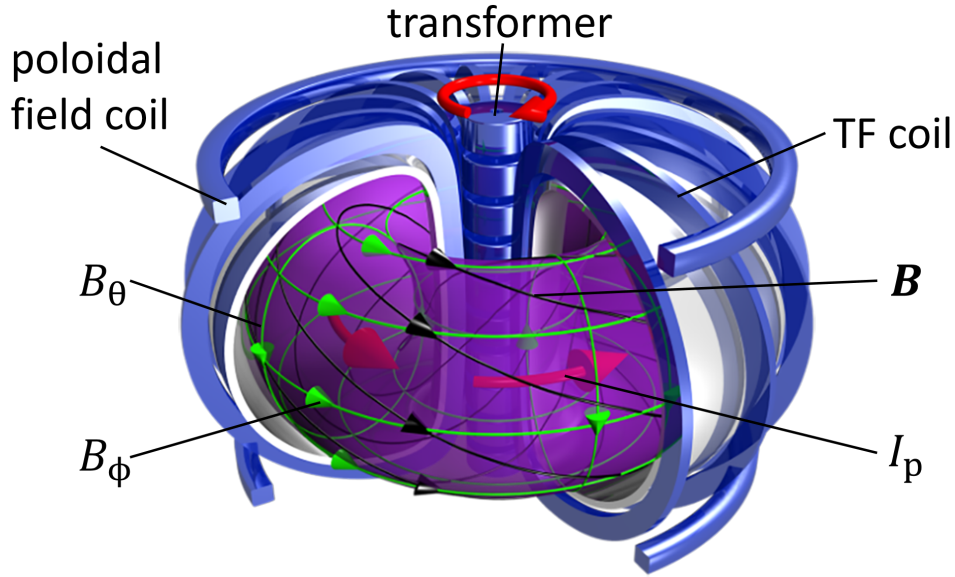


Figure 1.2: The plasma in purple is confined by using the tokamak principle: The toroidal magnetic field, B_ϕ , is created by the Toroidal Field (TF) coils (blue coils around the plasma). The poloidal magnetic field, B_θ , is generated by the toroidal plasma current, I_p , which is driven by an electric field induced by the transformer in the middle of the torus (blue coils with red arrow above). The combination of the toroidal and poloidal field results in helical field lines indicated in black. The poloidal field coils above and below the plasma complete the magnetic field configuration. (*source:* MPI for Plasma Physics, *graphic:* Christian Brandt, adapted)

Ψ_{axis} are called the poloidal flux at a particular flux surface, the separatrix and the magnetic axis, respectively. The normalisation is such that $\rho_{\text{pol}} = 0$ at the magnetic axis, $\rho_{\text{pol}} = 1$ at the separatrix and $\rho_{\text{pol}} > 1$ outside the separatrix in the SOL. [13, 14]

A typical q profile as a function of ρ_{pol} is shown in 1.3 on the right. The safety factor can be either a rational number, i.e. the field line closes in on itself after some toroidal turns, or an irrational number, i.e. the field line never closes in on itself. The magnetic flux surfaces, where q is a rational number, are prone to instabilities and are called resonant surfaces.

A tokamak has two major conceptual disadvantages compared to stellarators. Firstly, it is usually operated in pulses, since the plasma current relies on induction of the transformer. Advanced scenarios to make the discharges stationary by replacing the transformer induced plasma current are the subject of current research (cf. e.g. [15]). Secondly, a so-called disruption can occur, i.e. a sudden loss of the plasma current, which terminates the discharge. The consequences are high thermal and mechanical loads on the device structures (cf. section 1.4). In order to avoid disruptions in future fusion devices, it is important to study the instabilities that are involved in disruptions.

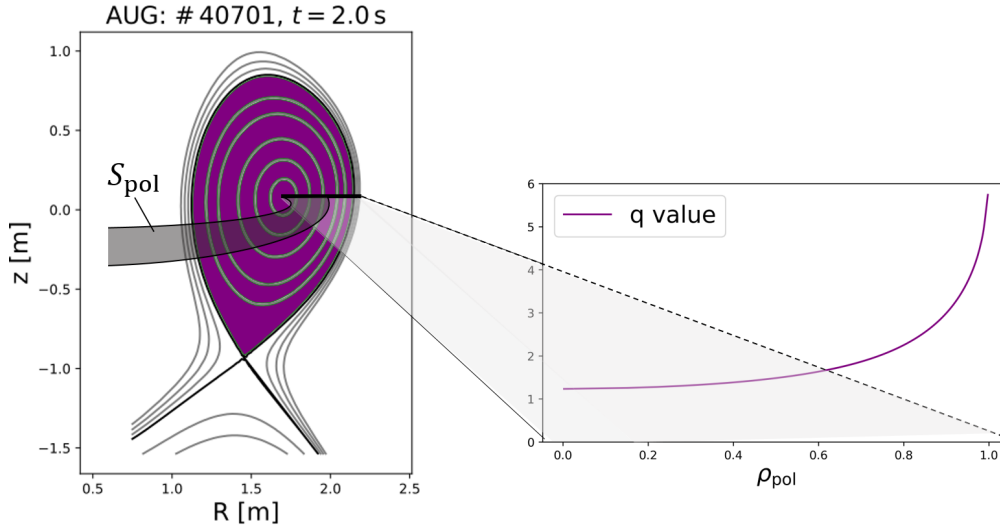


Figure 1.3: Equilibrium reconstruction of a standard discharge 40701 at $t = 2.0$ s. In the poloidal cross section (left), the plasma is marked in purple, the separatrix is shown in black and other magnetic flux surfaces are shown in grey. A part of an area S_{pol} for defining the magnetic flux surface label, ρ_{pol} , is indicated in dark grey. The corresponding q -profile is shown on the right.

1.4 Disruptions and the role of tearing modes

Disruptions can severely damage future reactor machines and are therefore intolerable in large devices with burning DT plasmas. A disruption usually occurs due to the loss of plasma confinement, the thermal quench, which is a rapid decrease in thermal energy, and the current quench. The plasma current cannot be sustained due to the decreased plasma conductivity, σ_{plasma} , which increases with T_e , with $\sigma_{\text{plasma}} \sim T_e^{3/2}$. In addition to the thermal loads of the no longer confined hot plasma, the sudden loss of the plasma current leads to strong forces due to the induced current densities in the conducting structures. Runaway electrons, i.e. relativistic electrons with an energy of a few tens of MeV [16], accelerated in the large resulting toroidal electric field, can also occur during a disruption with a high potential to damage the components on impact. The energy dissipated to the wall is approximated to scale with L^3 , where L is the typical size scale of the device, i.e. disruptions become more dangerous in larger devices with higher plasma currents and magnetic fields. (cf. chapter 7 in [12])

To avoid disruptions in future fusion reactors, it is important to study the instabilities that cause disruptions in smaller experiments like AUG where disruptions are tolerable. Tearing modes, resistive magnetohydrodynamic (MHD) instabilities in tokamak plasmas (cf. chapter 2), are often involved in disruptions (cf. e.g. [17, 18]). They lead to a confinement degradation [19], which is even stronger for coupled modes [20], i.e. modes that rotate with a fixed phase relation. Large rotating modes can be slowed down by the electromagnetic interaction with the conducting vacuum vessel surrounding the plasma and finally stop rotating with respect to the vessel, as described in [13] and [21]. These non-rotating modes are called locked modes and are found to be especially dangerous in regards to triggering disruptions.

In order to detect and analyse tearing modes, passive coils are installed in AUG that measure the magnetic fluctuations associated with these modes. With multiple

passive coils at different locations, it is possible to infer and study the mode structure of tearing modes using a model that calculates the expected measurements at the coil positions for a set of perturbation currents.

1.5 Aim and content of this work

The detection and characterisation of $n = 1$ tearing modes in terms of the poloidal mode number composition is important for a physical understanding and for initiating appropriate countermeasures to avoid or mitigate a confinement degradation and a disruption. In order to infer the poloidal mode number composition from magnetic measurements, a model simulating the predicted perturbation magnetic field is required, with different challenges arising for rotating and locked modes, i.e. non-rotating modes with respect to the laboratory frame. Rotating modes induce shielding currents in the surrounding conducting structures, which affect the magnetic measurements, while locked modes require the integrated measurements of the radial field component, as the poloidal component of the perturbation magnetic field cannot be distinguished from the poloidal equilibrium magnetic field with sufficient accuracy. For rotating modes, Mirnov coils are used, which measure the poloidal magnetic field component and thus cannot be used for locked modes. However, most radial field measurements are not suitable for use in the rotating phase due to attenuation by nearby shielding currents. Thus, for a continuous description of the mode structure of rotating and locked modes, all coil types have to be used and therefore modelled consistently. This requires a comparison in the low frequency range, where measurements of all coil types are available and where shielding currents are important.

Owing to the toroidal and shaped geometry of the resonant surface, where the tearing mode is located, and the surrounding conducting structures, an analytical formula, as derived in [13], using the cylindrical approximation is not sufficient for an accurate frequency dependent description of magnetic measurements near conducting structures. The aim of this work is to provide a tool to derive the poloidal mode composition from magnetic measurements for all mode frequencies f , including $f = 0$. This work provides a description of this model, a discussion of the steps taken to achieve a consistent description of the magnetic measurements of the different coil types, and the application of the model.

An introduction to (resistive) MHD, tearing modes and their role regarding disruptions is given in chapter 2. Chapter 3 contains a description of different methods for measuring tearing modes, in particular magnetic measurements. The model required to calculate the expected magnetic measurements uses the Finite Element Method (FEM) and is described in chapter 4 together with the mechanism to infer the poloidal mode structure. As for locked modes only radial measurements at far fewer poloidal positions are available, the theoretical distinguishability of modes with different poloidal mode numbers with these radial coils is discussed in chapter 5. An algorithm for determining the poloidal mode structure of locked modes is also presented. In chapter 6 an analysis of the relation between the dominant poloidal harmonics and their poloidal sidebands is presented and the phase relation between coupled modes analysed in [22] is confirmed. Moreover, it is shown that a consistent description of all coil types is achieved, as the resulting amplitudes and phases of modes with different poloidal mode numbers determined from the Mirnov coils yield simulated measurements that agree with their measured amplitudes and phases for the different coil types. A summary and outlook can be found in chapter 7.

2 Physical background

This section will provide a theoretical description of the plasma, tearing mode instabilities and their relation to disruptions. It is mainly based on [13].

2.1 The magnetohydrodynamic (MHD) equations

An exact description of the many-body system of the plasma in a magnetic field would require solving the equations of motion for all particles simultaneously. Since these equations are coupled by the interactions between the particles, this would mean that a coupled system of about 10^{20} equations per cubic metre must be solved. The kinetic theory statistically describes the system of a magnetised plasma by introducing the distribution function f_α for particle species α in six-dimensional space $d^3x d^3v$ where f_α is the likelihood to find a particle of species α with velocity \mathbf{v} at position \mathbf{x} . To get a three-dimensional fluid description of the system, the kinetic equations can be averaged over the velocity space assuming the distribution function is close to a Maxwellian.

The description of the plasma as a fluid is similar to the hydrodynamic equations, additionally taking into account magnetic fields \mathbf{B} and electric fields \mathbf{E} . The fluid description is only valid if the mean free path of the particles is much shorter than the length scale of the system L , which is not the case along the magnetic field lines, but perpendicular to them. In addition, the radius of the gyrating motion of the particles, the Larmor radius $r_L \sim \frac{\sqrt{mT}}{B}$ where m is the mass and T is the temperature, has to be small compared to L . To obtain a one-fluid description of a plasma consisting of electrons and positively charged ions, the mass density is defined as $\rho = m_i n_i + m_e n_e \approx m_i n_i$, the centre of mass velocity as $\mathbf{v} = 1/\rho (m_i n_i \mathbf{u}_i + m_e n_e \mathbf{u}_e) \approx \mathbf{u}_i$ and the current density as $\mathbf{j} = e n (\mathbf{u}_i - \mathbf{u}_e)$. The subscript 'i' refers to the positively charged ions, the subscript 'e' to the electrons. The variable n is the density, and quasi-neutrality is assumed, i.e. $n_e = n_i = n$ for singly charged ions. The velocities of the ions and electrons are denoted as \mathbf{u} and e is the elementary charge.

The resulting one-fluid MHD equations are the continuity equation

$$\frac{\partial \rho}{\partial t} + \nabla \cdot (\rho \mathbf{v}) = 0 \quad , \quad (2.1)$$

the force balance equation

$$\rho \left(\frac{\partial \mathbf{v}}{\partial t} + (\mathbf{v} \cdot \nabla) \mathbf{v} \right) = -\nabla \cdot \mathbf{P} + \mathbf{j} \times \mathbf{B} \quad , \quad (2.2)$$

where $\mathbf{P} = \mathbf{P}_i + \mathbf{P}_e$ is the total pressure tensor, and Ohm's law

$$\mathbf{E} + \mathbf{v} \times \mathbf{B} = \frac{1}{\sigma} \mathbf{j} \quad . \quad (2.3)$$

The Hall term, $\frac{\mathbf{j} \times \mathbf{B} - \nabla p_e}{en_e}$, and the expression $\frac{m_e}{e} \frac{d\mathbf{u}_e}{dt}$ in equation 2.3 have been neglected here. The validity of this approximation is discussed in [13] and [14].

To get a closed system of equations, the adiabatic equation

$$\frac{d}{dt} \left(\frac{p}{\rho^\gamma} \right) = 0 \quad , \quad (2.4)$$

is used, where γ is the adiabatic coefficient and \mathbf{P} is assumed to be a scalar.

Together with the Maxwell's equations, namely Faraday's law

$$-\frac{\partial \mathbf{B}}{\partial t} = \nabla \times \mathbf{E} \quad , \quad (2.5)$$

the absence of divergence of the magnetic field

$$\nabla \cdot \mathbf{B} = 0 \quad , \quad (2.6)$$

and Ampère's law, neglecting the displacement current ($\frac{1}{c^2} \frac{\partial \mathbf{E}}{\partial t}$) due to velocities $v \ll c$ (cf. [14]),

$$\nabla \times \mathbf{B} = \mu_0 \mathbf{j} \quad , \quad (2.7)$$

a complete description of the plasma as a single fluid is obtained.

A plasma equilibrium state, that is $\frac{\partial}{\partial t} = 0$, assuming $\mathbf{v} = 0$ and an isotropic pressure, is derived from the force balance equation 2.2:

$$\mathbf{j} \times \mathbf{B} = \nabla p \quad . \quad (2.8)$$

Constructing the dot product with \mathbf{B} gives

$$\underbrace{\mathbf{B} \cdot (\mathbf{j} \times \mathbf{B})}_{=0} = \mathbf{B} \cdot \nabla p \quad , \quad (2.9)$$

which means that lines of constant pressure lie on surfaces of magnetic field lines and vice versa. The dot product of equation 2.8 with \mathbf{j} gives that the lines of \mathbf{j} also lie on surfaces of constant pressure and magnetic flux in the equilibrium state. By expressing the vector quantities in equation 2.8 by fluxes (cf. definition of S_{pol} in figure 1.3), a differential equation for the poloidal flux Ψ , called the Grad-Shafranov equation (cf. e.g. [13, 12]), can be formulated for describing a toroidally symmetric equilibrium. In cylindrical coordinates the Grad-Shafranov equation is

$$R \frac{\partial}{\partial R} \left(\frac{1}{R} \frac{\partial \Psi}{\partial R} \right) + \frac{\partial^2 \Psi}{\partial z^2} = -\mu_0 (2\pi R)^2 p' - \mu_0^2 I'_{\text{pol}} I_{\text{pol}} \quad , \quad (2.10)$$

where derivatives with respect to Ψ are represented by a prime and I_{pol} is the poloidal current.

Moreover, the MHD equations allow to study the stability of the system and to predict the occurrence of MHD instabilities which will be discussed in the following sections for ideal (section 2.2) and resistive MHD (section 2.3). In ideal MHD, an important approximation is made: Considering the high electrical conductivity ($\sigma_{\text{plasma}} \sim T_e^{3/2}$) of a hot fusion plasma, the resistivity $\eta_{\text{plasma}} = 1/\sigma_{\text{plasma}}$ of the plasma is neglected, i.e. $\sigma_{\text{plasma}} \rightarrow \infty$. Hence, Ohm's law (equation 2.3) simplifies to $\mathbf{E} + \mathbf{v} \times \mathbf{B} = 0$ in ideal MHD. This implies magnetic flux conservation through a contour moving with the plasma, as derived in section 1.1.2 of [13], which means that in ideal MHD, field lines cannot break and reconnect. In contrast to ideal MHD, non-ideal or resistive MHD takes the plasma resistivity into account, which allows magnetic field lines to reconnect.

The approximation of an ideally conducting fluid is reasonable, if the order of magnitude of the term $|\mathbf{v} \times \mathbf{B}|$ is much larger than $|\frac{1}{\sigma} \mathbf{j}|$ (cf. equation 2.3). Using Ampère's law (equation 2.7) and a typical length scale L , the condition for an ideal treatment of the plasma results in

$$vB \gg \frac{1}{\mu_0 \sigma} \frac{B}{L} \quad , \quad (2.11)$$

which can be reformulated as

$$L/v \ll \mu_0 \sigma L^2 \quad . \quad (2.12)$$

Thus, ideal MHD is valid for processes with a timescale $\tau = L/v$ that is much shorter than the resistive timescale

$$\tau_R = \mu_0 \sigma L^2 \quad . \quad (2.13)$$

The Alfvén timescale $\tau_A = L/v_A$, which is of the order of a few μs in typical magnetically confined fusion plasmas, is the typical timescale of ideal MHD phenomena. The Alfvén velocity v_A related to this timescale is derived in section 2.2 (cf. equation 2.20). The ratio between the resistive and the Alfvén timescales is defined as the Lundquist number

$$S = \frac{\tau_R}{\tau_A} \approx \mu_0 \sigma L v_A \quad . \quad (2.14)$$

2.2 The energy principle of ideal MHD

In order to analyse the linear stability in ideal MHD, the ideal MHD equations are linearised and the problem is reformulated to investigate different drives for instabilities. A brief overview of this concept is given here, for a detailed derivation, the reader is referred to [13] or [12].

All fluid quantities, f , are described by an equilibrium quantity (subscript 0), which fulfills the stationary MHD equations, and a small perturbation (subscript 1) much smaller than the equilibrium quantity:

$$f = f_0 + f_1 \text{ with } f_1 \ll f_0 \quad . \quad (2.15)$$

This labelling is retained in the following sections. The displacement vector $\boldsymbol{\xi}$, which is also a perturbation quantity, is introduced as

$$\frac{d\boldsymbol{\xi}}{dt} = \mathbf{v}_1 \quad . \quad (2.16)$$

Inserting ansatz 2.15 for all fluid quantities into the MHD equations and neglecting quadratic and higher order terms of the perturbation quantities, the linearised ideal MHD equations are obtained. The linearised continuity equation (cf. equation 2.1) reads

$$\frac{\partial \rho_1}{\partial t} + \nabla \cdot (\rho_0 \mathbf{v}_1) = 0 \quad , \quad (2.17)$$

the linearised adiabatic equation (cf. equation 2.4) is

$$\frac{\partial p_1}{\partial t} + p_0 \gamma \nabla \cdot \mathbf{v}_1 + \mathbf{v}_1 \cdot \nabla p_0 = 0 \quad . \quad (2.18)$$

The combination of Faraday's (equation 2.5) and Ohm's law (equation 2.3) yields

$$\frac{\partial \mathbf{B}_1}{\partial t} = \nabla \times (\mathbf{v}_1 \times \mathbf{B}_0) \quad . \quad (2.19)$$

Equation 2.19 can be reformulated using a vector identity and inserted into the linearised force equation to obtain a wave equation from which the Alfvén velocity

$$v_A = \frac{B_0}{\sqrt{\mu_0 \rho_0}} \quad (2.20)$$

can be inferred.

Integration of the equations 2.17 to 2.19 gives equations that depend on $\boldsymbol{\xi}$, e.g. the integrated equation 2.19 is $\mathbf{B}_1 = \nabla \times (\boldsymbol{\xi} \times \mathbf{B}_0)$. Consequently, the force balance equation (cf. equation 2.2) can be written as

$$\rho_0 \frac{\partial^2 \boldsymbol{\xi}}{\partial t^2} = \mathbf{F}(\boldsymbol{\xi}) \quad (2.21)$$

with the force operator \mathbf{F} that only depends on the displacement $\boldsymbol{\xi}$ and equilibrium quantities. Using the ansatz $\boldsymbol{\xi}(\mathbf{x}, t) = \boldsymbol{\xi}(\mathbf{x}) e^{-i\omega t}$ equation 2.21 can be written as an eigenvalue problem

$$-\omega^2 \rho_0 \boldsymbol{\xi} = \mathbf{F}(\boldsymbol{\xi}) \quad (2.22)$$

which is stable for $\omega^2 > 0$ and unstable for $\omega^2 < 0$.² The stability criterion is then formulated using the so-called energy principle of ideal MHD by multiplication with the complex conjugate of the displacement $\boldsymbol{\xi}^*$, which takes the role of a test function, and integration over the volume. The potential energy

$$\delta W = \omega^2 / 2 \int \rho_0 |\boldsymbol{\xi}|^2 dV = \omega^2 K \quad , \quad (2.23)$$

where K is related to the kinetic energy, can now be used to investigate the stability: $\delta W > 0$ implies linear stability whereas $\delta W < 0$ describes an unstable system. The rearrangement of the terms in δW into an 'intuitive' form [23] allows the identification of terms that can be negative and thus drive instabilities, namely the pressure gradient drive and the current density drive. This gives rise to ideal MHD instabilities like current density driven kink modes or pressure gradient driven ballooning modes. However, the limit of the maximum achievable pressure in a tokamak is often set by resistive MHD instabilities already at lower pressure. It is common to express the average pressure as plasma β , which is the ratio of the average plasma pressure to magnetic pressure

$$\beta = \frac{\langle p \rangle}{\langle B^2 \rangle / 2\mu_0} \quad . \quad (2.24)$$

2.3 Resistive MHD

As previously discussed when deriving the resistive timescale (equation 2.13), it is necessary to include the effects of resistivity, if $|\frac{1}{\sigma} \mathbf{j}|$ is comparable to $|\mathbf{v} \times \mathbf{B}|$. Using Ampère's law (equation 2.7), this criterion is reformulated in reference to hydrodynamics: Resistive effects have to be included if the magnetic Reynold's number

$$\text{Re}_M := \mu_0 \sigma L v \approx \frac{|\mathbf{v} \times \mathbf{B}|}{\frac{1}{\sigma \mu_0} |\nabla \times \mathbf{B}|} \quad (2.25)$$

is small [13].

Compared to ideal MHD, when including the finite plasma resistivity, equation 2.19 becomes

$$\frac{\partial \mathbf{B}_1}{\partial t} = \nabla \times \left(\mathbf{v}_1 \times \mathbf{B}_0 - \frac{1}{\sigma} \mathbf{j}_1 \right) \quad . \quad (2.26)$$

²An instability proportional to $e^{-i\omega t}$ oscillates around the initial position when ω is a real value and is therefore stable, while an exponentially growing solution exists when ω is an imaginary value (unstable situation).

Hence, in resistive MHD, the time-evolution of the perturbation magnetic field is explicitly affected by the perturbation current density. Resistive corrections to the energy functional are derived and discussed in [24].

As mentioned in section 2.1, resistive MHD becomes important for timescales comparable to the resistive timescale τ_R (cf. equation 2.13), which is in the order of seconds for typical parameters in a magnetically confined fusion plasma. Since this is about 6 orders of magnitude slower than the Alfvén timescale, at first glance it looks as if resistive MHD instabilities do not play a role. However, since $\tau_R \sim L^2$, the resistive timescale becomes much shorter in thin layers, e.g. around rational surfaces, where the field line closes in on itself after a few toroidal turns. This allows resistive instabilities to develop at such layer, while the surrounding plasma can be treated ideally.

While the magnetic field topology is conserved in ideal MHD, the magnetic field lines can tear and reconnect in resistive MHD if this is energetically favourable. As their name suggests, tearing modes are such resistive instabilities involving the tearing and reconnection of magnetic field lines.

2.4 The tearing mode: a resistive MHD instability

The resistive MHD instability 'tearing mode' is driven by radial current and pressure gradients in the plasma and changes the magnetic field topology: Magnetic field lines are torn apart, hence the name 'tearing', and reconnected forming so-called magnetic islands [25]. A classical tearing mode, driven by a current density gradient, is at first examined in a so-called screw pinch. The results are then applied to a tokamak plasma, where also pressure driven Neoclassical Tearing Modes (NTM) become important.

2.4.1 Tearing modes in a screw pinch

First, the analytically describable periodic screw pinch is considered, which can be seen as a 'straight tokamak'. A screw pinch defines a cylindrical plasma with a plasma current, I_z , and a constant magnetic field, B_z , in z -direction. The plasma current produces a poloidal magnetic field, B_θ , resulting – together with B_z – in helical magnetic field lines. By introducing a periodicity in z with a period of $2\pi R_0$, the periodic screw pinch is similar to a tokamak with the magnetic axis at $R = R_0$ and a toroidal angle $R_0\phi$ instead of the z -direction, so the term 'toroidal' is also used for the periodic cylinder in this section. However, effects of toroidal field curvature, which are especially important for pressure driven modes, are neglected in the screw pinch.

As introduced in section 1.3, the safety factor q describes the helicity of the magnetic field lines, which is

$$q = \frac{r}{R_0} \frac{B_z}{B_\theta(r)} \quad (2.27)$$

in a screw pinch. Generally, an instability in a screw pinch is assumed to extend along the magnetic field lines such that an instability described by the poloidal and toroidal mode numbers m and n , e.g. a (m,n) tearing mode, is located at the resonant magnetic flux surface with a safety factor $q_s = m/n$.³ A typical q profile ranges from

³Although the variables m and n were introduced as mass and density for the derivation of the MHD equations (cf. section 2.1), in the following m and n always refer to the mode numbers.

$q = 1$ at the magnetic axis to $q = 5$ at the plasma edge (q where 95 % of the poloidal flux through the last closed magnetic flux surface is contained, cf. figure 1.3), with the lowest m and n being the most unstable. The spatial structure of a perturbation of an equilibrium quantity A_0 is expressed here as

$$A_1 = \hat{A}_1(r) e^{i(m\theta - n\frac{z}{R_0})} \quad , \quad (2.28)$$

where $\hat{A}_1(r)$ is the amplitude of the perturbation.

With finite resistivity, a perturbation of the magnetic field \mathbf{B}_1 , e.g. produced by a current density perturbation, \mathbf{j}_1 , can lead to the reconnection of magnetic field lines. This is illustrated in figure 2.1, where the equilibrium magnetic field, \mathbf{B}_0 , is directed in different directions inside and outside the layer where \mathbf{j}_1 flows. The perturbation magnetic field, \mathbf{B}_1 , strengthens (weakens) \mathbf{B}_0 at the position where \mathbf{j}_1 is directed into (out of) the plane, leading to the formation of magnetic islands if this is energetically favorable. In a (straight) tokamak, \mathbf{B}_0 is not oriented in different directions inside and outside the resonant layer, but the helicity changes across the resonant surface due to the shear of \mathbf{B}_0 according to $q(r)$.

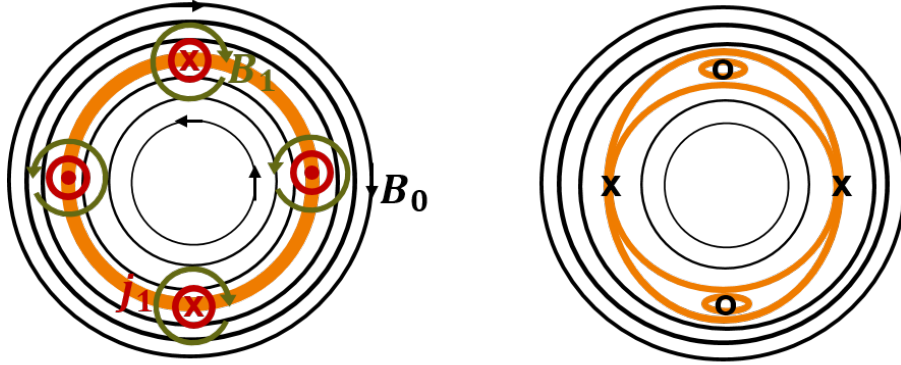


Figure 2.1: Illustration of the formation of magnetic islands with an equilibrium magnetic field, \mathbf{B}_0 , directed in different directions inside and outside the resonant surface (orange): A perturbation current density, \mathbf{j}_1 (red), flowing out of and into the plane produces a perturbation magnetic field, \mathbf{B}_1 (olive green), so that the field line topology around this layer is changed and magnetic islands with X- and O-points are formed. In this cartoon, only the magnetic field lines at the layer are changed, while in reality the magnetic field lines inside and outside the layer also change, cf. figure 2.2 for a calculated magnetic island structure.

To obtain a situation in analogy to figure 2.1, the transformation is made to a helical coordinate system with the helical angle $\zeta = (m\theta - n\frac{z}{R_0})$ following the field lines on the resonant $q = m/n$ surface. The coordinate system (marked with *) is chosen such that B_θ^* vanishes at the resonant surface q_s (cf. [6, 13]):

$$B_\theta^* = B_\theta \left(1 - \frac{q(r)}{q_s}\right) \quad . \quad (2.29)$$

Since ζ is now an ignorable coordinate, the problem can be formulated in two dimensions and the divergence-free magnetic field can be expressed by the helical flux function Ψ^* where

$$B_\theta^* = -\frac{\partial \Psi^*}{\partial r} \quad (2.30)$$

$$B_r^* = \frac{1}{r} \frac{\partial \Psi^*}{\partial \theta} = \frac{im}{r} \Psi_1^* \quad , \quad (2.31)$$

using the complex perturbed helical flux $\Psi_1^* = \hat{\Psi}_1^*(r) e^{i(m\theta - n\frac{z}{R_0})}$. Note that B_r^* , which is directly related to Ψ_1^* , is a pure perturbation quantity since B_0 has no radial component.

In order to get an equation for Ψ_1^* outside the resonant layer of thickness δ , where ideal MHD can be applied, the energy principle of ideal MHD (cf. section 2.2) is used to find $\delta W = 0$ in the approximation of negligible β . This gives an equation for the radial displacement ξ_r which can be related to Ψ_1^* via equation 2.19 and 2.16. After some algebra [13], the tearing mode equation reads

$$\Delta \Psi_1^* - \frac{\mu_0 \frac{dj_{0,z}}{dr}}{B_{0,\theta} (1 - q(r)\frac{n}{m})} \Psi_1^* = 0 \quad , \quad (2.32)$$

describing the plasma equilibrium around the resonant surface under the influence of Ψ_1^* . Directly at the resonant surface q_s , the tearing mode equation is singular and diverges.

To obtain a solution for the helical flux $\Psi^* = \Psi_0^* + \Psi_1^*$, the equilibrium helical flux Ψ_0^* and the perturbed helical flux Ψ_1^* have to be calculated numerically for an equilibrium current profile using equation 2.30 and the tearing mode equation 2.32. For an analytical solution of Ψ^* we can use a simple ansatz for Ψ_0^* and Ψ_1^* , which replaces the current sheet at $r = r_s$ in figure 2.1. A Taylor expansion of the equilibrium flux Ψ_0^* is formulated with $\Psi_0^*(r_s)$ set to 0 and $\frac{\partial \Psi_0^*}{\partial r} \Big|_{r=r_s} = 0$ since $B_{0,\theta}(r = r_s) = 0$. The remaining third term of the Taylor expansion describes a parabola, which is a valid approximation for Ψ_0^* close to the resonant surface r_s . The perturbation flux is assumed to be a sinusoidal variation with constant amplitude $\bar{\Psi}_1^*$, so that at $z = 0$ the 'constant Ψ approximation' is (similar to [26] and [13])

$$\Psi^* = \underbrace{\frac{1}{2} \frac{\partial^2 \Psi_0^*}{\partial r^2} \Big|_{r=r_s}}_{\Psi_0^*} (r - r_s)^2 + \underbrace{\bar{\Psi}_1^* \cos(m\theta)}_{\Psi_1^*} \quad . \quad (2.33)$$

This ansatz is taken to visualise the island structure in the poloidal plane and to derive characteristics of the magnetic island. It can be reformulated to

$$(r - r_s) = \pm \sqrt{\frac{2\bar{\Psi}_1^*}{\frac{\partial^2 \Psi_0^*}{\partial r^2} \Big|_{r=r_s}} \left(\frac{\Psi^*}{\bar{\Psi}_1^*} - \cos(m\theta) \right)} \quad . \quad (2.34)$$

Magnetic flux surfaces are given by constant Ψ^* which is shown for different Ψ^* in figure 2.2 for $m = 2$. The island separatrix is plotted in orange and fulfills $\Psi^* = \bar{\Psi}_1^*$. From this, the island width, W , can be calculated, resulting in

$$W = 4 \sqrt{\frac{\bar{\Psi}_1^*}{\frac{\partial^2 \Psi_0^*}{\partial r^2} \Big|_{r=r_s}}} \quad . \quad (2.35)$$

According to equation 2.30, the second derivative of the equilibrium flux Ψ_0^* can be formulated as

$$\frac{\partial^2 \Psi_0^*}{\partial r^2} \Big|_{r=r_s} = \frac{\partial B_{0,\theta}^*}{\partial r} \Big|_{r=r_s} = -\frac{B_{0,\theta}}{q_s} \frac{dq}{dr} \Big|_{r=r_s} \quad , \quad (2.36)$$

so that the island width can be written (using equation 2.31) as

$$W = 4 \sqrt{\frac{r_s B_r q_s}{m B_{0,\theta} \frac{dq}{dr} \Big|_{r=r_s}}} \quad . \quad (2.37)$$

The island width increases with the perturbation field component B_r and decreases with magnetic shear $s = \frac{r}{q} \frac{dq}{dr}$.

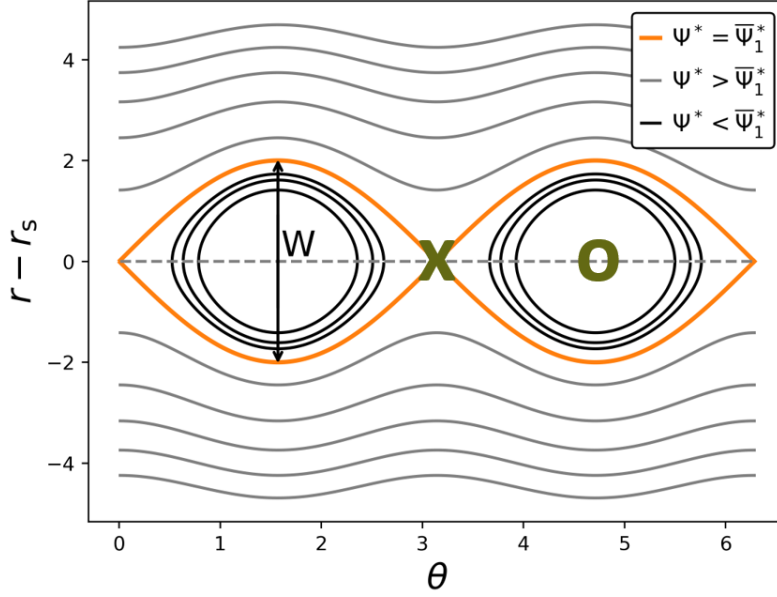


Figure 2.2: Magnetic flux surfaces calculated according to equation 2.34 with $\bar{\Psi}_1^* = 1$, $\left. \frac{\partial^2 \Psi_0^*}{\partial r^2} \right|_{r=r_s} = 1$ and $\Psi^* = a \bar{\Psi}_1^*$ with $a \in \{0, 0.2, 0.5, 1, 2, 4, 6, 8, 10\}$ for $m = 2$. The island separatrix is shown in orange and an X- and O-point are marked in olive green.

To study the temporal evolution of W , the temporal evolution of Ψ_1^* is derived. For this, the radial component of Faraday's law (cf. equation 2.5) is used to relate Ψ_1^* to an electric field in z -direction and to j_z via Ohm's law (cf. equation 2.3 neglecting $\mathbf{v} \times \mathbf{B}$ in the resistive layer).

$$\frac{im}{r} \frac{\partial \Psi_1^*}{\partial t} = \frac{\partial B_r^*}{\partial t} = -\frac{1}{r} \frac{\partial E_{1,z}}{\partial \theta} = -\frac{1}{r \sigma} \frac{\partial j_{1,z}}{\partial \theta} \stackrel{(2.28)}{=} -\frac{1}{r \sigma} im j_{1,z} \quad (2.38)$$

The perturbation current $j_{1,z} \cdot \delta$, where δ is the infinitesimally small thickness of the layer where $j_{1,z}$ flows, can be related to the jump of the tangential (poloidal) component, $B_{1,\theta}^*$, at the resonant surface:

$$\mu_0 j_{1,z} \delta = B_{1,\theta}^* \Big|_{r_s+\delta/2} - B_{1,\theta}^* \Big|_{r_s-\delta/2} = \frac{\partial \Psi_1^*}{\partial r} \Big|_{r_s-\delta/2} - \frac{\partial \Psi_1^*}{\partial r} \Big|_{r_s+\delta/2} . \quad (2.39)$$

The combination of equations 2.38 and 2.39 gives

$$\frac{\partial \Psi_1^*}{\partial t} = \frac{1}{\sigma \mu_0 \delta} \left(\frac{\partial \Psi_1^*}{\partial r} \Big|_{r_s+\delta/2} - \frac{\partial \Psi_1^*}{\partial r} \Big|_{r_s-\delta/2} \right) = \frac{1}{\sigma \mu_0 \delta} \Delta'_0 \Psi_1^* , \quad (2.40)$$

where the linear stability parameter

$$\Delta'_0 = \frac{\left(\frac{\partial \Psi_1^*}{\partial r} \Big|_{r_s+\delta/2} - \frac{\partial \Psi_1^*}{\partial r} \Big|_{r_s-\delta/2} \right)}{\Psi_1^*} \quad (2.41)$$

is introduced. $\Delta'_0 > 0$ represents an unstable situation, while $\Delta'_0 < 0$ means that Ψ_1^* decreases with time. To describe a non-linear island growth, the infinitesimally small

thickness δ is replaced by the island width W , so that the stability index $\Delta'(W)$ is a non-linear quantity. Equation 2.40 can be reformulated to obtain the Rutherford equation [27] using the resistive timescale τ_R (cf. equation 2.13 with $L = r_s$), relating Ψ_1^* to W (cf. equation 2.35) and taking the correct factor from numerical flux surface averaged calculations [13]:

$$\frac{\tau_R}{r_s} \frac{dW}{dt} = 1.22 r_s \Delta'(W) \quad . \quad (2.42)$$

In reality, there is a saturated island width, W_{sat} , at which $\frac{dW}{dt} = 0$, so that a simple ansatz for $\Delta'(W)$ can be chosen:

$$\Delta'(W) = \Delta'_0 \left(1 - \frac{W}{W_{\text{sat}}} \right) \quad , \quad (2.43)$$

which gives a solution for W :

$$W = W_{\text{sat}} \left(1 - e^{-\frac{t}{\tau_R} \frac{r_s^2 \Delta'_0}{W_{\text{sat}}^2}} \right) \quad . \quad (2.44)$$

In general, the current density that describes the growth of an island ($\frac{dW}{dt} \neq 0$) via Faraday's law (equation 2.5) is called the Rutherford current, while the current describing a saturated (non-growing) island via Ampère's law (equation 2.7) is used in the following to represent a tearing mode.

In a periodic screw pinch, all perturbation quantities have the exact same helicity in linear ideal MHD. If the displacement, $\boldsymbol{\xi}$, is aligned with the equilibrium magnetic field, \mathbf{B}_0 , on the q_s surface, then the perturbation magnetic field, $\mathbf{B}_1 = \nabla \times (\boldsymbol{\xi} \times \mathbf{B}_0)$ (cf. equation 2.19), and the perturbation current density, $\mathbf{j}_1 = \frac{1}{\mu_0} \nabla \times \mathbf{B}_1$ (cf. equation 2.7), also follow the field lines. Thus, a tearing mode in a screw pinch can be described by a perturbation current density

$$\mathbf{j}_1 \sim \mathbf{B}_0 e^{i(m\theta - n\frac{z}{R_0})} \quad , \quad (2.45)$$

which is parallel to the magnetic field lines on the resonant $q = m/n$ surface.

Difference between plasma and vacuum solution

In the model that will be introduced in section 4, the plasma around the resonant surface is treated as a vacuum. While an exact description of Ψ_1^* (in a screw pinch) requires solving the tearing mode equation (cf. equation 2.32), the vacuum assumption reduces to

$$\Delta \Psi_{1,\text{vac}}^* = 0 \quad , \quad (2.46)$$

with the solution

$$\Psi_{1,\text{vac}}^* = \begin{cases} \bar{\Psi}_1^* \left(\frac{r}{r_s}\right)^m e^{im\theta} & \text{if } r \leq r_s \\ \bar{\Psi}_1^* \left(\frac{r_s}{r}\right)^m e^{im\theta} & \text{if } r_s \geq r \end{cases} \quad , \quad (2.47)$$

where $\bar{\Psi}_1^*$ is the amplitude of the perturbation [13].

The solution of the tearing mode equation (equation 2.32) is obtained using a code based on [27, 28] where the conducting wall is placed at $r_w \rightarrow \infty$, for the equilibrium current density profiles (shown in figure 2.3)

$$j_{0,z}(r) = \left(1 - \left(\frac{r}{a}\right)^\nu \right)^\mu \quad , \quad (2.48)$$

where $(\nu, \mu) \in \{(1, 3), (2, 3), (2, 4)\}$ and a is the minor radius at the separatrix, and compared with $\Psi_{1,\text{vac}}^*$ (cf. equation 2.47).

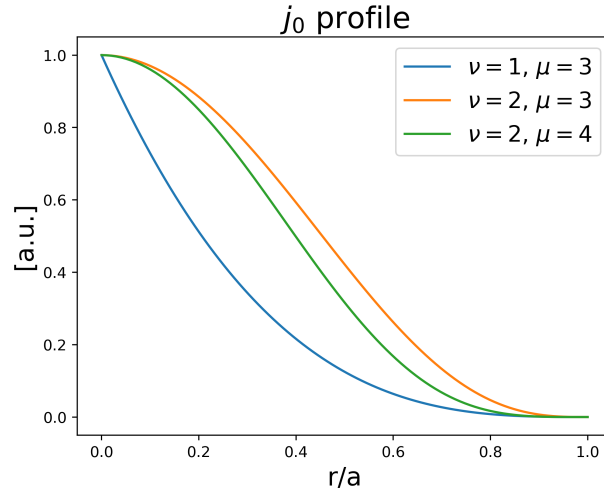


Figure 2.3: Equilibrium current density profiles according to equation 2.48 for $(\nu, \mu) \in \{(1, 3), (2, 3), (2, 4)\}$.

The top panel in figure 2.4 shows the solution of the tearing mode equation for $\nu = 2$, $\mu = 3$ together with the vacuum solution (equation 2.47) for an $m = 2$ mode. Solid lines represent the solutions with the same perturbed helical flux amplitude at the resonant surface. We then compare the perturbed helical fluxes at $r = a$, since in the experiment the measurements of the perturbation magnetic field at $r > a$ give an indication of the perturbation amplitude of the tearing mode at the resonant surface, and the radial dependence is the same for $\Psi_{1,\text{vac}}^*$ and Ψ_1^* outside the plasma. In the case of figure 2.4 the corresponding perturbed helical fluxes at $r = a$ differ by a factor $k_{m=2} = 0.6 < 1$, corresponding to an underestimation of $\Psi_{1,\text{vac}}^*$ (red dashed line) at the resonant surface due to the different radial decay of $\Psi_{1,\text{vac}}^*$ compared to Ψ_1^* from equation 2.32.

The corresponding perturbation current density profile, $j_{1,z}$, is calculated via the z component of Ampère's law (equation 2.7) in cylindrical coordinates,

$$\mu_0 j_{1,z} = \frac{1}{r} \left(\frac{\partial}{\partial r} (r B_{\theta,1}^*) - \frac{\partial B_r^*}{\partial \theta} \right) \quad , \quad (2.49)$$

and using equations 2.30 and 2.31

$$j_{1,z} = \frac{1}{\mu_0 r} \left(-\frac{\partial \Psi_1^*}{\partial r} - r \frac{\partial^2 \Psi_1^*}{\partial r^2} + \frac{m^2}{r} \Psi_1^* \right) \quad . \quad (2.50)$$

$j_{1,z}$ for the solutions Ψ_1^* , $\Psi_{1,\text{vac}}^*$ and $k_{m=2}\Psi_{1,\text{vac}}^*$ is shown in the lower panel of figure 2.4. The perturbation current density distribution corresponding to the solution of the tearing mode equation passes through zero at the resonant surface, in contrast to $j_{1,z}$ of the vacuum solution, which essentially describes an 'effective' current density. In both cases $j_{1,z}$ is quite localised on the resonant surface. Note that, for numerical reasons, the radial resolution of Ψ_1^* calculated according to [27, 28] is reduced inside the resonant surface for $r \rightarrow r_s$, leading to non-exact values of the perturbation current density near the resonant surface in figure 2.4, but the general shape can be shown.

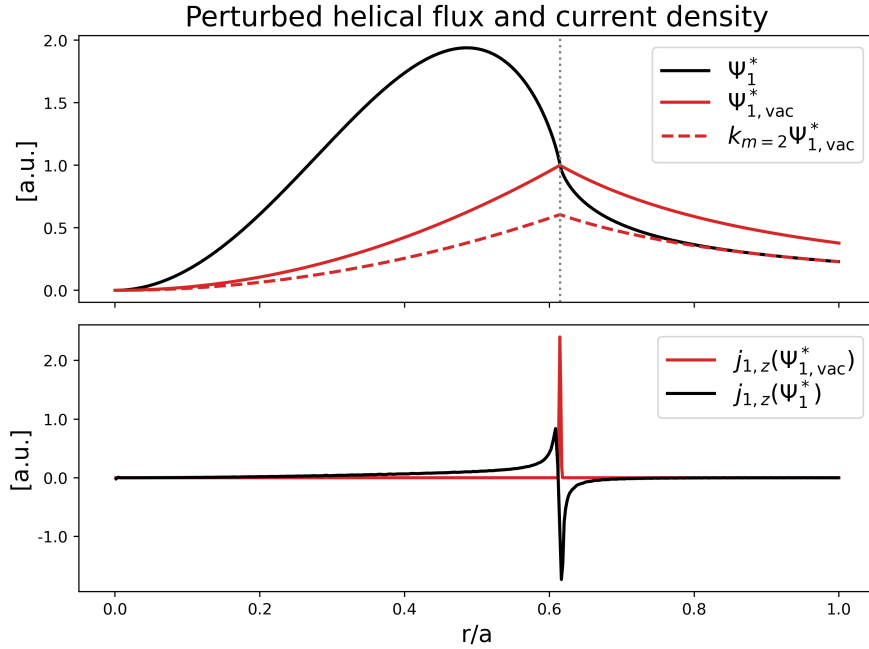


Figure 2.4: Solution of the tearing mode equation 2.32 (black) for an equilibrium current density profile according to 2.48 with $\nu = 2$, $\mu = 3$ and the corresponding q profile with $q_a = 4.5$ at $r = a$ together with the vacuum solution (red, equation 2.46) for the $m = 2$ mode (upper figure). The vacuum solution where $\Psi_1^* = \Psi_{1,\text{vac}}^*$ at $r = a$ is shown with a dashed red line. The corresponding perturbation current densities are shown in the lower figure.

To evaluate the influence of using $\Psi_{1,\text{vac}}^*$ instead of Ψ_1^* from the tearing mode equation on the determination of the mode composition, we compare the ratios of the perturbed helical fluxes at the plasma edge for an $m = 2$ and an $m = 3$ mode (denoted by the subscript) which are located at their q surfaces. If there were no influence on the determination of the relative mode composition, the same perturbation flux at the resonant surface would result in

$$\frac{\Psi_{1,m=2}^*}{\Psi_{1,m=3}^*} = \frac{k_{m=2}}{\underbrace{k_{m=3}}_k} \frac{\Psi_{1,\text{vac},m=2}^*}{\Psi_{1,\text{vac},m=3}^*} \quad (2.51)$$

with $k = 1$. However, $k < 1$ for current density profiles with $(\nu, \mu) \in \{(1, 3), (2, 3), (2, 4)\}$ as shown in table 2.1, so $m = 2$ modes are underestimated by the vacuum assumption, with a smaller effect for a steeper current profile. This must be taken into account when interpreting the results of the mode composition determination.

ν	μ	$r_{s,m=2}$	$r_{s,m=3}$	$k_{m=2}$	$k_{m=3}$	k
1	3	0.648	0.814	0.823	0.961	0.856
2	3	0.615	0.811	0.606	0.903	0.671
2	4	0.643	0.815	0.757	0.961	0.788

Table 2.1: Relation between Ψ_1^* and $\Psi_{1,\text{vac}}^*$ at $r = a$ for the same perturbed helical flux amplitude at $r = r_s$ for different equilibrium current density profiles, corresponding to different ν , μ , with $q_a = 4.5$ and different resonant surface positions $r_{s,m=2}$ and $r_{s,m=3}$.

For an interpretation of different perturbed helical flux amplitudes at the resonant surface, the relation of Ψ_1^* and $\Psi_{1,\text{vac}}^*$ to the island width needs to be discussed. An analytical expression for the island width (cf. equation 2.37) has been derived for the 'constant Ψ approximation'. A more accurate formulation of the island width would require solving $\Psi^* = \Psi_0^* + \Psi_1^*$ for the island separatrix with a realistic equilibrium helical flux Ψ_0^* and Ψ_1^* determined from equation 2.32.

We take the parabolic approximation for Ψ_0^* from equation 2.33 and compare the magnetic flux surfaces for the 'constant Ψ approximation' (cf. figure 2.2), the vacuum solution (cf. equation 2.47) and the solution of the tearing mode equation for $\nu = 2$, $\mu = 3$ in figure 1 for an $m = 2$ mode. In each subfigure of figure 2.5 the island separatrix is marked in red and the island width is given in the title. The island width calculated using the vacuum solution for the perturbed helical flux (figure b)) is the smallest with 89% of the island width from the 'constant Psi approximation' (cf. equation 2.35). If the curvature of the perturbed helical flux Ψ_1 in the radial direction is greater than the curvature of the equilibrium helical flux Ψ_0 , an additional island can form at the location of the usual X-point [29], which can be the case for the vacuum solution and is visible in figure b). For this equilibrium current density profile, the solution of the tearing mode equation (figure c)) gives an island width similar to W from equation 2.35 (97% of W from the 'constant Psi approximation'), although the asymmetric shape of the island differs from figure a).

Table 2.2 shows a comparison of the island widths using the solution of the tearing mode equation for different equilibrium current density profiles for $m = 2$ and $m = 3$. It shows that a more accurate description of W might results in a value smaller than W calculated according to the equation 2.35, i.e. the island width might be overestimated when calculated according to the equation 2.35. This effect seems to be quite small for the $m = 2$ mode, especially for current density profiles $(\nu, \mu) \in \{(2, 3), (2, 4)\}$, and amounts to an overestimation of about 10% for the $m = 3$ mode when calculating W according to the equation 2.35.

m	ν	μ	W	compared to W from 'const. Psi approx.'
2	1	3	0.296	94 %
2	2	3	0.307	97 %
2	2	4	0.308	97 %
3	1	3	0.283	90 %
3	2	3	0.288	91 %
3	2	4	0.287	91 %

Table 2.2: Island width of the solution of the tearing mode equation for different equilibrium current density profiles, corresponding to different ν, μ , with $q_a = 4.5$ for the $m = 2$ and $m = 3$ mode. The percentage of the island width compared to W from the 'constant Psi approximation' is given in the last column.

In summary, the vacuum assumption introduces uncertainties in the determination of the mode composition. For the equilibrium current densities considered here, the amplitude of the perturbed helical flux at the resonant surfaces is more underestimated for the $m = 2$ mode compared to the $m = 3$ mode. In addition, the calculation of the island width according to equation 2.35 slightly overestimates the width of the tearing mode equation solution, especially for the $m = 3$ mode and the equilibrium current density profiles regarded here, while for the $m = 2$ mode, the calculation of W according to equation 2.35 is close to the width of the tearing mode equation

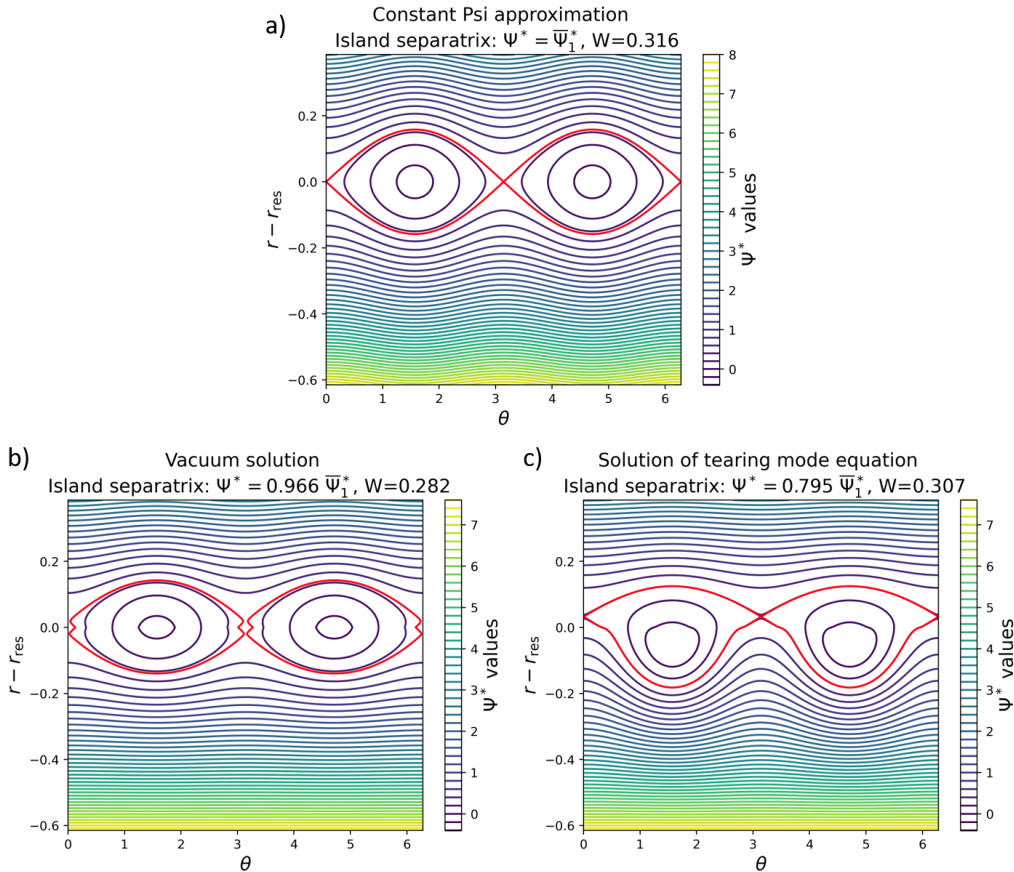


Figure 2.5: Ψ^* with a parabolic equilibrium flux $\Psi_0^* = 20 \cdot (r - r_s)^2$ and different Ψ_1^* for an $m = 2$ mode: Figure a) shows the contour plot of Ψ^* for the 'constant Psi approximation' with $\Psi_1^* = 0.25 \cdot \cos(m\theta)$ (similar to figure 2.2), figure b) the contour plot for the vacuum solution $\Psi_1^* = \text{Re}(\Psi_{1,\text{vac}}^*)$ with $\bar{\Psi}_1^* = 0.25$ (cf. equation 2.47), and figure c) the solution of the tearing mode equation for an equilibrium current density profile with $\nu = 2$, $\mu = 3$ and the corresponding q profile with $q_a = 4.5$. The solution of the tearing mode equation is multiplied by $\bar{\Psi}_1^* = 0.25$, so that Ψ_1^* at the resonant surface is the same for all cases. The island separatrix is marked in red, with the jagged structure at the X-point in figure b) indicating the formation of an additional island as described in [29]. The separatrix location and the island width is given in the title.

solution.

2.4.2 Tearing modes in a torus

When the periodic screw pinch is bent into a torus, the toroidal magnetic field, B_ϕ , corresponding to B_z in the screw pinch, varies as $\frac{1}{R}$ and is therefore no longer constant on a magnetic flux surface. Thus, the field line pitch changes with θ in a torus, which becomes even more pronounced for typical shaped cross sections with finite β . In order to obtain straight magnetic field lines in a plane spanned by a poloidal and a toroidal coordinate in a tokamak as well, a coordinate transformation from the torus coordinates (r, θ, ϕ) to straight field line coordinates (ρ, θ^*, ϕ) is made, where $\rho = \rho_{\text{pol}}$ (cf. equation 1.5) can be chosen [12].⁴ The straight field line angle

⁴An analytical expression for θ^* is derived in [30].

$\theta^*(\theta, r)$ is defined such that

$$\frac{\mathbf{B} \cdot \nabla \theta^*}{\mathbf{B} \cdot \nabla \phi} = \text{const} \quad . \quad (2.52)$$

Using equations 4.8.8 and 4.8.9 in [31], this expression can be related to the safety factor in straight field line coordinates, where q can be written as

$$q = \frac{\mathbf{B} \cdot \nabla \phi}{\mathbf{B} \cdot \nabla \theta^*} \quad . \quad (2.53)$$

For a plasma with nearly circular magnetic flux surfaces, θ^* can be calculated according to the Merezhkin formula [32]

$$\theta^*(\theta, r) = \theta - \lambda \sin \theta \quad (2.54)$$

with

$$\lambda = \frac{r}{R_0} \left(\beta_p(r) + \frac{l_i(r)}{2} + 1 \right) \quad , \quad (2.55)$$

where $\beta_p = \frac{\langle p \rangle}{\langle B_\theta^2 \rangle / 2\mu_0}$ is the poloidal plasma β , and l_i the internal inductance [13]. Figure 2.6 shows several magnetic flux surfaces of a nearly circular plasma on the left, together with lines of constant angles θ and $\theta^*(\theta, r)$ from the equilibrium reconstruction.⁵ A comparison between the equilibrium reconstruction of $\theta^*(\theta, r)$ and the value calculated according to the Merezhkin formula is shown in the right plot of figure 2.6. In this case, the Merezhkin formula with $\lambda = 0.4$ is in agreement with the reconstructed values for the $q = 2$ surface.

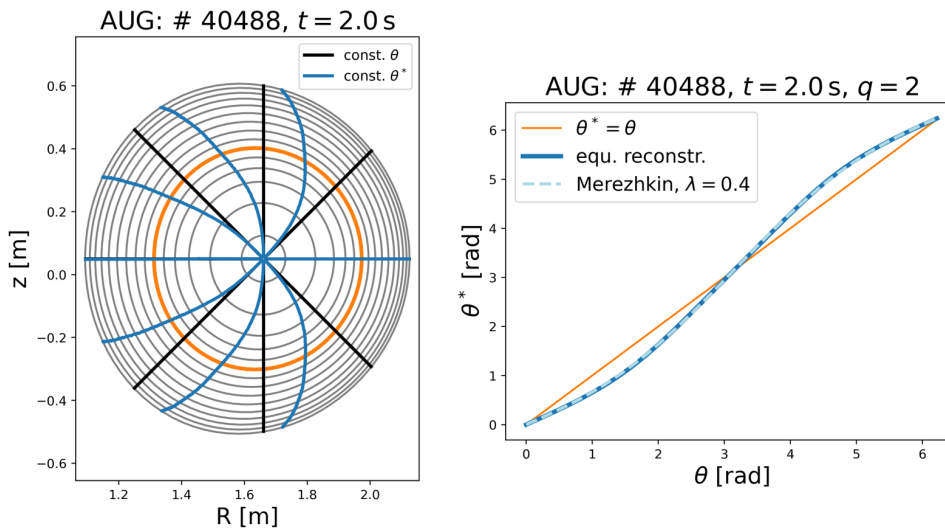


Figure 2.6: Equilibrium reconstruction for discharge 40488 at $t = 2.0$ s. On the left, several magnetic flux surfaces are shown in grey, while the $q = 2$ surface is shown in orange. Black and blue lines indicate lines of constant θ and θ^* , respectively. The right plot shows the equilibrium reconstruction of θ^* on the $q = 2$ surface and θ^* calculated using the Merezhkin formula.

⁵The equilibrium is reconstructed based on the CLISTE code [33], which solves the Grad-Shafranov equation. In the example of discharge 40488 (cf. figure 2.6), the IDE code [34] has been used, which additionally takes the flux diffusion into account.

An instability in a torus, that is aligned with \mathbf{B}_0 is therefore described with a poloidal phase $m\theta^*$. Note that in a toroidal device with finite β , different perturbation quantities do not necessarily have the same helicity: If the displacement, $\boldsymbol{\xi}$, has the helicity of \mathbf{B}_0 , the parallel perturbation current density, \mathbf{j}_1 , is not described by a single pair of (m, n) , contrary to section 2.4.1. To show this, we assume a pure radial displacement

$$\boldsymbol{\xi} = \xi_0(r) e^{i(-n\phi + m\theta^*(\theta, r))} \hat{r} \quad , \quad (2.56)$$

and an equilibrium magnetic field in the approximation of non-shifted circular flux surfaces, according to equations 2.57 and 2.73 in [13],

$$\mathbf{B}_0 = \frac{B_{\phi,0}}{1 + \frac{r}{R_0} \cos \theta} \hat{\phi} + \underbrace{\frac{\mu_0 I_p(r)}{2\pi r}}_{c_1(r)} \left(1 + \frac{r}{R_0} \underbrace{\left(\beta_p(r) + \frac{l_i(r)}{2} - 1 \right)}_{\tilde{c}_2} \cos \theta \right) \hat{\theta} \quad (2.57)$$

where $B_{\phi,0}$ is the toroidal magnetic field at the magnetic axis at R_0 . The perturbed vector potential $\mathbf{A}_1 = \boldsymbol{\xi} \times \mathbf{B}_0$ (cf. equation 2.19) results in

$$\begin{aligned} \mathbf{A}_1 = & \xi_0(r) e^{-in\phi} \cdot \\ & \left(-c_1(r) \left(e^{im\theta^*} + \frac{\varepsilon \tilde{c}_2}{2} \left(e^{i(m+1)\theta^*} e^{i\varepsilon c_3 \sin \theta^*} + e^{i(m-1)\theta^*} e^{-i\varepsilon c_3 \sin \theta^*} \right) \right) \right) \hat{\phi} \\ & + B_{\phi,0} \left(e^{im\theta^*} - \frac{\varepsilon}{2} \left(e^{i(m+1)\theta^*} e^{i\varepsilon c_3 \sin \theta^*} + e^{i(m-1)\theta^*} e^{-i\varepsilon c_3 \sin \theta^*} \right) \right) \hat{\theta} \end{aligned} \quad (2.58)$$

where the inverse aspect ratio $\varepsilon = \frac{r}{R_0}$ is introduced and c_3 is defined as $c_3 = \left(\beta_p(r) + \frac{l_i(r)}{2} + 1 \right)$.⁶ Additionally, $\cos \theta = \frac{e^{i\theta} + e^{-i\theta}}{2}$ and the approximation for small ε that $\frac{1}{1 + \varepsilon \cos \theta} \approx (1 - \varepsilon \cos \theta)$ and $\theta \approx \theta^* + \varepsilon c_3 \sin \theta^*$ have been used. Equation 2.58 already shows that \mathbf{A}_1 has poloidal sidebands with $(m \pm 1)$ in θ^* of the order of ε . To calculate the perturbed magnetic field $\mathbf{B}_1 = \nabla \times \mathbf{A}_1$, the curl of \mathbf{A}_1 in torus coordinates can lead to even more complicated poloidal sidebands, especially if the perturbation current density is calculated from $\mathbf{j}_1 = \mu_0 (\nabla \times \mathbf{B}_1)$. Thus, the perturbation quantities $\boldsymbol{\xi}$, \mathbf{A}_1 , \mathbf{B}_1 and \mathbf{j}_1 do not usually have the same helicity. In general, the form of $\xi_0(r)$ (cf. equation 2.56), and thus also the corresponding \mathbf{j}_1 , is non-trivial and requires the use of a numerical model that solves the MHD equations for stability, as described, for example, in [35].

Figure 2.7 shows the poloidal harmonics, i.e. harmonics with the same toroidal mode number, of the normalised perturbation current density amplitude parallel to the magnetic field, $\hat{j}_{1,\parallel}$, calculated using the linear MHD stability code CASTOR3D [36] for a (2,1) tearing mode for negligibly small and finite β . At finite β poloidal sidebands, which are non-resonant poloidal harmonics, especially those with $\Delta m = 1$, might become significant.

However, as a first order approximation, the perturbation current density, \mathbf{j}_1 , is defined in the following to flow force-free, i.e. aligned with \mathbf{B}_0 . The corrections to this ansatz are discussed in section 4.5.

As a magnetic island introduces magnetic field lines that have a radial component (cf. figure 2.2), heat and particle transport, which is much higher parallel than perpendicular to field lines, is amplified in radial direction, leading to a flattening of the profiles at the location of a magnetic island [13]. Thus, the existence of an island can

⁶Since \tilde{c}_2 and c_3 depend on r only through $\beta_p(r)$ and $l_i(r)$, the r dependence is not written explicitly.

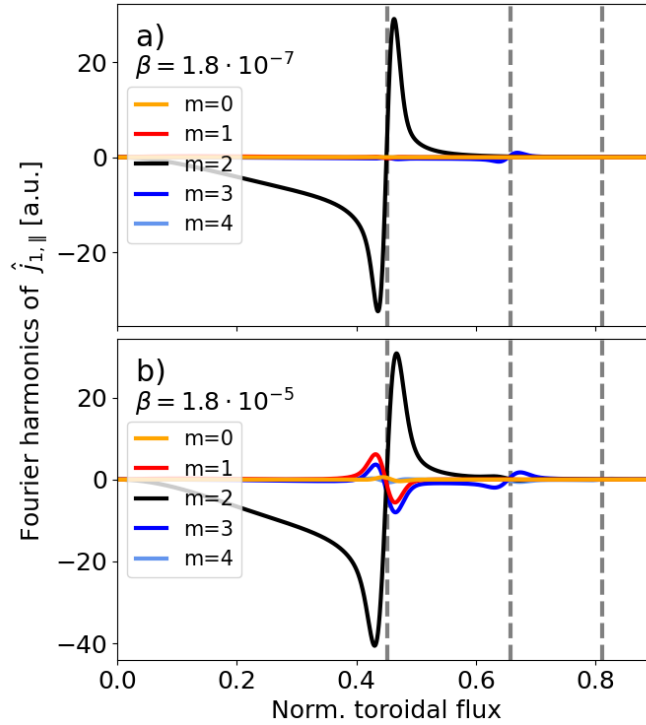


Figure 2.7: $\hat{j}_{1,\parallel}$ for a (2,1) tearing mode for negligibly small (figure a)) and finite β (figure b)). The grey dashed lines indicate the position of the $q = 2$, $q = 3$ and $q = 4$ surfaces at a normalised toroidal flux of 0.45, 0.66 and 0.81, respectively. For negligibly small β , the tearing mode is well-described by the $m = 2$ Fourier component at the $q = 2$ surface. For finite β , there are significant contributions of the $m = 1$ and $m = 3$ harmonics at the $q = 2$ surface. There is also a small $m = 3$ contribution on the $q = 3$ surface, corresponding to a $(m = 3, n = 1)$ tearing mode. (Figure: courtesy of Jonas Puchmayr, MPI for Plasma Physics)

result in a flattening of the pressure gradient within the island. In tokamaks, there is a current density resulting from the collisions of trapped⁷ and passing particles, called the bootstrap current, which is $\mathbf{j}_{\text{bs}} \sim \nabla p$ [37]. A reduced ∇p therefore leads to a deficit of the bootstrap current density, which is similar to the perturbation current density discussed above, describing a tearing mode.⁸ In this case, the tearing mode is a pressure gradient driven NTM, as it is classically stable ($\Delta'(W) < 0$) and exists only because of the bootstrap current described in neoclassical theory, which includes the effects of toroidicity.

These NTMs often occur in plasma discharges with high β , where ∇p is large without an island. A so-called seed island causing a reduced ∇p excites the mode to an island width W larger than the seed island width W_{seed} . The saturated island width of an NTM is proportional to the poloidal β . There exists a marginal pressure $\beta_{\text{p,marg}}$ at which the NTM disappears when β_{p} is reduced, where $\beta_{\text{p,marg}} \ll \beta_{\text{p,onset}}$ and $\beta_{\text{p,onset}}$ is β_{p} at the onset of the NTM. [12]

As the example of NTMs shows, additional effects must be taken into account in

⁷Owing to the conservation of the magnetic moment $\mu = \frac{m v_{\perp}^2}{2B}$ and the kinetic energy, particles can be 'trapped', if the ratio between the initial parallel and perpendicular velocity $\frac{v_{\parallel}}{v_{\perp}} < \sqrt{\frac{B_{\text{max}}}{B_{\text{min}}} - 1}$. They change direction along their path towards the HFS at higher magnetic field.

⁸One method to compensate the missing \mathbf{j}_{bs} for the suppression of NTMs is to apply a localised current drive at the island location [38], which has to be inferred from the measurements.

a torus with finite β . Likewise, the Rutherford equation (cf. equation 2.41) must be extended to include additional stabilizing and destabilizing terms related to non-inductive currents such as the bootstrap current [39, 40], a current that guarantees $\nabla \cdot \mathbf{j} = 0$ [41, 40], and the polarisation current [42], as well as external influences [43, 44].⁹

In this work, no distinction is made between classical and neoclassical tearing modes. Although most experimental examples are NTMs, each mode is referred to as a tearing mode and is described by a perturbation current density

$$\mathbf{j}_1 \sim \mathbf{B}_0 e^{i(m\theta^* - n\phi + \omega t)} \quad . \quad (2.59)$$

This is similar to equation 2.45 where the rotation frequency ω is added to take into account the rotation of the tearing mode.

2.4.3 Rotation, braking and locking of tearing modes

Owing to the balance of torque and viscosity, tearing modes usually rotate with a velocity between the fluid velocity of the plasma, $\mathbf{v}_{\text{fluid}}$, and the sum of $\mathbf{v}_{\text{fluid}}$ and the diamagnetic drift velocity, $\mathbf{v}_{\text{dia}} \perp \mathbf{B}$, arising due to a pressure gradient. For large magnetic islands, where the pressure gradient becomes very small, the island rotation approaches $\mathbf{v}_{\text{fluid}}$. [13]

The fluid velocity of the plasma can have a poloidal and a toroidal component, but the poloidal rotation with ω_{pol} is strongly damped in the core plasma, such that the toroidal rotation with ω_{tor} - with different rotation frequencies depending on ρ_{pol} - dominates.¹⁰ Therefore, the angular frequency $\omega = n\omega_{\text{tor}} + m\omega_{\text{pol}}$ (cf. section 3.1.2 in [12]) of the modes rotating with the plasma frame is dominated by the toroidal mode number n .

The rotating perturbation field of the mode induces currents in the conducting vacuum vessel around the plasma, which shield the magnetic fields to the outside. The induced currents in the resistive wall, \mathbf{j}_{wall} , exert a braking force on a rotating mode, which is stronger for larger modes. A very slowly rotating mode can stop rotating, i.e. become locked¹¹, by interacting with the resonant component of an error field of the tokamak arising from imperfections. [13]

A model for mode braking and locking is derived in [46] taking the resistive wall and the viscous coupling to the plasma into account. A tearing mode can also be born locked, if the error field is so large, that it overcomes the shielding effect of the plasma. In AUG, the so-called compass scan [47] was performed to identify the error field. Discharges were performed with an applied perturbation field with different orientations, hence the name, which causes a born locked mode. The error field of AUG is very small (cf. [47, 48]) and born locked modes usually do not exist in NBI heated plasmas without externally applied field.

In general, a higher rotation frequency allows for higher error fields. For larger fusion devices with low rotation frequency of the plasma and therefore with low rotation frequency of the tearing mode, the predicted critical error field for getting locked modes is relatively small. [49]

⁹See for example [45] for a detailed discussion of the additional terms.

¹⁰In AUG, the toroidal plasma rotation mainly arises due to the injection of neutral particles (Neutral Beam Injection (NBI)) in toroidal direction to heat the plasma.

¹¹In this work, the term locked modes always refers to locking with respect to the laboratory frame, while phase-locked modes will be referred to as coupled (or phase-locked) modes.

2.4.4 Influence of a conducting wall on the perturbation magnetic field of a rotating mode

As described in the previous section, a rotating mode induces mirror currents in the conducting structures around the plasma, which in turn affect the perturbation magnetic field of the mode. Correctly accounting for these induced currents is important for the interpretation of measurements that detect the perturbed magnetic field of rotating modes (cf. section 3.3).

An analytical formula for the perturbed magnetic flux Ψ_1^* in cylindrical geometry with a circular wall at r_w concentric around a circular resonant surface at r_s containing a rotating mode at frequency ω is derived in [13]. Ψ_1^* is calculated in the vacuum region inside r_s (region I), between r_s and r_w (region II) and outside r_w (region III). The induced current density in the wall, j_w , is obtained from Ψ_1^* via the radial component of Faraday's law (cf. equation 2.5) and the jump of the tangential magnetic field component across the wall. This results in

$$j_w = \frac{r_w \sigma}{2m\tau_w} \cdot \left(\frac{\partial \Psi_{\text{III}}^*}{\partial r} \Big|_{r=r_w} - \frac{\partial \Psi_{\text{II}}^*}{\partial r} \Big|_{r=r_w} \right), \quad (2.60)$$

where σ is the wall conductivity, Ψ_{II}^* and Ψ_{III}^* are the perturbed magnetic fluxes in regions II and III (cf. equations equation 7.20 to 7.22 in [13]) with

$$\frac{\partial \Psi_{\text{III}}^*}{\partial r} \Big|_{r=r_w} = -\bar{\Psi}^* \frac{i}{i + \omega\tau_w} \left(\frac{r_s}{r_w} \right)^m \left(\frac{m}{r_w} \right) \cdot e^{i(m\theta - \omega t)}, \quad (2.61)$$

$$\frac{\partial \Psi_{\text{II}}^*}{\partial r} \Big|_{r=r_w} = \bar{\Psi}^* \left(\left(\frac{r_s}{r_w} \right)^m \left(-\frac{m}{r_w} \right) - \frac{\omega\tau_w}{i + \omega\tau_w} \left(\frac{r_s}{r_w} \right)^m \frac{m}{r_w} \right) \cdot e^{i(m\theta - \omega t)}, \quad (2.62)$$

where $\bar{\Psi}^*$ is the perturbation amplitude, and

$$\tau_w = \frac{\mu_0 \sigma d r_w}{2m} \quad (2.63)$$

is the resistive timescale of the wall of thickness d . In general, τ_w depends on the frequency itself, as the skin depth, where the induced current flows, changes with ω . At low $\omega\tau_w$, the frequency dependence of the induced currents, and hence their effects, changes the most which is one of the motivations for implementing the model described in section 4.

Owing to the induced currents, the perpendicular and tangential components of the magnetic field have a different frequency dependence in the vicinity of an electrical conductor. In the cylindrical approximation, the magnetic field components perpendicular and tangential to the conducting wall are calculated according to equation 7.21 in [13] and equations 2.30 and 2.31 giving

$$B_r = i \hat{B} \left(\left(\frac{r_s}{r} \right)^m - \frac{\omega \tau_w}{i + \omega \tau_w} \left(\frac{r_s}{r_w} \right)^{2m} \left(\frac{r}{r_s} \right)^m \right) \cdot e^{i(m\theta - \omega t)} \quad (2.64)$$

$$B_\theta = \hat{B} \left(\left(\frac{r_s}{r} \right)^m + \frac{\omega \tau_w}{i + \omega \tau_w} \left(\frac{r_s}{r_w} \right)^{2m} \left(\frac{r}{r_s} \right)^m \right) \cdot e^{i(m\theta - \omega t)}, \quad (2.65)$$

where $\hat{B} = \bar{\Psi}^* m / r$ is the perturbation field amplitude at r_s for $\omega = 0$. In this geometry, the perpendicular and tangential components correspond to the radial and poloidal components, B_r and B_θ , respectively. We keep this nomenclature also

for toroidal (and shaped) geometries, where these magnetic field components are only approximately perpendicular or tangential.

The frequency dependence of the amplitude of the poloidal and radial field components calculated according to equations 2.64 and 2.65 is shown in figure 2.8. As the frequency increases, the amplitude of B_r is attenuated while the amplitude of B_θ is enhanced by the mirror currents in the wall. For fast rotating modes, in the limit of $\omega\tau_w \rightarrow \infty$, B_θ approaches $2\hat{B}$ and B_r approaches zero directly at the wall.

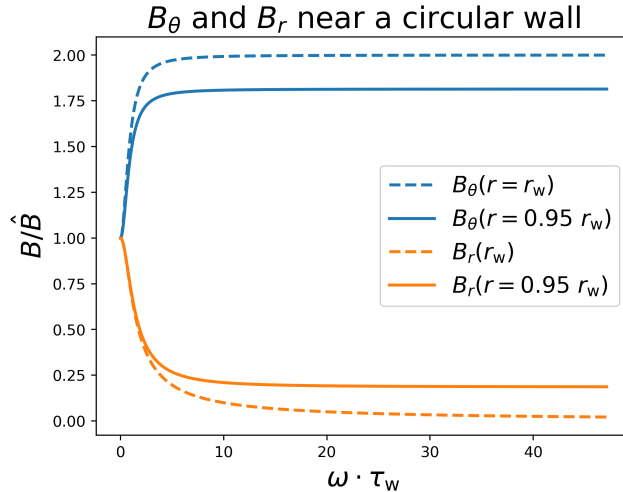


Figure 2.8: Frequency dependence of the radial and poloidal magnetic field amplitudes calculated according to equations 2.64 and 2.65. The magnetic perturbation field is generated by an $m = 2$ mode at $r_s = 0.8$ m with $j_{\text{pert}} \propto \delta(r - r_s)e^{i(-\omega t + m\theta)}$. Dashed lines show the radial and poloidal field components directly at the wall $r_w = 1.0$ m; solid lines show the radial and poloidal components 5 cm away from the wall, normalised by the magnetic field amplitude at $\omega = 0$. Here, the resistive timescale of the wall is $\tau_w = 10^{-3}$ s.

The frequency dependence of the amplitudes of B_r and B_θ changes to a slight extent in a toroidal configuration with a perturbation current according to equation 2.59. This will be shown and discussed in section 4.3.

2.4.5 Toroidal mode coupling

In a tokamak, poloidal symmetry is broken by the toroidal nature and shaping of the plasma, so that tearing modes at different resonant surfaces with the same toroidal mode number n , but different poloidal mode numbers m can couple together (cf. chapter 3 in [12]). If so, they rotate at the same rotation frequency, i.e. their phase relation is the same for all ϕ , but varies with θ . The difference in ω between uncoupled tearing modes with the same n is due to the radial variation of ω_{tor} . The coupling of these modes is facilitated when the differential rotation of their resonant surfaces is small. While it was originally thought, that tearing modes usually couple constructively at the LFS [50], it was shown that in AUG the poloidal position at which the tearing modes are in phase can vary from the LFS over the top to the HFS depending on plasma pressure and plasma rotation velocity [22].

The determination of amplitude and phase relations of coupled tearing modes is crucial to analyse tearing modes before a disruption. The formalism used in this

work to determine the poloidal mode composition in terms of amplitudes and phases is described in 4.5.

2.5 Role of tearing modes in regards to disruptions

As already indicated in the previous sections, tearing modes lead to an increased transport in the radial direction, as they form a short circuit for heat transport, which degrades the confinement of a tokamak plasma [19]. If coupled magnetic islands overlap, this leads to a stochastisation of the field lines in this region and, in turn, to even worse confinement degradation [20], especially at the poloidal angle where the modes are in phase. Thus, (coupled) tearing modes are often precursors to disruptions and are involved in the disruption process itself [18]. Especially locked modes cause a large decrease in β [51] and often result in a disruption. As locked modes inherently have the same frequency $\omega = 0$, mode coupling is supposed to play an important role. In order to understand in which cases tearing modes cause a disruption, the investigation of the poloidal mode composition, indicating the involved resonant surfaces, in terms of amplitudes and phases is of high importance.

2.6 Description of tearing modes in this work

Parts of the content and text of this section are included in a publication accepted by Plasma Physics and Controlled Fusion (DOI 10.1088/1361-6587/adc0bd), of which the author of this thesis is the first author.

In this work, tearing modes are described by helical perturbation current densities (cf. equation 2.59) in an annulus between two flux surfaces. We define base vectors

$$\mathbf{j}_{\text{pert}}^{(m,n)} \propto \mathbf{B}_0 e^{i(\omega t - n\phi + m\theta^*)} \quad (2.66)$$

with single helicities $((m, n))$, such that \mathbf{j}_{pert} can be expressed by

$$\mathbf{j}_{\text{pert}} = \sum_{m,n} \tilde{a}^{(m,n)} \mathbf{j}_{\text{pert}}^{(m,n)} \quad (2.67)$$

with complex amplitudes

$$\tilde{a}^{(m,n)} = a^{(m,n)} e^{i\varphi^{(m,n)}}. \quad (2.68)$$

The base vectors represent the harmonics of the mode, where those with the same toroidal mode number are called the poloidal harmonics. Describing a tearing mode can be translated to describing its complex amplitudes $\tilde{a}^{(m,n)}$. Note that in our base vector system, a pure (m, n) mode on its resonant $q = m/n$ surface might require the consideration of poloidal sidebands, which are non-resonant poloidal harmonics. This has already been indicated in section 2.4.2 and will be discussed further in section 4.5.

The radially localised ansatz of equation 2.66 describes an 'effective' current density, similar to the perturbation current density corresponding to $\Psi_{1,\text{vac}}^*$ described in section 2.4.1, where it was shown that the perturbation current density corresponding to the tearing mode equation solution is quite localised on the resonant surface. We assume a monotonically increasing q profile and hence no resonance with a second surface of the same helicity, justifying the ansatz used in this work. However, the consequences of treating the plasma as a vacuum, as discussed in section 2.4.1, must be considered when interpreting the quantitative values of the amplitudes $a^{(m,n)}$.

3 Measurements of tearing modes

Parts of the content, figures and text of this chapter are included in a publication accepted by Plasma Physics and Controlled Fusion (DOI 10.1088/1361-6587/adc0bd) of which the author of this thesis is the first author.

A first step to analyse tearing modes is their detection by suitable measurements which can measure a perturbation related to a tearing mode. This can be either a local measurement within the plasma (like Electron Cyclotron Emission spectroscopy (ECE)), a line-integrated measurement (like Soft X-Ray (SXR) measurement) or a measurement of a perturbation outside the plasma (like magnetic measurements). The ensuing determination of mode characteristics, as the mode frequency and mode numbers, requires a sufficient high sampling rate, appropriate positions of the measurements and a model for calculating synthetic measurements. Since the perturbation quantities are usually small compared to the equilibrium, mode characterisation is facilitated if the perturbation rotates in the laboratory frame. [12]

The following sections 3.1 and 3.2 introduce the ECE and SXR measurements that can be used for tearing mode detection. Magnetic measurements, which are the diagnostic primarily used in this work, are explained in more detail in section 3.3.

3.1 Electron cyclotron emission spectroscopy

The passive technique of ECE is used to measure the electron temperature T_e locally, i.e. not by a line integral, along a Line of Sight (LOS). Usually, the LOS are directed from the LFS outside the plasma towards the magnetic axis, primarily in major radial direction [12]. Owing to the gyration of the electrons around the magnetic field lines (cf. section 1.2), electromagnetic radiation is emitted at harmonics of the electron cyclotron frequency [6]

$$\omega_{ce} = \frac{eB}{m_e} \quad , \quad (3.1)$$

which depends on the magnetic field strength $B = \sqrt{B_\phi^2 + B_\theta^2}$. The radiation observed can be spectrally resolved and thus measured absolutely [8]. For optically thick plasmas, the emission intensity has a direct relation to T_e [6]. Because of the dependence of the magnetic field strength on the major radius with $B_\phi \sim 1/R$ (cf. section 1.2), ω_{ce} can be related to a radial position in the plasma, leading to a local T_e measurement. B_θ , which is about 10% of B_ϕ and thus only about 0.5% of B , is also taken into account.¹²

In the plasma core, where most of the harmful tearing modes are located, the emission is optically thick and the electron temperatures can be deduced together with their locations. Provided a radially decreasing background temperature profile, tearing modes with a substantial flattening of the T_e profile are visible in ECE with suitable settings. Figure 3.1 shows an example of a contour plot of different channels of ECE. In this case, the tearing modes are clearly visible at $\rho_{pol} = 0.4$ and $\rho_{pol} \approx 0.75$ – corresponding to the $q = 2$ and $q = 3$ surfaces – because of the lower temperatures

¹²In AUG, changes in the toroidal magnetic field and the magnetic field ripple due to the discrete toroidal field coils at the position of the LOSs of the ECE diagnostic are also considered.

inside the island separatrix. Here, the electron temperature profile is even hollow within the magnetic island of the $m = 2$ tearing mode at $\rho_{\text{pol}} = 0.4$. The flattening of T_e due to the tearing modes is also visible in the T_e profile. The tearing modes on the $q = 2$ and $q = 3$ surfaces have the same frequency with a phase shift of π , hence they are coupled (cf. section 2.4.5) in anti-phase on the LFS.

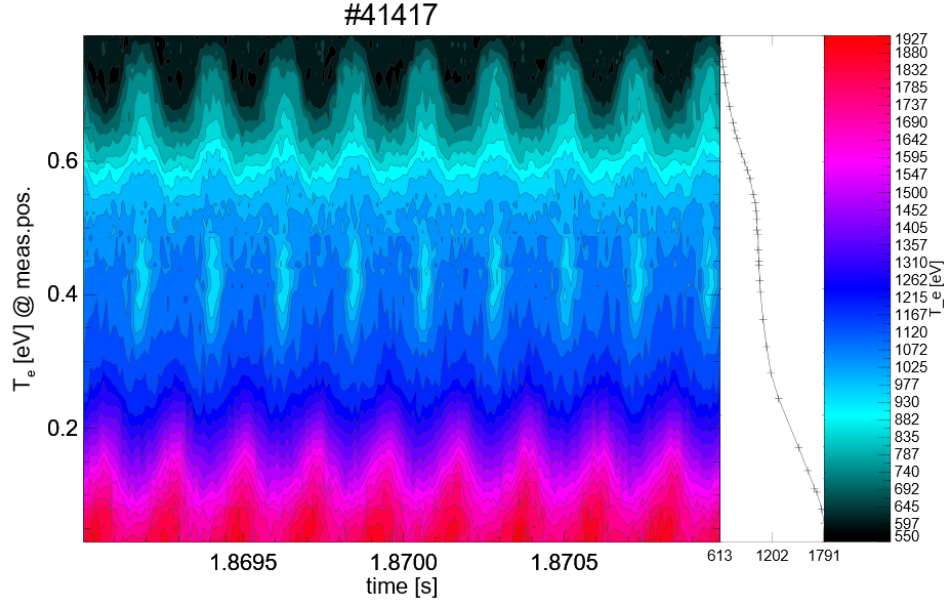


Figure 3.1: Contour plot of T_e (colour bar on the right) determined from ECE of discharge 41417 between $t = 1.8690$ s and 1.8710 s. The magnetic flux surface label ρ_{pol} is shown on the y-axis. A profile of T_e depending on ρ_{pol} is shown between the contour plot and the colour bar.

As the example of figure 3.1 shows, appropriate settings allow comparing the resonant surface position from equilibrium reconstruction with the island position determined from ECE. Furthermore, coupled tearing modes at different q surfaces and their phase relation can be analysed using ECE, as for example done in [22].

3.2 Soft x-ray measurement

The SXR diagnostic consists of semiconductor diodes and is a line-integrated measurement. The quantity observed is the radiation power density along many LOS covering a poloidal cross section of the plasma in AUG as shown in figure 3.2, where the LOS of the SXR diagnostic are shown together with the location of the ECE. By introducing material filters (usually beryllium foil filters), photons with low energy can be blocked, allowing the radiation and fluctuations of the hot central plasma to be studied. To obtain spatial information on local emissivity, an inversion algorithm, i.e. a tomographic reconstruction, is required. By analysing the oscillations of different LOS angles via Fast Fourier Transform (FFT), it is possible to deduce the poloidal mode number of an instability in the core plasma. A mode profile of SXR measurements is obtained by ordering, e.g. by the angle of the LOS with regard to the direction $\theta = 0$, the amplitudes and phases at the frequency with the maximum amplitude determined from the FFT of a time signal where the oscillation is clearly visible. For an uncoupled mode, the mode profile shows m amplitude minima and m phase jumps by π . This is explained by the fact that the diagnostic detects a signal where the perturbation consists essentially of the contributions of the intersection of

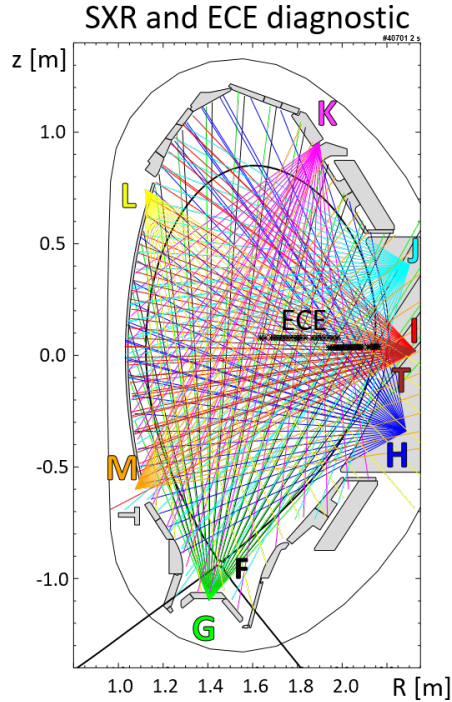


Figure 3.2: The LOS of the various channels of the SXR diagnostic, indicated by letters, are displayed as lines of different colours, together with the position of the ECE (black crosses) for discharge 40701 at 2.0s. The separatrix is shown in black.

the LOS with the resonant surface and by geometrical considerations in cylindrical geometry [12]. An example of an $m = 1$ mode is shown in figure 3.3, where one amplitude minimum and one phase jump of about π are visible at about a LOS angle of 3.1 rad. Owing to the higher temperatures in the core plasma, the radiation is higher in the central part of the plasma (cf. figure 3.3 a)). Thus the $m = 1$ mode is visible in the SXR data, even though the dominant poloidal mode number obtained from the magnetic measurements is $m = 2$.

We use the SXR diagnostic in particular to check whether an $m = 1$ mode is present in the core of the plasma at the $q = 1$ surface (cf. figure 3.3). In principle, other small poloidal mode numbers can be observed with the SXR diagnostic [12]. Care should be taken in the interpretation of SXR signals when modes are coupled.

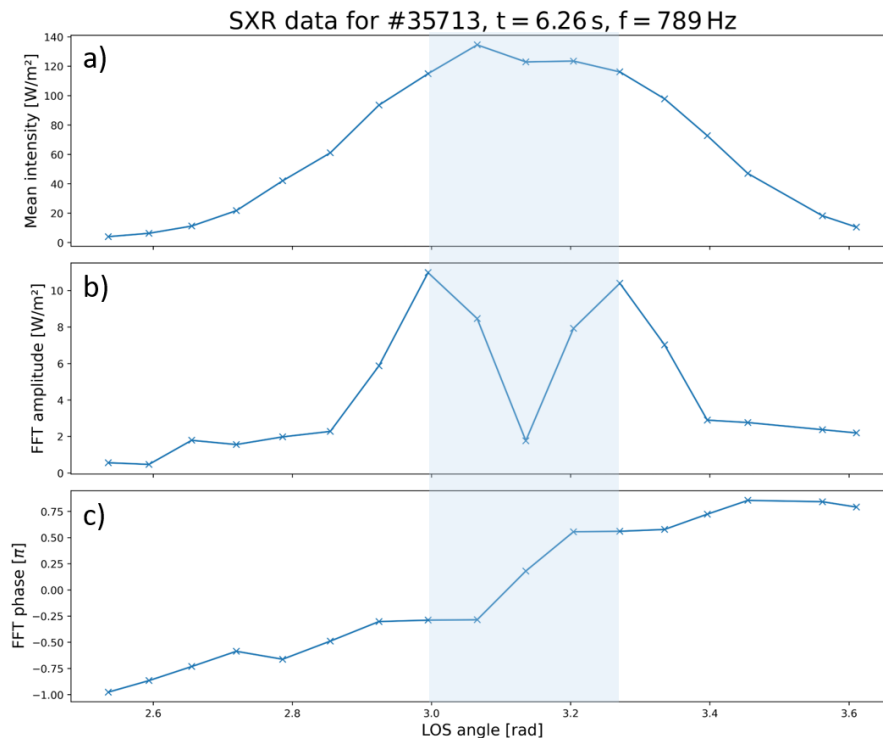


Figure 3.3: Signals of channel I of the SXR diagnostic as a function of the LOS angle: figure a) shows the mean intensity, figures b) and c) the amplitudes and phases at $f = 789$ Hz, determined from the FFT of a central LOS signal. The central part, where the amplitude minimum (figure b)) and the phase jump of about π (figure c)) occur, is marked in light blue.

3.3 Magnetic measurements

As ECE measurements are not always available for the resonant surfaces of interest and SXR measurements are line integrated, magnetic measurements are suitable for tearing mode detection as they measure locally outside the plasma and are always available without special settings. The passive coils measuring the perturbation magnetic field generated by a tearing mode are installed at AUG with different orientations at different positions. For constructional reasons, they are often mounted on or near conducting structures and are therefore influenced by mirror currents induced by rotating modes (cf. section 2.4.4). Note that from magnetic measurements alone it is in principle not clear whether the perturbation magnetic field is generated by an ideal instability, e.g. a kink mode, or by a resistive tearing mode. However, due to the growth rates and effects of the mode, we usually assume that the instability is a tearing mode and therefore use this term in most of the following.

3.3.1 Passive coils for mode detection

A time-varying magnetic field, e.g. the perturbation field of a tearing mode, is detected via the induced voltage

$$U_{\text{ind}} = -N_{\text{coil}} \frac{d\Psi_{\text{B}}}{dt} \quad (3.2)$$

with N_{coil} the winding number and $\Psi_{\text{B}} = \int_S \mathbf{B} \cdot d\mathbf{S}$ the magnetic flux through one coil winding with area S and normal vector $d\mathbf{S}$.

Usually, the measured coil voltages of coils k are converted into the temporal derivative of the perturbation magnetic field, $\dot{\tilde{B}}_{\text{meas},k}$, averaged over the coil volume. The complex amplitude

$$\tilde{B}_{\text{meas},k} = a_{\text{meas},k} e^{i\varphi_{\text{meas},k}} \quad (3.3)$$

is then derived by temporal Fourier transform of $\dot{\tilde{B}}_{\text{meas},k}$ and division by the rotation frequency ω . This gives $a_{\text{meas},k}$ and a phase shifted by $\pi/2$ or $-\pi/2$ relative to $\varphi_{\text{meas},k}$ depending on the rotation direction, as

$$\frac{\partial \tilde{B}_{\text{meas},k}}{\partial t} = i\omega \tilde{B}_{\text{meas},k} = e^{i\pi/2} \omega \tilde{B}_{\text{meas},k} \quad . \quad (3.4)$$

For rotating modes with small toroidal mode numbers, n can be derived from a small number of signals at the same poloidal position θ_{coil} but different toroidal positions ϕ_k , e.g. from two passive coils $k = k_1, k_2$. Here and in the following, the measurements and simulations of only $n = 1$ tearing modes are discussed. Because of toroidicity and shaping, the identification of the poloidal mode number m is more difficult [52]. A poloidally arranged array of passive coils is required to determine m . For coupled modes, the measured signal is composed of different poloidal mode numbers, even when the effect of θ^* is correctly accounted for (cf. section 2.4.2). Separation by Fourier transform is therefore not possible for coupled rotating modes, since the superposition of different harmonic oscillations (with different amplitudes and phases) at the same frequency results in a harmonic oscillation again. Thus, in addition to a poloidal array of coils, determining the poloidal mode composition of rotating modes requires a model that calculates the expected magnetic measurements for different m at the coil positions. This model needs to account for the field line geometry of the resonant surface where the mode is located, and the influence of mirror currents in conducting structures near the passive coils induced by a rotating mode.

When a tearing mode locks with respect to the vessel (cf. section 2.4.3), the temporal component is eliminated. The procedure described above, using a temporal Fourier transform, is not applicable here anymore. Thus, to get the amplitude, $a_{\text{meas},k}$, and the phase, $\varphi_{\text{meas},k}$, at one poloidal coil position θ_{coil} , a toroidal array of passive coils is needed for locked modes in addition. The determination of $a_{\text{meas},k}$ and $\varphi_{\text{meas},k}$ from a toroidal array of coils is described in [53]. Moreover, integrated radial field measurements are required to detect locked modes, since the poloidal magnetic perturbation field of the tearing mode cannot be distinguished from the poloidal component of the equilibrium magnetic field with sufficient precision. Integrating the signal from the magnetic measurements adds another challenge, as the mode signal has to be separated from other changes in the magnetic flux through the coils caused by changes in plasma current, poloidal and toroidal field coils. The investigation of locked modes thus requires the corrected integration of the signals from a toroidal array of radial field coils, which are typically only available at a few poloidal positions.

3.3.2 Passive coils in ASDEX Upgrade

In AUG, different types of coils with different orientations and positions are installed. A poloidal cross-section highlighting the relevant coils used in this work for tearing mode detection is shown in figure 3.4.

Mirnov coils (cf. figure 3.5, left) are installed tangentially to the vacuum vessel, in the welding flange, and measure (mainly) B_θ by nature of their arrangement. These

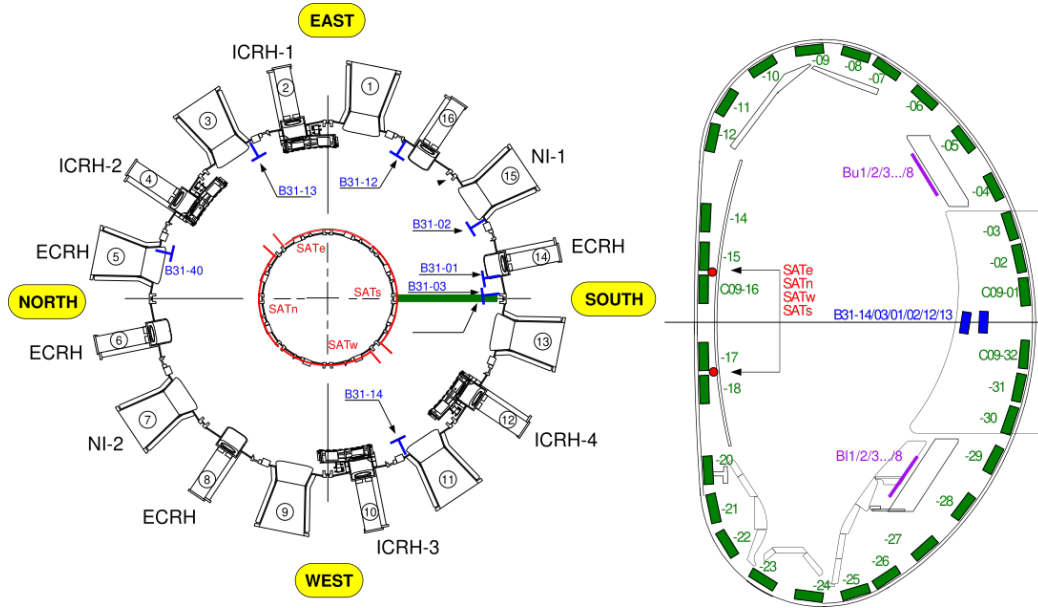


Figure 3.4: Toroidal (left) and poloidal (right) cross-section of AUG including the magnetic measurements used for tearing mode detection. The Mirnov coils ('C09') are indicated in green, the saddle coils in red ('SAT'), the Ballooning coils in blue (B31') and the B-coils in purple ('Bu', 'B1', only in the right plot). The 16 toroidal sectors are numbered in the left plot. The poloidal cross-section (right) shows the projection of all coil types onto one toroidal angle (only 2 Ballooning coils are shown).

coils are 13.1 cm high with 131 turns and an effective coil area of 0.3634 m^2 [54]. We use a poloidal array consisting of 30 coils (green in figure 3.4, labelled 'C09-xx'), sufficient to determine the poloidal mode composition of rotating modes.¹³

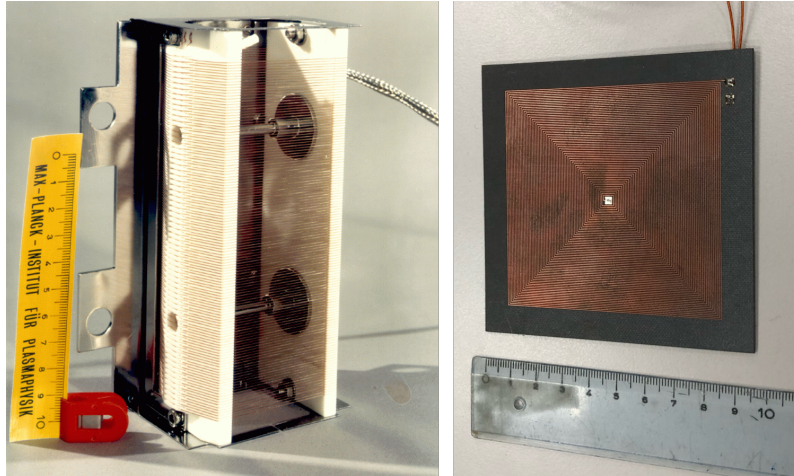


Figure 3.5: Pictures of a Mirnov coil (on the left) and a Ballooning coil (on the right) used in AUG.

The so-called Ballooning coils (cf. figure 3.5, right) measure \dot{B}_r and consist of a planar meander with an effective area of 0.119026 m^2 [54]. We use Ballooning coils at the LFS midplane at different toroidal positions and slightly different major radii (blue in figure 3.4, labelled 'B31-xx'). These are not placed directly in front of a

¹³In AUG there are also toroidally distributed Mirnov coils at the same poloidal position, from which the toroidal mode number can be inferred.

conducting structure and can therefore also be used for rotating modes and give the toroidal mode number. There is no poloidal array of Ballooning coils sufficient to determine the poloidal mode composition.

Four saddle coils on the high field side (HFS) midplane (red in figure 3.4, labelled 'SATx', where 'x' is the coil orientation in the east ('e'), south ('s'), west ('w') and north ('n') directions) with a height of 0.452 m, covering a toroidal angle of $\frac{\pi}{2}$, serve primarily as locked mode detector, although frequencies up to 10 kHz can be observed. Only the difference of measured U_{ind} of each pair of opposite coils (e.g. 'SATew') is recorded, corresponding to an $n = \text{odd}$ filtering. For locked modes, the integration is done in hardware with an integrator constant $\tau_{\text{int}} = 10$ ms and a correction for changes in plasma and coil currents is performed, similar to [55] and references therein.

The upper and lower B-coils (purple in figure 3.4, labelled 'Bux' and 'Blx' where 'x' is the coil number) are installed directly in front of the highly conducting upper and lower Passive Stabilisation Loop (PSL) with a distance of 10 mm and 30 mm, respectively. The PSL is installed in AUG to mitigate, i.e. slow down, a Vertical Displacement Event (VDE).¹⁴ The upper B-coils have an effective area of 1.693 m², the effective area for the lower B-coils is 1.798 m², each with 5 turns.¹⁵ They are designed and primarily used to apply magnetic perturbations to the plasma [56] but they measure magnetic perturbations when not actively used. Their vicinity to the PSL strongly damps frequencies above a few hundred Hz (cf. section 2.4.4). Thus, the detection of rotating modes with the B-coils is often challenging. Subtracting a common noise, e.g. by taking the difference of the measured U_{ind} as done in hardware for the saddle coils, improves the signals. An additional enhancement is achieved by projecting the signals onto the sine and cosine base vectors, with components $e_{\text{sin},i}^n = \sin(n\phi_i)$ and $e_{\text{cos},i}^n = \cos(n\phi_i)$ where ϕ_i is the coil position, as described in [53]. However, the use of B-coil data for rotating modes is strongly limited, as discussed in section 5.2. As the B-coils measure the radial field component and consist of an upper and lower toroidal array of 8 coils each, the integrated data can in principle be used for locked mode detection [53]. However, the integrated data must be corrected for changes in the plasma current and currents in the poloidal field coils.

3.4 Technical aspects

For rotating modes, a temporal Fourier transform is performed and the frequency with the largest amplitude is selected. In order to do this, a manual selection of time intervals with an integer number of mode periods is used, where the signal approximately describes a stationary rotation. The selected time window should also not contain any Edge Localised Mode (ELM), an MHD edge instability that appears recursively in the High confinement mode (H-mode) [57], leading to a rapid loss of plasma particles and energy [58]. ELMs are visible in magnetic measurements and can affect the amplitude and phase determined by temporal Fourier transform. Figure 3.6 shows an example of the magnetic signal $\hat{B}_{\text{meas},k}$ from the Mirnov coil 'C09-11' of discharge 38926, where an ELM is observed at the middle of the time interval. A sinusoidal function corresponding to the first oscillation is displayed

¹⁴Elongated plasmas are prone to axisymmetric perturbations in which the plasma is vertically displaced [6].

¹⁵The calculation of the B-coil area can be found in the Appendix A.3.

to show the change in phase and the distortion in amplitude. The relative phase between the coils before and after the ELM occurs is not changed.

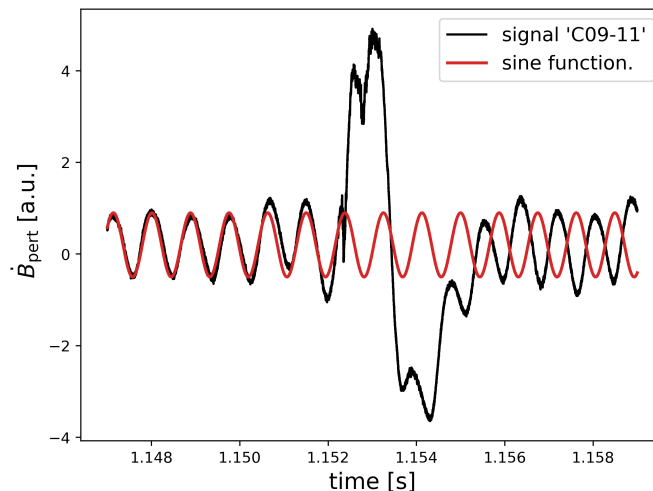


Figure 3.6: Time section of the signal from the Mirnov coil 'C09-11' (back curve) of discharge 38926, where an ELM is visible. For comparison, the sine function $A \sin(\omega t + \phi_0) + \Delta y$, where $A = 0.7$, $\omega = 2\pi \cdot 1145 \frac{1}{s}$, $\phi_0 = -1.4$ rad and $\Delta y = 0.2$, is shown (red).

For uncoupled tearing modes on different q surfaces rotating at different frequencies, the Fourier transform can be used to separate the signals and perform a separate fit of the simulated to the measured coil amplitudes and phases, as described in section 6.1.

In principle, the integrated signal, e.g. the hardware integrated difference signal of the saddle coils, can also be used for rotating modes. However, for hardware integrated data, there is usually a frequency dependence of the integrator which must be known and corrected. We therefore use non-integrated data for rotating modes.

3.5 Necessity for modelling magnetic measurements

As described in section 3.3.2, the poloidal array of Mirnov coils is well suited for observing rotating modes, as they mainly measure B_θ , but they cannot be used for locked modes. On the other hand, most B_r coils in ASDEX Upgrade are not suited to observe fast rotating modes due to the damping close to conducting structures. Thus, for a continuous monitoring of tearing modes in all states, from rotating to locked, both coil types are needed and have to be consistent. To validate this, a comparison is required in the frequency range in which both coil types are applicable and in which shielding currents are important.

Generally, a model is required to determine the complex amplitude, $\tilde{B}_{\text{sim},k}^{(m,n)}$, expected for a coil at a certain coil position and tilt, for a given $\mathbf{j}_{\text{pert}}^{(m,n)}$, especially when shielding currents, induced by a rotating mode, influence the magnetic measurements. These currents also flow in structures which are not toroidally symmetric, necessitating a three-dimensional treatment.

In the following chapter, the three-dimensional model using the FEM is presented, with which we calculate the magnetic perturbation field produced by the individual

base vectors $\mathbf{j}_{\text{pert}}^{(m,n)}$, including the frequency dependent shielding currents in the relevant conducting structures in AUG. This allows the complex amplitudes, $\tilde{a}^{(m,n)}$, of the harmonics, $\mathbf{j}_{\text{pert}}^{(m,n)}$, for coupled $n = 1$ tearing modes to be inferred from magnetic measurements for all mode frequencies.

4 Simulating tearing modes and their measurements with the Finite Element Method (FEM)

Parts of the content, figures and text of this chapter are included in a publication accepted by Plasma Physics and Controlled Fusion (DOI 10.1088/1361-6587/adc0bd) of which the author of this thesis is the first author.

In this work, a model using the FEM and implemented in the GetDP code [59] is developed to solve the electromagnetic problem of a perturbation magnetic field generated by a perturbation current that describes a tearing mode in the presence of induced image currents in passive conductors. This allows for the interpretation of magnetic measurements which for AUG were introduced in section 3.3. In this chapter, a general introduction to FEM is given, followed by a description of the model used in this thesis.

4.1 Theory and formulation of FEM

For solving the partial differential equations of the electromagnetic problem, the FEM is chosen, which discretises the calculation domain into small elements and then solves a simplified model for each element (cf. chapter 7 in [60]). The solution for the whole system is then obtained from the solution for the elements, taking into account the appropriate continuity and equilibrium conditions [61]. It was first introduced by [62] for elastic deformation, where the domain was discretised by a lattice structure. The first mathematical foundations were developed by [63].¹⁶ The method was then further developed (e.g. by [67]), mainly in the field of civil and aeronautical engineering. [68]

In general, the term FEM includes variational methods [69] as well as methods using the weighted residual [70]. In this work, the equations are solved in the weak form [71] using Galerkin's method, which belongs to the category of weighted residuals methods [72]. The reader is referred to [73] for an introduction to the electromagnetic application of FEM, which is used in this thesis and is one of many applications of FEM.

4.1.1 General theory

The basic idea of FEM is to divide the objects of a domain into small finite elements as for example sketched in figure 4.1, where the triangular elements are linear and the nodal points correspond to the corner of the elements.¹⁷ A variable $f(\mathbf{x})$ is then, for example, examined at the nodal points i and the distribution of $f(\mathbf{x})$ over the element is interpolated using a prescribed normalised function $s_i(\mathbf{x})$, called shape function¹⁸,

¹⁶Comparable work was carried out by [64], [65] and [66] during this period (1940s, 1950s).

¹⁷For higher order elements, more nodal points are needed.

¹⁸The shape functions are also called approximation, ansatz, interpolation or basis functions.

that describes the spatial course of the variable. Thus, $f(\mathbf{x})$ is approximated by

$$f(\mathbf{x}) = \sum_i f_i s_i(\mathbf{x}) \quad (4.1)$$

where f_i denotes the unknown quantities – also called multipliers or degrees of freedom – that have to be determined for the element nodes i . The shape functions can be of different order and must be continuous over the elements. In this example, the shape functions are scalar functions associated with nodes, but they can also be associated with edges, facets or volumes. Edge functions for example allow to calculate an unknown vector field via the circulation along the element edges. [74, 72, 75, 59]

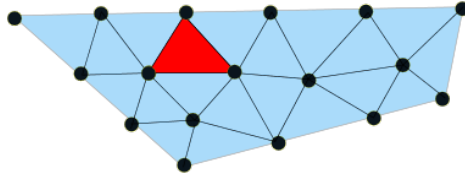


Figure 4.1: Example of an object (blue) that is divided into finite elements where one is shown in red. Here, the nodes i (cf. equation 4.1, black dots) are at the corners of the triangular shaped elements.

For complex structures, it is often sufficient to solve the problem so that the partial differential equations are fulfilled in the weak form for well-chosen test functions. By multiplying the partial differential equation by a test function f' and integrating over the volume Ω , the differential equations can be simplified such that the derivatives are distributed over the unknowns and test functions, which is shown in the example below.

As the same procedure is used repeatedly in the formulation described in section 4.1.2, it is illustrated here in a general example and referred to afterwards. A partial differential equation with an unknown f and an arbitrary scalar function a

$$-\nabla \cdot (a \nabla f) = 0 \quad (4.2)$$

is formulated in the weak form by an inner product with a test function f' over a domain Ω

$$(-\nabla \cdot (a \nabla f), f')_{\Omega} = 0 \quad . \quad (4.3)$$

This inner product can be, for example, the integral

$$\int_{\Omega} (-\nabla \cdot (a \nabla f)) f' \, d\Omega = 0 \quad . \quad (4.4)$$

Problem 4.2 is now reformulated to find f such that equation 4.4 holds for all test functions f' . For differentiable test functions, equation 4.4 is rewritten by means of integration by parts:

$$-\int_{\Omega} \nabla \cdot (a \nabla f f') \, d\Omega + \int_{\Omega} (a \nabla f) \cdot (\nabla f') \, d\Omega = 0 \quad . \quad (4.5)$$

Using the Gaussian integral theorem, we obtain

$$-\int_{\partial\Omega} (a \nabla f f') \cdot \mathbf{n} \, d\Gamma + \int_{\Omega} (a \nabla f) \cdot (\nabla f') \, d\Omega = 0 \quad . \quad (4.6)$$

The integral over the surface $\partial\Omega$, where \mathbf{n} is the normal vector on the surface and $d\Gamma$ is a small surface element, can either be included in the boundary conditions, or test

functions that vanish at the boundary of the domain are chosen so that the surface integral vanishes. In the following, we neglect these surface integrals, assuming that one of the two possibilities is fulfilled. Thus, for a vanishing surface term, we need to find f in the function space such that

$$\int_{\Omega} (a \nabla f) \cdot (\nabla f') \, d\Omega = 0 \quad (4.7)$$

holds for all f' . The discrete approximation of f (equation 4.1) can be inserted into equation 4.7, where in the Galerkin method the shape functions are used as test functions. This gives a system of linear equations that can be solved by numerical methods. [59]

4.1.2 FEM formulation used in this work

For the electromagnetic problem of a perturbation current creating a perturbation magnetic field, the Maxwell equations (cf. equations 2.5, 2.6, 2.7) have to be solved in the weak form, which is done here in the A-V formulation in the frequency domain [59] using the vector potential \mathbf{A} and the electric scalar potential V . \mathbf{A} and V are defined to directly fulfill the requirement that \mathbf{B} is divergence free (equation 2.6) and Faraday's law (equation 2.5). Thus, the magnetic and electric field are expressed as

$$\mathbf{B} = \nabla \times \mathbf{A} \quad (4.8)$$

and

$$\mathbf{E} = -\frac{\partial \mathbf{A}}{\partial t} - \nabla V \quad (4.9)$$

Using these expressions (equations 4.8 and 4.9) and Ohm's law with $\mathbf{v} = 0$ (cf. equation 2.3), Ampère's law, neglecting the displacement current in the low frequency limit (cf. equation 2.7), reads

$$\nabla \times \left(\frac{1}{\mu_0} \nabla \times \mathbf{A} \right) \stackrel{(2.7)}{=} \mathbf{j} \stackrel{(2.3)}{=} \sigma \left(-\frac{\partial \mathbf{A}}{\partial t} - \nabla V \right) + \mathbf{j}_{s0} \quad (4.10)$$

where \mathbf{j}_{s0} is the source current density that represents the perturbation current at the resonant surface .

In this work, equation 4.10 is formulated in the weak form as an integral over the domain Ω (cf. equation 4.4) such that

$$\underbrace{\int_{\Omega} \left(\nabla \times \left(\frac{1}{\mu_0} \nabla \times \mathbf{A} \right) \right) \cdot \mathbf{A}' \, d\Omega}_{\text{I}} + \underbrace{\int_{\Omega} \sigma \left(\frac{\partial \mathbf{A}}{\partial t} + \nabla V \right) \cdot \mathbf{A}' \, d\Omega}_{\text{II}} - \underbrace{\int_{\Omega} \mathbf{j}_{s0} \cdot \mathbf{A}' \, d\Omega}_{\text{III}} = 0 \quad (4.11)$$

where the test functions \mathbf{A}' are vectors in the edge finite element space of the shape functions of \mathbf{A} , allowing to calculate \mathbf{A} via the circulation along the edges of the elements.

Term I of equation 4.11 is rewritten by using the vector identity

$$(\nabla \times \mathbf{c}) \cdot \mathbf{d} = \nabla \cdot (\mathbf{c} \times \mathbf{d}) + \mathbf{c} \cdot (\nabla \times \mathbf{d}) \quad (4.12)$$

with arbitrary vectors \mathbf{c} and \mathbf{d} , and the Gaussian integral theorem, similarly to equations 4.5 to 4.7, for $\mathbf{c} = \nabla \times \mathbf{A}$ and $\mathbf{d} = \mathbf{A}'$, such that the curl is applied to both \mathbf{A} and \mathbf{A}' :

$$\text{I} = \int_{\Omega} \frac{1}{\mu_0} (\nabla \times \mathbf{A}) \cdot (\nabla \times \mathbf{A}') \, d\Omega \quad (4.13)$$

Term II is integrated over the conducting domains with the corresponding conductivities σ .

The source current density \mathbf{j}_{s0} in term III is defined as

$$\mathbf{j}_{s0} = \mathbf{j}_s - \nabla \xi_s \quad (4.14)$$

with a scalar potential ξ_s that fulfills

$$\nabla \cdot (\mathbf{j}_s - \nabla \xi_s) = 0 \quad (4.15)$$

which is formulated as – comparable to equations 4.4 to 4.7 –

$$\int_{\Omega} \nabla \cdot (\mathbf{j}_s - \nabla \xi_s) \xi' \, d\Omega = \int_{\Omega} \mathbf{j}_s \cdot \nabla \xi' \, d\Omega - \int_{\Omega} \nabla \xi_s \cdot \nabla \xi' \, d\Omega = 0 \quad (4.16)$$

where the scalar test function ξ' is an element of the function space called nodal finite element space. Adding $(-\nabla \xi_s)$ to \mathbf{j}_s is necessary because the discretisation of \mathbf{j}_s according to equation 4.1 results in a current density that is, by definition, not divergence-free, and the divergence-free nature of \mathbf{j}_{s0} is fundamental to the robust determination of post-processing quantities such as \mathbf{B} [76].

Like the source current density, the total current density \mathbf{j} must also be divergence free. This is formulated by using the definition of \mathbf{j} as in equation 4.10:

$$\nabla \cdot \sigma \left(-\frac{\partial \mathbf{A}}{\partial t} - \nabla V \right) + \underbrace{\nabla \cdot \mathbf{j}_{s0}}_{\stackrel{(4.15)}{=} 0} = 0 \quad . \quad (4.17)$$

In the weak form after using the Gaussian integral theorem – with the approach of equation 4.4 to 4.7 – equation 4.17 reads

$$\int_{\Omega} \sigma \left(\frac{\partial \mathbf{A}}{\partial t} + \nabla V \right) \cdot \nabla V' \, d\Omega = 0 \quad (4.18)$$

where the test functions V' are in the function space of the sum of the nodal functions.

To ensure the uniqueness of \mathbf{A} , a gauge condition has to be formulated. In this work, the Coulomb gauge is chosen

$$\nabla \cdot \mathbf{A} = 0 \quad , \quad (4.19)$$

which is formulated as (cf. equations 4.4 to 4.7)

$$\int_{\Omega} \mathbf{A} \cdot \nabla \xi' \, d\Omega = 0 \quad , \quad (4.20)$$

where the test functions ξ' are from the nodal finite element space. There exist also other possibilities to impose a gauge condition as for example using the co-tree gauging [73]. For a unique and stable convergence of the solution, Lagrange multipliers are introduced to complement the Coulomb gauge condition [77, 78]. They must be added to equation 4.11 as $\int_{\Omega} \nabla \xi \mathbf{A}' \, d\Omega$, where the shape functions of ξ are elements of the nodal finite element space. [76]

4.2 Model set-up in general

The ONELAB (Open Numerical Engineering LABoratory) software package [79] is chosen as an interface to the Gmesh [80] and GetDP [59] codes. The mesh generator Gmesh automatically generates a tetrahedral mesh fitting to the defined regions with a prescribed characteristic length, i.e. a measure of the mesh fineness at that point. For calculating the magnetic perturbation field generated by a perturbation current representing a tearing mode on the resonant surface and including the induced shielding currents, regions with different properties have to be defined: the source region, where the perturbation current $\mathbf{j}_{\text{pert}}^{(m,n)}$ flows and conducting regions, which represent the relevant conducting structures. The remaining volume, including the plasma, except for the source region, is modelled as a vacuum. The geometry of the model is defined by poloidal cross-sections A_i that are extruded by a specific angle α_i , as shown in figure 4.2, where the simulation coordinate system is introduced. By extruding the poloidal cross sections by several different angles in succession, it is possible to implement structures that are not toroidally symmetrical.

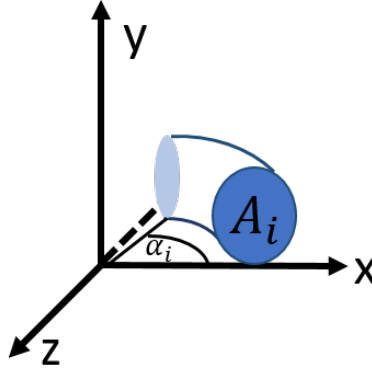


Figure 4.2: Schematic drawing of the coordinate system used in the model, defined so that the y -axis is the height, corresponding to the z -axis in cylinder coordinates, and the z -axis points out of the plane.

The source region, where the perturbation current density flows, is defined as an annulus between two flux surfaces. Even if the source current density is made divergence-free by including $\nabla \xi_s$ (cf. equation 4.15), the ansatz for \mathbf{j}_s needs to be divergence-free (before the discretisation) to ensure a correct physical description. This is achieved by choosing a perturbation current density as defined in equation 2.59 (cf. [30]), as shown below.

Let a poloidal harmonic of the perturbation current density parallel to the equilibrium magnetic field, \mathbf{B}_0 , be defined as

$$\mathbf{j}_{\text{pert}}^{(m,n)} = f(\rho_{\text{pol}}) \mathbf{B}_0 e^{i(m\theta^* - n\phi + \omega t)} \quad , \quad (4.21)$$

where $f(\rho_{\text{pol}})$ is a function that is constant on a magnetic flux surface. Then,

$$\begin{aligned} \nabla \cdot \mathbf{j}_{\text{pert}}^{(m,n)} &= \nabla \cdot \left(f(\rho_{\text{pol}}) \mathbf{B}_0 e^{i(m\theta^* - n\phi + \omega t)} \right) \\ &= \underbrace{(\nabla f(\rho_{\text{pol}})) \mathbf{B}_0 e^{i(m\theta^* - n\phi + \omega t)}}_{=0} + \underbrace{f(\rho_{\text{pol}}) (\nabla \cdot \mathbf{B}_0) e^{i(m\theta^* - n\phi + \omega t)}}_{=0} \\ &\quad + f(\rho_{\text{pol}}) \mathbf{B}_0 \nabla e^{i(m\theta^* - n\phi + \omega t)} \\ &= f(\rho_{\text{pol}}) \mathbf{B}_0 e^{i(m\theta^* - n\phi + \omega t)} (im\nabla\theta^* - in\nabla\phi) \quad . \end{aligned} \quad (4.22)$$

Using the definition of q from equation 2.53, equation 4.22 becomes

$$\nabla \cdot \mathbf{j}_{\text{pert}}^{(m,n)} = f(\rho_{\text{pol}}) e^{i(m\theta^* - n\phi + \omega t)} \mathbf{B}_0 \cdot \nabla \phi \underbrace{\left(\frac{im}{q} - in \right)}_{=0 \text{ for } q=m/n}. \quad (4.23)$$

Thus, $\mathbf{j}_{\text{pert}}^{(m,n)}$ is divergence-free on its resonant $q = m/n$ surface, when defined as in equation 4.21, i.e. the radial width of the current density is constant in ρ_{pol} .

The finite element solver GetDP is then used to solve the electromagnetic problem in the weak form in the frequency domain using the A-V formulation.

The passive coils are not implemented as separate domains, but their flux is post-calculated via the vector potential \mathbf{A} . The magnetic flux through the coil windings is calculated using Stokes integral theorem:

$$\Psi_B = \int_S \mathbf{B} \cdot \mathbf{dS} = \int_S (\nabla \times \mathbf{A}) \cdot \mathbf{dS} = \oint_{\partial S} \mathbf{A} \cdot \mathbf{dl}, \quad (4.24)$$

where S is the coil winding area, \mathbf{dS} is the normal vector on the coil, ∂S is the curve following the coil winding and \mathbf{dl} the vector along the curve ∂S . Thus, the vector potential, \mathbf{A} , is integrated along the lines following the coil turns at their position to obtain the magnetic flux, which can be directly compared with the measurements (cf. equation 3.2). The magnetic flux calculated according to equation 4.24 is divided by the area of the coils to obtain the expected complex measurement amplitudes $\tilde{B}_{\text{sim},k}^{(m,n)}$.

A measure of agreement between $\tilde{B}_{\text{sim},k}^{(m,n)}$ and $\tilde{B}_{\text{meas},k}$ – and also between two vectors of complex coil amplitudes with different simulation properties – is the angle α between the two complex vectors. The angle between two complex vectors \mathbf{c} and \mathbf{d} is defined as:

$$\alpha = \arccos \left(\frac{\text{Abs}\langle \mathbf{c}, \mathbf{d} \rangle}{\|\mathbf{c}\| \|\mathbf{d}\|} \right). \quad (4.25)$$

where $\langle \mathbf{c}, \mathbf{d} \rangle$ is the dot product of \mathbf{c} and \mathbf{d} . α is also a measure to test linear independence and orthogonality.

By calculating $\tilde{B}_{\text{sim},k}^{(m,n)}$ via an integral (equation 4.24), the solution is more robust than evaluating the magnetic perturbation field at a single point. This is due to the fact that, firstly, the gradient of ξ associated with the Coulomb gauge for the vector potential \mathbf{A} (cf. section 4.1.2) is introduced, which leads to \mathbf{A} being continuous over the elements but not continuously differentiable in the first-order calculation. By integrating \mathbf{A} along the lines of the coil turns, the quantity is smoothed and more reliable. Secondly, the magnetic field \mathbf{B} is calculated via $\nabla \times \mathbf{A}$, which introduces additional uncertainties in \mathbf{B} . To test the reliability of the results of Ψ_B , a comparison of the simulated Mirnov results (cf. the model described in section 4.4) has been made between simulations with first-order and second-order test functions. As the angle α between $\tilde{B}_{\text{sim},k}^{(2,1)}$ of the first-order and second-order calculation is very small ($\alpha = 1.34^\circ$), the first-order calculation is used in this work to save computational time.

4.3 Magnetic measurements in a simplified toroidal device with wall

From a cylinder to a torus – as already indicated in section 2.4.4 – the frequency dependence of B_r and B_θ in front of a resistive wall might change. Hence, to study the influence of the toroidal geometry on the magnetic measurements, two models with small and large aspect ratios $A = R_0/r_s$ are implemented. The minor radius of the resonant surface r_s is 0.4 m each, and they have a major radius $R_0 = 1.65$ m and $R_0 = 5.00$ m at the centre of the resonant surface, resulting in $A = 4.12$ for the small and $A = 12.5$ for the large aspect ratio case. Both models use the above described FEM framework and share the same simplified circular geometry except for the major radius R_0 .

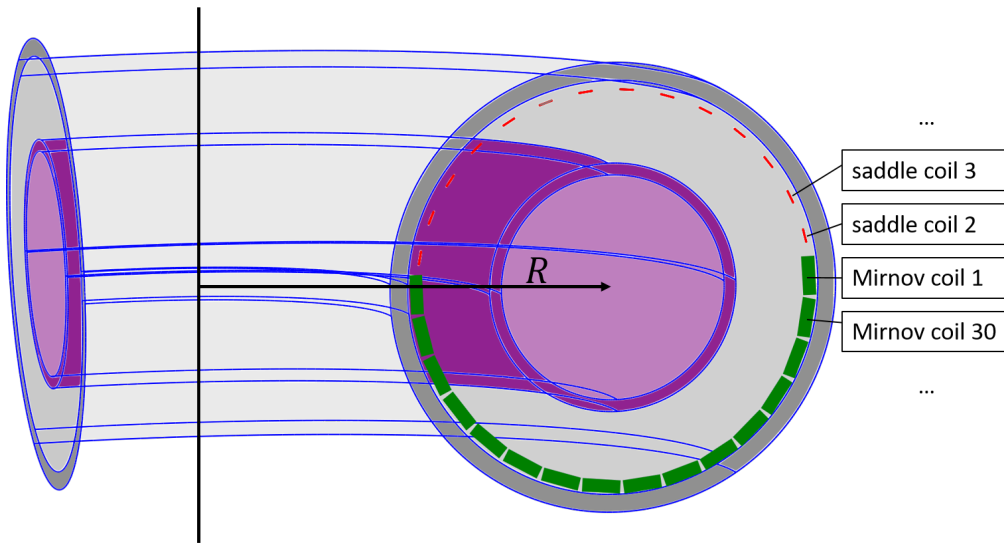


Figure 4.3: Geometry of the circular torus model with the resonant magnetic flux surface in purple and the conducting vessel in grey. The model contains 30 Mirnov coils measuring the poloidal field direction, 16 of which are shown as green boxes, and 30 quadratic saddle coils measuring the radial magnetic field component, 14 of which are indicated as red lines. The coil labelling is indicated by the lettering on the right.

Figure 4.3 shows the model geometry for the low aspect ratio case and the location where the magnetic flux through the virtual coils (cf. equation 3.2) is evaluated. The circular shaped vessel, with radius $r_w = 0.7$ m, a thickness $d_w = 0.06$ m and a conductivity $\sigma_w = 2.0 \cdot 10^5 \frac{1}{\Omega\text{m}}$, is implemented concentrically around the resonant surface. 30 virtual Mirnov coils (cf. section 3.3) and 30 small radial field coils (quadratic coils at the centres of the Mirnov coils) are placed in front of the conducting vessel in the model. The resonant magnetic flux surface is defined with a constant thickness $d_s = 0.04$ m, neglecting the different distance of neighbouring magnetic flux surfaces along the poloidal angle θ in real tokamak plasmas. In this simple geometry model, no correction for constant flux surface thickness is implemented as the frequency dependence of a single coil remains similar.

The tearing mode is described by a helical source current density

$$\hat{j}_{\text{pert,circ}}^{(m,n)} = \frac{\hat{j}_{\text{pert,circ}}}{R} \frac{(-nr) \mathbf{e}_{\theta^*} + mR \mathbf{e}_\phi}{\sqrt{(nr)^2 + (mR)^2}} e^{i(\omega t - n\phi + m\theta^*)} \quad (4.26)$$

where the amplitude of the source current is $\hat{j}_{\text{pert,circ}} = 10^5 \frac{\text{A}}{\text{m}}$. The factor $1/R$

accounts for the variation of B with the major radius R , to reproduce a perturbation current density that is parallel to \mathbf{B}_0 (cf. equations 2.59 and 4.21). In the coordinate system according to figure 4.2, the toroidal vector is

$$\mathbf{e}_\phi = \begin{pmatrix} \sin(\phi) \\ 0 \\ \cos(\phi) \end{pmatrix} \quad (4.27)$$

where $\phi = \arctan\left(\frac{-z}{x}\right)$ and the poloidal vector is defined as

$$\mathbf{e}_{\theta^*} = \begin{pmatrix} -\cos(\phi) \cdot \sin(\theta^*) \\ \cos(\theta^*) \\ \sin(\phi) \cdot \sin(\theta^*) \end{pmatrix} \quad (4.28)$$

where $\cos(\phi) = \frac{x}{R}$ and $\sin(\phi) = -\frac{z}{R}$ with the major radius $R = \sqrt{x^2 + z^2}$. The straight field line angle θ^* is defined according to the Merezhkin formula (equation 2.54) to be also applicable for the large aspect ratio case. The term $(\beta_p + \frac{l_i}{2} + 1)$ is approximated to be 2, leading to $\lambda = 0.48$ and $\lambda = 0.16$ for $\varepsilon = r_s/R = 0.24$ and $\varepsilon = 0.08$, respectively.

Figure 4.4 shows the perturbation current density for $(m = 2, n = 1)$ on its resonant surface, leading to a perturbation magnetic field and the induction of mirror currents in the circular wall. The resulting magnetic flux through the virtual coils (cf. figure

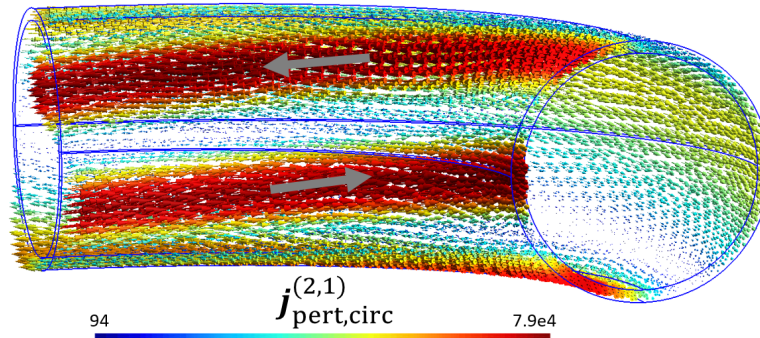


Figure 4.4: Source current density $\mathbf{j}_{\text{pert,circ}}^{(2,1)}$ on the circular surface. Red values mark extreme values and the direction is indicated by the grey arrows.

4.3) is evaluated according to equation 4.24. The virtual saddle coils are implemented as a square winding of 4.5 cm length, the dimensions of the virtual Mirnov coils are the same as those of AUG. In the model, they consist of 5 turns equally distributed across the height of the Mirnov coil. The amplitude of the simulated magnetic measurements of the virtual coils are shown in figure 4.5 depending on the frequency. For the sake of clearness, the virtual measurements of only 16 coils each are shown. Both the saddle and the Mirnov coils are labelled with numbers beginning with 1 at the LFS midplane. The coils labelled with 16 (red and blue) are those at the HFS midplane. The frequency dependence of the saddle coils, measuring B_r , and of the Mirnov coils, measuring B_θ , for the large aspect ratio case (right plot of figure 4.5) is very similar to the magnetic field components obtained from the cylindrical formula (cf. equations 2.64 and 2.65 and figure 2.8). However, the frequency dependence of the amplitudes measured by the virtual coils on the HFS changes for the low aspect ratio case for small frequencies (left plot of figure 4.5). This indicates that the distribution of the perturbation current according to θ^* leads to a non-monotonic frequency dependence of B in front of a resistive wall on the HFS, where the minima

and maxima of the perturbation current density are closer to each other. In a torus, the vacuum vessel can no longer be considered as a flux surface, which becomes even more pronounced for realistic resonant surface and vessel geometries (cf. section 4.4).

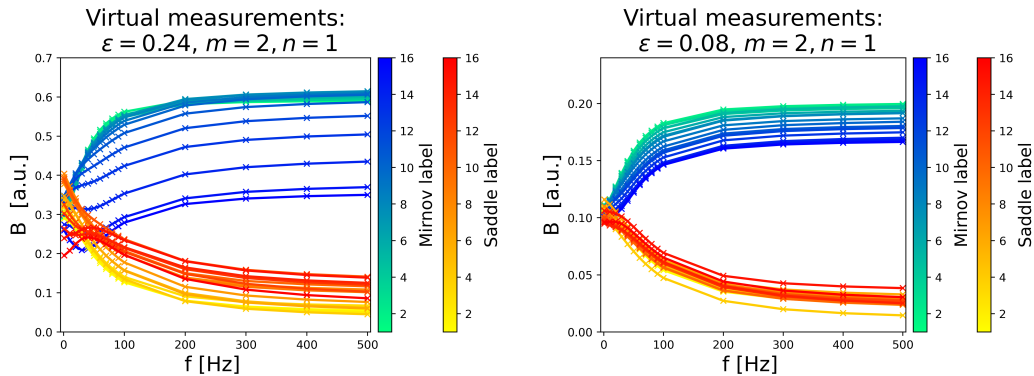


Figure 4.5: Amplitude of the magnetic field of a mode described by $\hat{j}_{\text{pert,circ}}^{(2,1)}$ measured by 16 virtual Mirnov (cyan to blue) and saddle coils (yellow to orange) for the small (left) and large (right) aspect ratio cases depending on frequency. The coil labelling starts – as indicated in figure 4.3 – on the LFS with index 1.

In order to capture not only the effects of toroidicity, but also the effects of shaped resonant surfaces, a non-circular vacuum vessel and other conducting structures within the vessel, a more sophisticated model geometry is described in the following section 4.4 and used in the remainder of this work.

4.4 Model description: ASDEX Upgrade

In order to obtain a realistic simulation of the magnetic measurements, the geometry of the resonant surface is taken from the equilibrium reconstruction^{19,20} and the conducting structures are implemented in such a way that they cover the most important effects on the magnetic measurements used here. Although a quarter of the torus would be sufficient to model $n = 1$ tearing modes, we use half of the torus, from segment 13 to segment 4 (cf. figure 3.4 on the left), so that the poloidal array of Mirnov coils, a saddle and two upper and lower B-coils each can be calculated directly.

4.4.1 Source region

The currents defined in the source regions (cf. figure 4.6) are the perturbation current basis vectors for single helicities localised around the respective resonant surfaces with positive mode numbers m , n :

$$\hat{j}_{\text{pert}}^{(m,n)} = \hat{j}_0 g(\rho_{\text{pol}}) \mathbf{B}_0 e^{i(\omega t - n\phi + m\theta^*)} \quad (4.29)$$

¹⁹In most cases, the equilibrium reconstruction is based on the CLISTE code [33]. If indicated, the IDE code [34] is used instead.

²⁰As explained in section 3.4, the time intervals are chosen manually to ensure an appropriate amplitude and phase determination of the magnetic measurements from the temporal Fourier transform. To ensure a reliable equilibrium reconstruction, times when the equilibrium changes little are chosen, resulting in the times used for the equilibrium reconstruction sometimes not being exactly in the time window used for the Fourier transform.

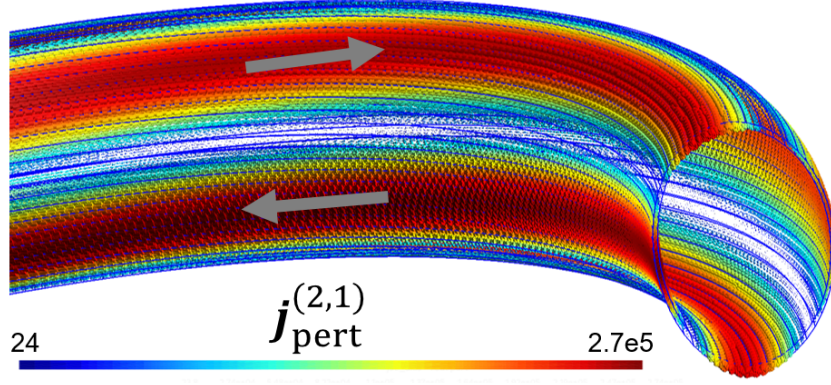


Figure 4.6: Source current density for $m = 2$, $n = 1$ on the resonant $q = 2$ surface for discharge 41091 at 6.05 s used as a base vector to describe a tearing mode. Red colors mark extreme absolute values, the grey arrows indicate the direction of the perturbation current density.

where $\hat{j}_0 = 10^5 \frac{A}{m^2 T}$ is defined to be the (fixed) amplitude and

$$g(\rho_{\text{pol}}) = \begin{cases} 1 & \text{if } (\rho_{\text{pol},m} - \Delta\rho_{\text{pol}}) < \rho_{\text{pol}} < (\rho_{\text{pol},m} + \Delta\rho_{\text{pol}}) \\ 0 & \text{otherwise} \end{cases} .$$

The radial coordinate $\rho_{\text{pol},m}$ is the magnetic flux surface label (equation 1.5) at the resonant $q = \frac{m}{n=1}$ surface. Using ρ_{pol} as radial coordinate allows to define the thickness of the source region $\Delta\rho_{\text{pol}}$ in a natural way. This is equivalent to using a constant thickness in r and modulating the amplitude of $\mathbf{j}_{\text{pert}}^{(m,n)}$ by $\frac{1}{RB_\theta}$ as in [29]. The geometry of the resonant surface is taken from an equilibrium reconstruction and $\Delta\rho_{\text{pol}} = 0.01$ is chosen. The ansatz (equation 4.29) describes a divergence-free perturbation current density on its resonant $q = \frac{m}{n}$ surface as shown in equation 4.22.

The equilibrium magnetic field, \mathbf{B}_0 , is calculated according to

$$\mathbf{B}_0 = (-1)^l \sqrt{B_{R,0}^2 + B_{z,0}^2} \mathbf{e}_\theta + B_{\phi,0} \mathbf{e}_\phi \quad (4.30)$$

where $B_{R,0}$, $B_{z,0}$ and $B_{\phi,0}$ are the magnetic field components from the equilibrium reconstruction in cylinder coordinates. As the poloidal magnetic field of the equilibrium, $B_{\theta,0}$ with $|B_{\theta,0}| = \sqrt{B_{R,0}^2 + B_{z,0}^2}$, can be positive or negative depending on the direction of I_p (and $B_{\phi,0}$), the factor $(-1)^l$ is introduced where l can be an odd or an even number. For a standard $(I_p, B_{\phi,0})$ configuration, l is an even number. The toroidal unit vector, \mathbf{e}_ϕ , is defined according to equation 4.27 and the poloidal unit vector is

$$\mathbf{e}_\theta = \begin{pmatrix} -\cos(\phi) \cdot \sin(\theta) \\ \cos(\theta) \\ \sin(\phi) \cdot \sin(\theta) \end{pmatrix} \quad (4.31)$$

where $\sin(\theta) = \frac{y-z_0}{r}$ and $\cos(\theta) = \frac{R-R_0}{r}$ with z_0 and R_0 being the z coordinate and the major radius, R , on the magnetic axis. The minor radius is $r = \sqrt{(y-z_0)^2 + (R-R_0)^2}$.

For poloidal sidebands $\mathbf{j}_{\text{pert}}^{(m_1,n)}$ on a $q = m_2/n$ surface where $m_1 \neq m_2$, i.e. non-resonant poloidal harmonics, the perturbation current density ansatz (equation 4.29)

is not divergence free. As the source current density is corrected to be divergence-free by the code (cf. equation 4.15), it has to be checked whether the resulting \mathbf{j}_{s0} correctly describes the non-resonant poloidal harmonic. Thus, for comparison, the factor

$$b = \frac{m}{q n} \quad (4.32)$$

is introduced as a weighting factor of the toroidal magnetic field component, so that equation 4.30 becomes

$$\mathbf{B}_0 = (-1)^l \left(\sqrt{B_{R,0}^2 + B_{z,0}^2} \mathbf{e}_\theta + B_{\phi,0} b \mathbf{e}_\phi \right) \frac{\sqrt{B_{R,0}^2 + B_{z,0}^2 + B_{\phi,0}^2}}{\sqrt{B_{R,0}^2 + B_{z,0}^2 + (b B_{\phi,0})^2}}, \quad (4.33)$$

where the ratio accounts for a different perturbation amplitude for $b \neq 1$. On its own resonant $q = m_1/1$ surface, the factor b is one for $\mathbf{j}_{\text{pert}}^{(m_1,1)}$. A comparison between the simulated Mirnov amplitudes and phases of $\mathbf{j}_{\text{pert}}^{(1,1)}$ on the $q = 2$ surface with $b = 1$ and $b = 1/2$, which are both corrected to be divergence-free by the code (equation 4.15), is described in section 4.4.3. As will be shown in section 4.4.3, the resulting amplitudes and phases are very similar, so that b is set to 1 for the sidebands as well.

4.4.2 Conducting regions

The rotating perturbation current density induces mirror currents in the conducting structures, which influence the magnetic perturbation field and hence the magnetic measurements. It is therefore important to include the relevant conducting structures in the vicinity of the passive coils to infer the amplitude of $\mathbf{j}_{\text{pert}}^{(m,n)}$.

The vacuum vessel as largest conducting region is implemented as toroidally symmetric wall with an increased thickness to avoid the need for a very fine mesh in the area of the wall. An effective conductivity $\sigma_{\text{vessel,eff}} = 2.0 \cdot 10^5 \frac{1}{\Omega\text{m}}$ is chosen to account for the increase in resistivity due to holes, ducts and different materials. The procedure for determining this effective conductivity is described in section 4.6.2. The geometry of the vessel is defined as the contour of the inner flange (welding flange) between the segments, as the Mirnov coils are installed in front of this contour. The shape is defined by four circle segments (cf. table 4.1, dotted lines in figure 4.7) and is shown in figure 4.7 together with an overview of the different coil types and other conducting structures included in the simulation. The mirror currents induced in the vacuum vessel mainly influence the measurements of the Mirnov and saddle coils due to their proximity to the conducting structure.

i	centre of the circle segment		radii of the contour		starting angle
	$R_{c,i}$	$z_{c,i}$	$r_{\text{in},i}$	$r_{\text{out},i}$	θ_i
1	1.0829	0.0	1.455	$1.455 + d_w$	-1.0252
2	1.5449	0.7608	0.565	$0.565 + d_w$	1.0252
3	12.283	0.0	11.33	$11.33 + d_w$	3.0709
4	1.5449	-0.7608	0.565	$0.565 + d_w$	3.2123

Table 4.1: Coordinates, $R_{c,i}$ and $z_{c,i}$, of the centre of the four circle segments together with their inner and outer radii, $r_{\text{in},i}$ and $r_{\text{out},i}$, and poloidal angles, θ_i , that define the starting angle of each segment. A wall thickness $d_w = 6$ cm is defined.

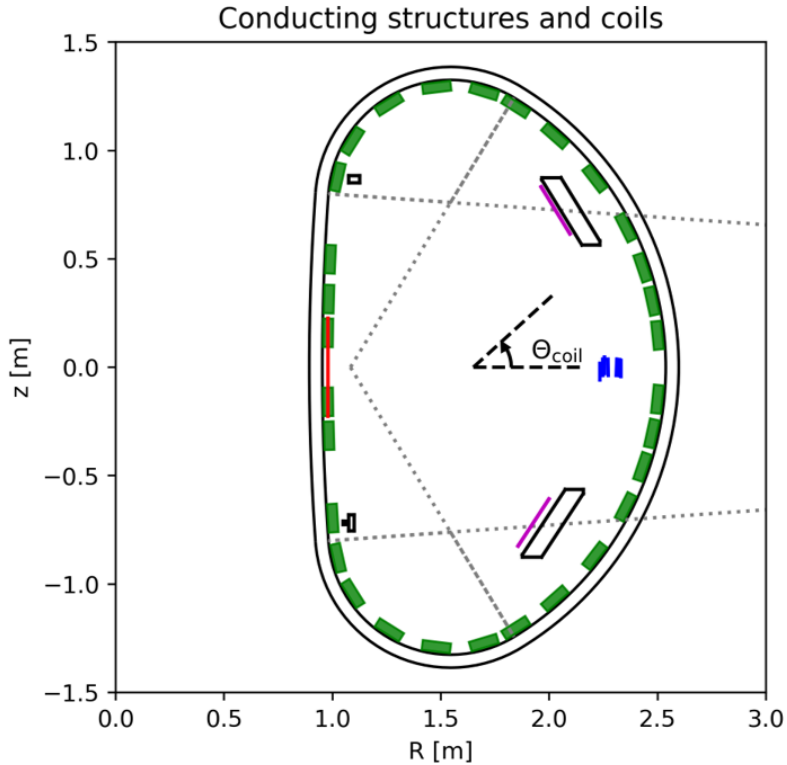


Figure 4.7: Poloidal cross-section of the geometry used in the model: The vacuum vessel and additional conducting structures (upper and lower loop of the PSL on the LFS, and support structures on the HFS, cf. figure 4.8) are drawn in black. The 4 circle segments are marked by dotted lines as the connection between $(R_{c,i}, z_{c,i})$ and the inner contour of the vessel at the angles θ_i (cf. table 4.1). The included coil types are the Mirnov coils indicated as green boxes, the saddle (red) and upper and lower B-coils (magenta) marked by a line. The Ballooning coils are projected onto this poloidal plane and shown as blue lines. The support bridges for mechanical stabilisation of the PSL (cf. figure 4.8) are implemented in the model, but not shown in this figure. The angle θ_{coil} describes the poloidal coil positions with respect to the geometric centre at $R_0 = 1.65$ m, $z_0 = 0$ starting with 0 on the LFS midplane.

The upper and lower PSL (cf. figures 4.7 and 4.8), which is installed in AUG to mitigate vertical displacement events, is a highly conducting region (copper with $\sigma = 5.77 \cdot 10^7 \frac{1}{\Omega\text{m}}$) that strongly affects the B-coils that are directly mounted to it but also those Mirnov coils that are located behind the upper or lower PSL loop. We will show in 4.4.4 that the shielding currents induced in the PSL by tearing modes with $n \geq 1$ are significantly modified by the implementation of support bridges (cf. figure 4.13) that primarily stabilise the PSL mechanically (cf. figure 4.8).

Support bridges with a toroidal distance of $\frac{\pi}{4}$ each are implemented as a circular connection between the upper and lower PSL loops with the centre of the circle at $R = 1.651$ m and $z = 0.0341$ m and an extrusion angle of 2.73° .²¹ In AUG, the current bridge (indicated in figure 4.8, installed between sectors 7 and 8 in figure 3.4) replaces one of the support bridges. The effect of the current bridge can be

²¹For constructional reasons, two of the support bridges were replaced by two new bridges each in AUG. The simulation retains the original configuration of support bridges with a toroidal distance of $\frac{\pi}{4}$ to avoid the need to compute a full torus model. Note that the shape of the support bridges is approximated in the simulation.

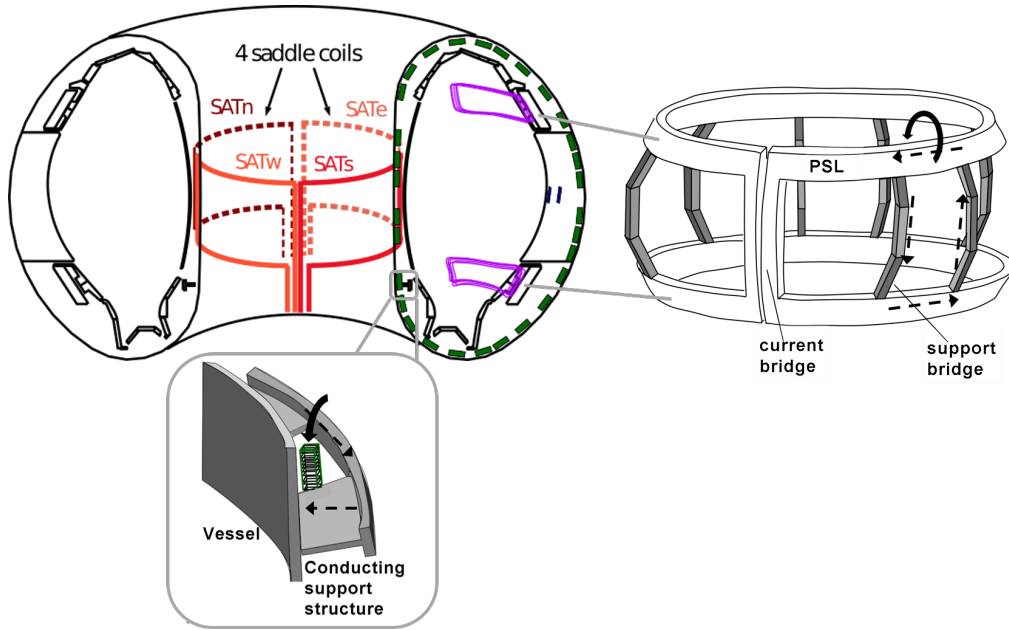


Figure 4.8: Schematic drawing of the vessel and the coils extended in toroidal direction. The PSL with support bridges in grey is sketched on the right and a support structure on the lower part of the torus, which has an electrical connection to the vacuum vessel, is shown as an inlay in the lower figure. The second support structure on the HFS, that is included in the model, is not depicted here. The dotted arrows in the PSL and the support structures represent induced mirror currents, the solid bent arrow indicates the corresponding magnetic field. There is also a Mirnov coil shown in the lower figure, indicated by the green box with black windings.

taken into account in the simulation, which has been studied in detail in [81], but has no significant effect on the magnetic measurements considered here. Additional conducting structures on the HFS with an electrical connection to the vacuum vessel influence the magnetic measurements of nearby Mirnov coils. They are implemented as conducting regions (cf. figure 4.7 and 4.8) with a connection to the wall at every eighth of the torus.²² The electrical conductivity of the additional support structures and bridges is assumed to be $\sigma = 2 \cdot 10^6 \frac{1}{\Omega\text{m}}$ to be in the order of magnitude of the electrical conductivity of steel.

As described in section 2.4.4, the mirror currents in a circular wall induced by a rotating perturbation current density can be calculated in the cylindrical approximation according to equation 2.60, where the resistive timescale of the wall τ_w determines the frequency dependence of j_w . To infer an estimation of τ_w , the toroidal wall currents in the simulation are calculated as an integral over the volume of the wall according to

$$I_{w,\phi} = \int_{\text{wall}} dV \frac{|\sigma \mathbf{E} \cdot \mathbf{e}_\phi|}{R \alpha_{\text{extr}}} \quad (4.34)$$

for different rotation frequencies ω . Equation 4.34 describes the integrated projection of the wall current density onto the toroidal direction (cf. equation 4.27) divided by the 'curve length' of the vessel in the simulation, $R \alpha_{\text{extr}}$, where α_{extr} is the extrusion angle. Using equations 2.60, 2.61 and 2.62, the function

$$I_w = |j_w| d_w \quad (4.35)$$

²²The geometry of the T-shaped structure (cf. inlay of figure 4.8) is simplified in the model. The same applies to the square-shaped conducting component, which is installed in AUG per segment, including gaps.

can be fitted to the simulated $I_{w,\phi}$ to obtain τ_w . Note that even if the wall has only one mesh element in its thickness, it still has some resolution in the direction of the wall thickness, which is achieved by interpolating between the results at the front and back of the wall.

Figure 4.9 shows the simulation results for $I_{w,\phi}$ induced by $m = 2$ and $m = 3$ poloidal harmonics depending on frequency. The geometry of the $q = 2$ and $q = 3$ surface were taken from the equilibrium reconstruction of discharge 38706 at 3.0 s. The resistive timescale τ_{wall} to obtain the best fit is found to be $\tau_w = 2.3$ ms for $\mathbf{j}_{\text{pert}}^{(2,1)}$ and $\tau_w = 1.6$ ms for $\mathbf{j}_{\text{pert}}^{(3,1)}$. Thus, $(\tau_w m)$ results in approximately 5 ms, which is similar to 7 ms obtained by [82]. In [21], a mean resistive wall timescale $\tau_w m = 0.73$ ms was found.

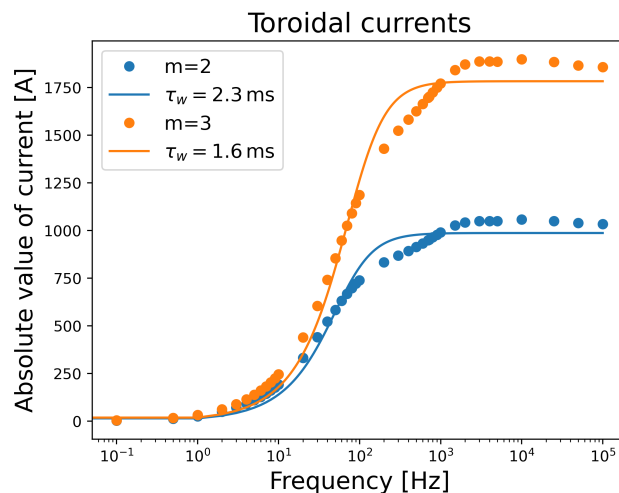


Figure 4.9: Toroidal currents in the vessel calculated according to equation 4.34 for $\mathbf{j}_{\text{pert}}^{(2,1)}$ (blue dots) and $\mathbf{j}_{\text{pert}}^{(3,1)}$ (orange dots) using the geometry of the equilibrium reconstruction of the $q = 2$ and $q = 3$ surfaces of discharge 38706 at $t = 3$ s. The corresponding fits according to equation 4.35 are shown as solid lines. The best τ_w is given in the legend.

4.4.3 Virtual magnetic measurements

As described in section 4.2, the simulated magnetic measurements are evaluated in the post-processing (cf. equation 4.24). In the simulation, the saddle coil consists of one turn corresponding to the saddle coil 'SATE' in AUG (cf. section 3.3). The B-coils 'Bu1', 'Bl1', 'Bu8' and 'Bl8' are simulated with one turn at the position of the middle turn of the corresponding B-coil.²³ The Mirnov coil measurements are modelled as the average of 5 turns equally distributed across the length of the coil, as shown in figure 4.10. The Ballooning coils are simulated with the outermost turn.²⁴ The number of turns of the Mirnov and Ballooning coil measurements in the simulation was found to be sufficient, as the modelled complex amplitudes do not change with an increased number of turns.

²³As the area of the B-coils used in the recorded integrated data is 0.396 m^2 per turn, this value is also taken to calculate the magnetic field from the magnetic flux through the coils for simulated and non-integrated measured data.

²⁴The contour of the Mirnov and Ballooning coils used to evaluate the magnetic flux in the simulation can be found in the Appendix A.1 and A.2.

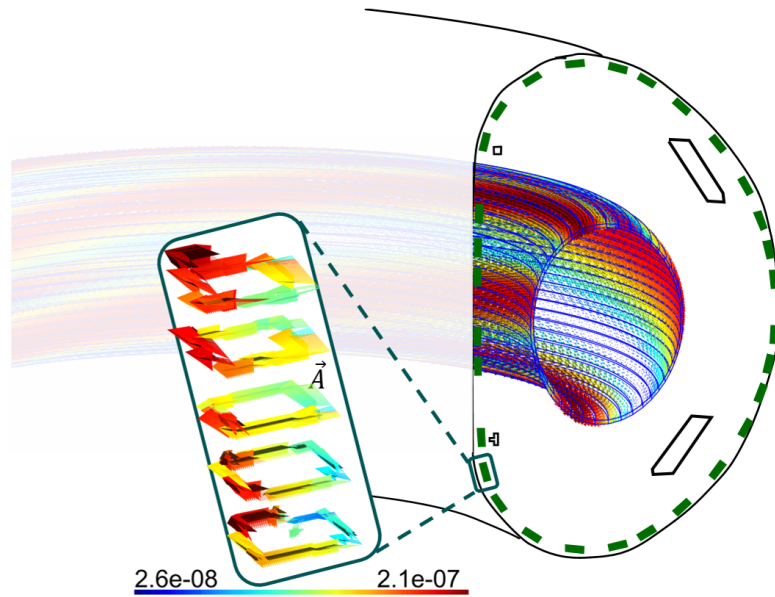


Figure 4.10: Illustration of the evaluation of the simulated Mirnov coil measurements. The vector potential, \mathbf{A} , is evaluated along 5 turns evenly distributed over the length of the Mirnov coil (green box) to calculate the magnetic flux (cf. equation 4.24).

Figure 4.11a) shows the simulated amplitudes, $a_{\text{sim},k}^{(m,1)}$, and phases, $\varphi_{\text{sim},k}^{(m,1)}$, of all k Mirnov coils generated by poloidal harmonics $\mathbf{j}_{\text{pert}}^{(m,1)}$ rotating at 719 Hz with $m \in \{2, 3, 4\}$ at the respective $q = m/1$ surfaces. The poloidal amplitude variation arises mainly due to the different distances of the Mirnov coils to the resonant surfaces, but also due to the different influence of the mirror currents in the conducting in-vessel components. As the $q = 4$ surface is closest to the plasma boundary and hence to the (virtual) measurements, the Mirnov amplitudes for $m = 4$ have the largest amplitude. The simulated coil phases span approximately $m \cdot 2\pi$. The influence of the non-circular geometry including induced currents in the conducting structures is visible in both $a_{\text{sim},k}^{(m,1)}$ and $\varphi_{\text{sim},k}^{(m,1)}$.

The same applies to the simulated amplitudes and phases of the radial field coils. $a_{\text{sim},k}^{(m,1)}$ and $\varphi_{\text{sim},k}^{(m,1)}$ for the upper and lower B-coils and the saddle coil is shown in figure 4.11b). Depending on the mode frequency, not only the different distance between the virtual coils and the resonant surface contributes to the different $a_{\text{sim},k}^{(m,1)}$, but also the stronger damping of the B-coils (at $\theta_{\text{coil}} = 1.1$ and 5.0) due to mirror currents induced in the PSL.

The simulated amplitudes and phases of the toroidal Ballooning coils are shown in figure 4.11c). Note that the Ballooning coils are installed with slightly different tilting angles at different toroidal angles ϕ_{coil} at the LFS midplane ($\theta_{\text{coil}} = 0$). Thus, the phase dependence on ϕ_{coil} is almost the same for all poloidal harmonics due to the same toroidal mode number $n = 1$. The phase spans about 60% of $n \cdot 2\pi$, since the toroidal cover of ϕ_{coil} is $3.99 \approx 60\% 2\pi$.

Since there is no $q = 1$ surface in many equilibrium reconstructions, although a $q = 1$ surface exists, often inferred from the presence of sawteeth²⁵, the poloidal harmonic

²⁵The sawtooth instability describes a periodic relaxation of temperature and density in the plasma core, usually with an accompanying ($m = 1, n = 1$) mode at the $q = 1$ surface (cf. chapter 4 in [12]).

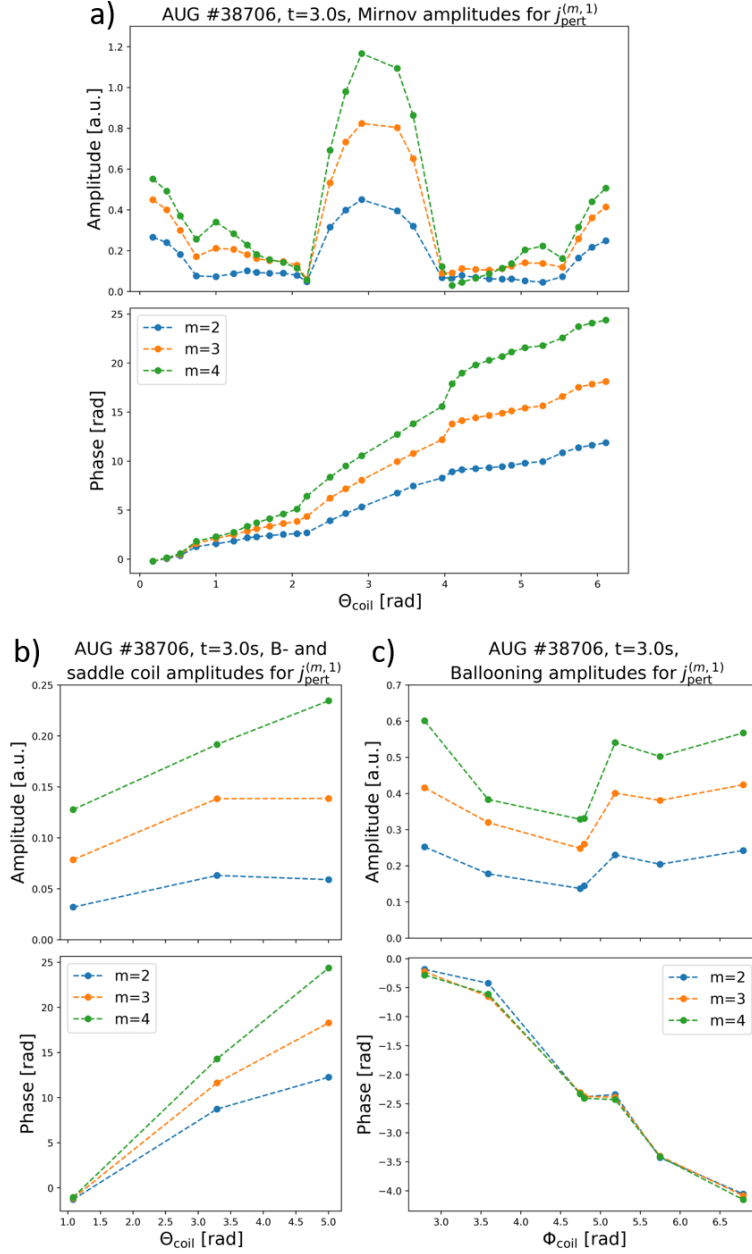


Figure 4.11: Amplitudes (upper row in each subfigure) and phases (lower row) of the complex amplitudes $\tilde{B}_{\text{sim},k}^{(m,1)}$ of the poloidal array of Mirnov coils (figure a)), the upper and lower B-coils together with the saddle coil (figure b), which are at slightly different toroidal positions ϕ_{coil} and the toroidal Ballooning coils (figure c)) for $m \in \{2, 3, 4\}$ as a function of the coil position, θ_{coil} and ϕ_{coil} (at $\theta_{\text{coil}} = 0$). The individual coil amplitudes and phases (dots) are connected with a dashed lines as a guidance for the eye only. The geometry of the resonant $q = m/1$ surface is taken from the equilibrium reconstruction of discharge 38706 at $t = 3.0$ s.

$\tilde{j}_{\text{pert}}^{(1,1)}$ is simulated on the $q = 2$ surface. As announced in section 4.4.1, the virtual Mirnov results of $\tilde{j}_{\text{pert}}^{(1,1)}$ calculated according to equations 4.29 and 4.33 with $b = 1$ and with $b = 1/2$ are compared in figure 4.12. The resulting Mirnov amplitudes and phases are almost identical, which is also reflected in a very small $\alpha = 0.45^\circ$. Thus, the correction by the code via $\nabla \xi_s$ to make \tilde{j}_s divergence-free (cf. equation

4.15), results in the same virtual measurements as using equation 4.33 with $b = 1/2$. Therefore the equation 4.30 is also used to calculate the virtual measurements of $j_{\text{pert}}^{(1,1)}$ on the $q = 2$ surface.

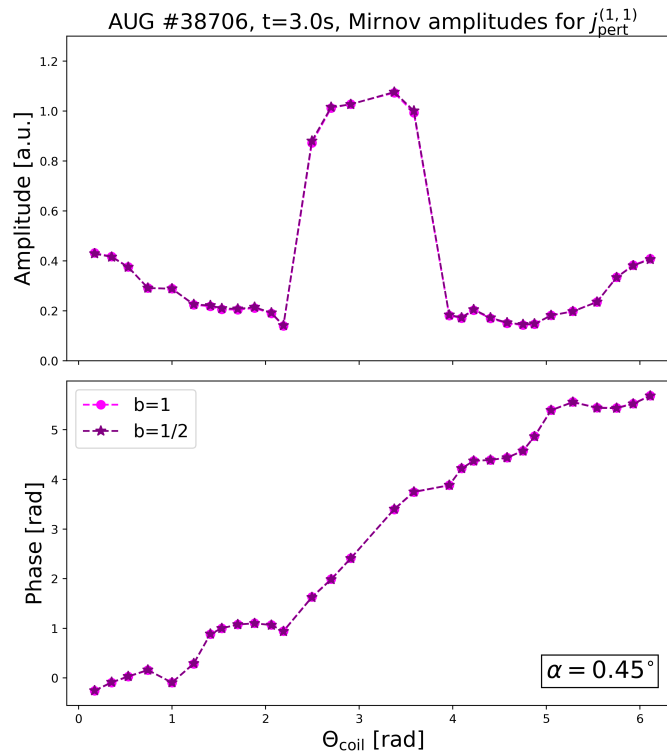


Figure 4.12: Comparison of simulated Mirnov amplitudes $a_{\text{sim},k}^{(1,1)}$ and phases $\varphi_{\text{sim},k}^{(1,1)}$ of an $m = 1$ poloidal harmonic at the $q = 2$ surface for $b = 1$ and $b = 1/2$ (cf. equation 4.33). The angle α between the $\tilde{B}_{\text{sim},k}^{(1,1)}$ is given in the lower right corner.

4.4.4 Influence of conducting structures

The effect of the support bridges, which mechanically stabilise the PSL loops, and the additional conducting structures on the HFS is demonstrated below using the example of the Mirnov coils due to their high coverage in poloidal direction. Figure 4.13 shows the comparison between $\tilde{B}_{\text{meas},k}$ and $\tilde{B}_{\text{sim},k}^{(2,1)}$ for the Mirnov coils for two different models: one with wall and PSL only and one with wall, PSL and additionally the support bridges and structures on the HFS. The angle α (equation 4.25) is used to test the agreement of $\tilde{B}_{\text{sim},k}^{(2,1)}$ with $\tilde{B}_{\text{meas},k}$. The case shown in figure 4.13 with only $j_{\text{pert}}^{(2,1)}$ and no support structures gives $\alpha = 26.9^\circ$, including the support structures improves the agreement to $\alpha = 16.0^\circ$. The importance of including the support bridges and the additional conducting structures on the HFS in addition to the wall and the PSL is clearly visible in order to reproduce the observed damping of $a_{\text{meas},k}$ in the poloidal regions marked in figure 4.13. Although $\varphi_{\text{sim},k}^{(2,1)}$ is slightly changed by implementing the additional structures, the main change is observed in $a_{\text{sim},k}^{(2,1)}$.

The influence of the vacuum vessel, the PSL and support structures connected to the wall on the HFS has already been discussed in [29] in the fast rotating limit in 2D with $n = 0$. Also in the 3D simulation described in this work, $\tilde{B}_{\text{sim},k}^{(2,1)}$ around $\theta_{\text{coil}} = 2$ rad and $\theta_{\text{coil}} = 4$ rad are improved by the implementation of the in-vessel

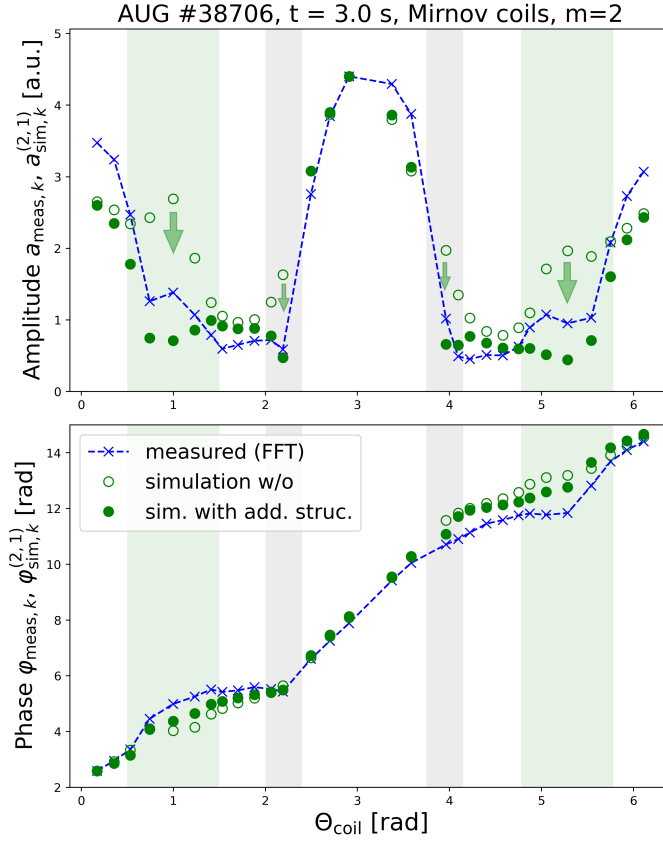


Figure 4.13: Comparison of $\tilde{B}_{\text{meas},k}$ (blue crosses) with $\tilde{B}_{\text{sim},k}^{(2,1)}$ of the Mirnov coils generated by $\mathbf{j}_{\text{pert}}^{(2,1)}$. Open green circles show $\tilde{B}_{\text{sim},k}^{(2,1)}$ with only the vessel and the PSL loops included, full green circles with the additional conducting structures (support bridges, in-vessel components on HFS). The measured amplitudes and phases are connected by dashed lines for guidance only. The amplitudes of the simulations are multiplied by a constant factor such that the maximal values agree, the simulated phase is shifted to match the measured phase of the Mirnov coil at the smallest θ_{coil} . Including the additional conducting structures reduces $\tilde{B}_{\text{sim},k}^{(2,1)}$ behind the PSL (transparent green) and near the HFS support structures (transparent grey) (indicated by the green arrows). This improves the agreement with $\tilde{B}_{\text{sim},k}^{(2,1)}$ significantly.

components on the HFS (cf. figure 4.13). The inlay of figure 4.8 shows the induced currents (dotted arrows) building a loop between support structure and vacuum vessel. The resulting magnetic field (solid black arrow) influences the Mirnov coils in the vicinity of these support structures.

The experimentally observed influence of the PSL requires the consideration of the support bridges, which were not relevant in 2D, but become crucial in the 3D case with $n > 0$. $\tilde{B}_{\text{meas},k}$ of the Mirnov coils behind the PSL at positions around $\theta_{\text{coil}} = 1$ rad and $\theta_{\text{coil}} = 5$ rad cannot be reproduced, if the support bridges are not included. As indicated in the right drawing of figure 4.8, the support bridges are required to close the loop of the induced currents between the upper and lower PSL (black dotted arrows) in order to reproduce the damping of $a_{\text{meas},k}$ of the coils k behind the PSL.

However, $\tilde{B}_{\text{sim},k}^{(2,1)}$ from the simulation with all the conducting structures discussed above with only $\mathbf{j}_{\text{pert}}^{(2,1)}$ cannot fully reproduce the $\tilde{B}_{\text{meas},k}$ of all Mirnov coils. Other poloidal harmonics have to be included in order to match the measurements. The

determination of amplitudes and phase relations of the poloidal harmonics of \mathbf{j}_{pert} is described in in section 4.5.

The frequency dependence of the saddle coil and several simulated Mirnov amplitudes is shown in figure 4.14. As already observed with the simplified toroidal geometry (cf. section 4.3, figure 4.5), the frequency evolution can be non-monotonic for magnetic measurements near the wall on the HFS in toroidal geometry with a perturbation current density distribution along θ^* . Here, the virtual Mirnov measurements, of which 16 are shown, also have different amplitudes and frequency behaviours due to the shaped geometries of the resonant surface and the wall with different distances between the resonant surface and the virtual Mirnov coils, and due to the additional conducting structures within the vacuum vessel.

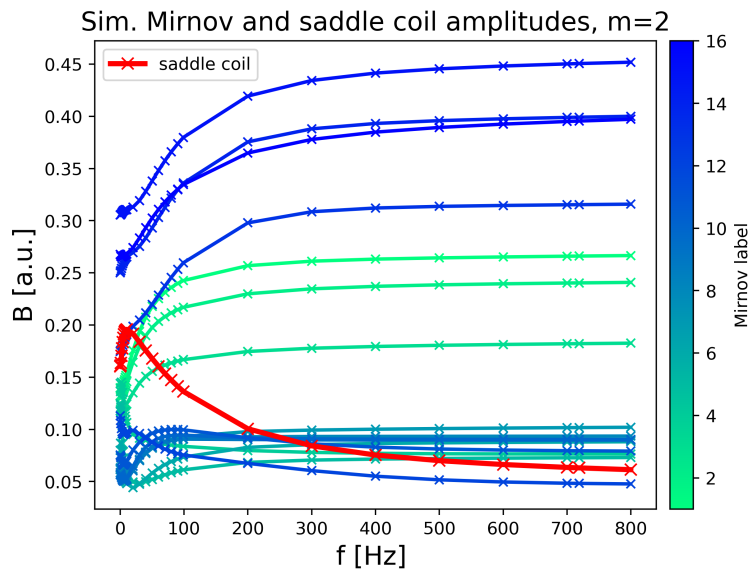


Figure 4.14: Amplitude of simulated saddle (red) and Mirnov coil measurements (cyan to blue) for the geometry of discharge 38706 at $t = 3.0$ s depending on frequency. The Mirnov coil labelling starts with index 1 at the LFS, by definition identical as indicated in figure 4.3.

From figure 4.14 it follows that the ratio between simulated Mirnov and saddle coil amplitudes changes with frequency. This ratio is shown in figure 4.15, where the same virtual Mirnov coils are shown as in figure 4.14. The frequency dependence of $a_{\text{sim,Mirnov}}^{(2,1)}/a_{\text{sim,saddle}}^{(2,1)}$ underlines the necessity of a frequency dependent treatment as done in this work, especially in the low frequency range.

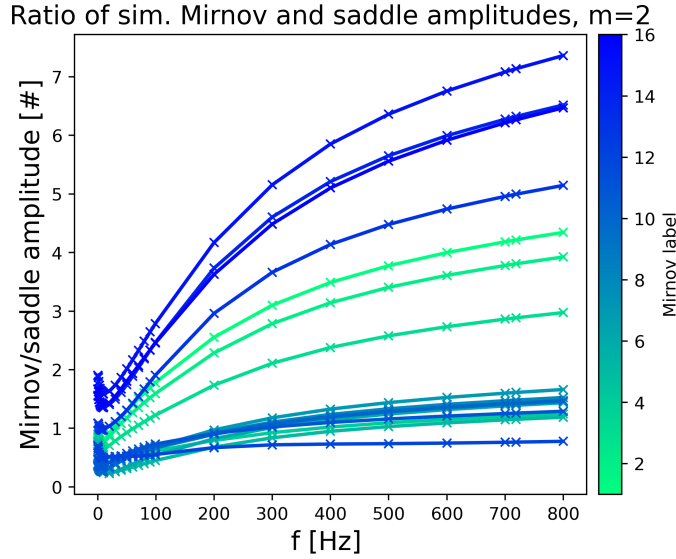


Figure 4.15: Ratio of $\frac{a_{\text{sim,Mirnov}}^{(2,1)}}{a_{\text{sim,saddle}}^{(2,1)}}$ for the geometry of discharge 38706 at $t = 3.0$ s for 16 Mirnov coils. The coil labelling corresponds to the labelling in figure 4.14.

4.4.5 Influence of the position of the resonant surface

In order to get an estimate of the uncertainty of the simulation due to a possible wrong position of the resonant surface from the equilibrium reconstruction, 4 simulations with shifted resonant surfaces are compared. The $q = 2$ surface from the equilibrium reconstruction of discharge 38706 at $t = 3.0$ s is shifted in z - and major radial direction by ± 2 cm respectively, as shown in figure 4.16. The resulting Mirnov amplitudes and phases generated by $\mathbf{j}_{\text{pert}}^{(2,1)}$ rotating at $f = 719$ Hz are shown in figure 4.16.

The angle α between $\tilde{B}_{\text{sim},k}^{(2,1)}$ on the $q = 2$ surface from the equilibrium reconstruction and on the shifted surfaces gives an average of $\alpha = 4.07^\circ$ with a minimum deviation of $\alpha = 3.86^\circ$ (shift of 2 cm in negative major radial direction towards the HFS) and a maximum deviation of $\alpha = 4.17^\circ$ (shift in negative z -direction towards the bottom). Figure 4.16 shows that a shift of the resonant surface in major radial direction has a large effect on the simulated amplitudes on HFS and LFS, while the simulated phase remains almost unchanged. To minimise the effect of an incorrect position of the resonant surface, coils with a similar θ_{coil} should be used, when comparing different coil types, as done in section 4.6.

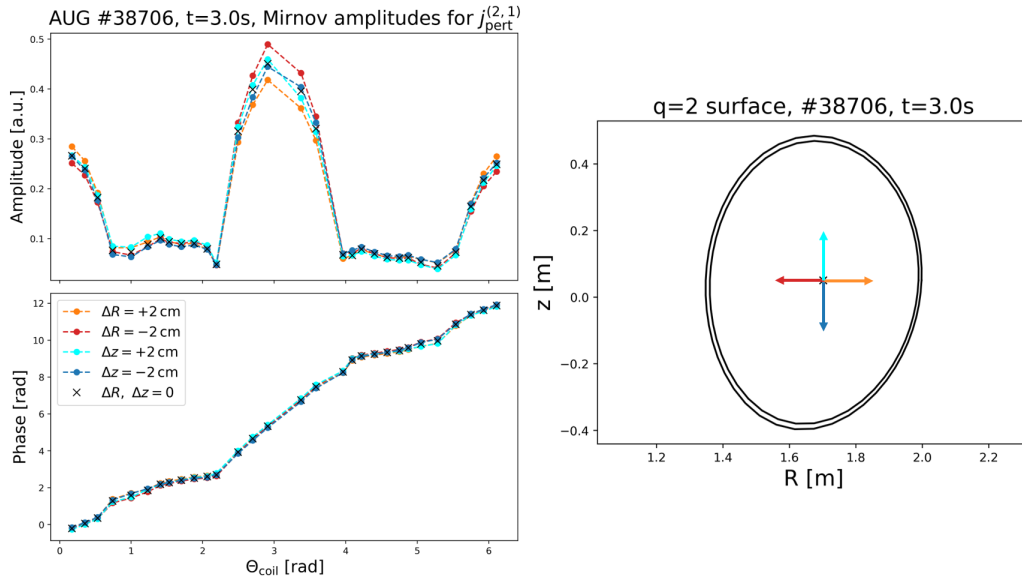


Figure 4.16: Simulated Mirnov measurements, $\tilde{B}_{\text{sim},k}^{(2,1)}$, (left figure) generated by $\tilde{j}_{\text{pert}}^{(2,1)}$ at a $q = 2$ surface which is shifted by $\pm 2\text{ cm}$ in major radial direction (orange, red) and $\pm 2\text{ cm}$ in z -direction (cyan, blue). $\tilde{B}_{\text{sim},k}^{(2,1)}$ for the non-shifted surface are shown as black crosses. The right figure shows the $q = 2$ surface geometry used as the source region for the non-shifted case. The coloured arrows indicate the direction of the shift.

4.5 Determination of mode composition

As seen in figure 4.13, a single helicity perturbation current $\tilde{j}_{\text{pert}}^{(2,1)}$ cannot reproduce the $\tilde{B}_{\text{meas},k}$ for a seemingly pure (2,1) mode measured by the poloidal Mirnov coil array. The stability analysis, shown in section 2.4.2, suggested that multiple poloidal harmonics $\tilde{j}_{\text{pert}}^{(m,n)}$ must be considered for a complete description of the current density for a tearing mode at $\beta > 0$. We will now show experimental evidence that tearing modes are generally composed of different m in our base vector system.

4.5.1 Method and application

Since tearing modes on the $q = 2$ and $q = 3$ surfaces are considered to be the most important $n = 1$ tearing modes in regard to disruptions, and we include sidebands with $\Delta m = \pm 1$, $\tilde{j}_{\text{pert}}^{(m,1)}$ with $m \in \{1, 2, 3, 4\}$ are considered as appropriate base vectors for the perturbation current. Note that the phases of the expected Mirnov measurements of an $m = 3$ sideband of an $m = 2$ tearing mode, which is on the $q = 2$ surface, are almost the same as those of an $m = 3$ poloidal harmonic on the $q = 3$ surface. Apart from the different amplitude, which is due to different distance between current and coils, the expected Mirnov amplitudes differ due to the differences in the $\theta^*(\theta)$ and the different shapes and positions of the resonant surfaces, as shown in figure 4.17, where the virtual Mirnov amplitudes and phases are presented for an $m = 3$ poloidal harmonic on its $q = 3$ surface and on the $q = 2$ surface, resulting in a deviation of $\alpha = 18.5^\circ$. Since there could also be a tearing mode on a surface with $q \neq 2$, each $\tilde{j}_{\text{pert}}^{(m,1)}$ is simulated on the $q = m$ surface, apart

from $\mathbf{j}_{\text{pert}}^{(1,1)}$, which is positioned on $q = 2$ because the equilibrium reconstruction in the plasma core is less reliable and does not always contain a $q = 1$ surface (cf. section 4.4.3).

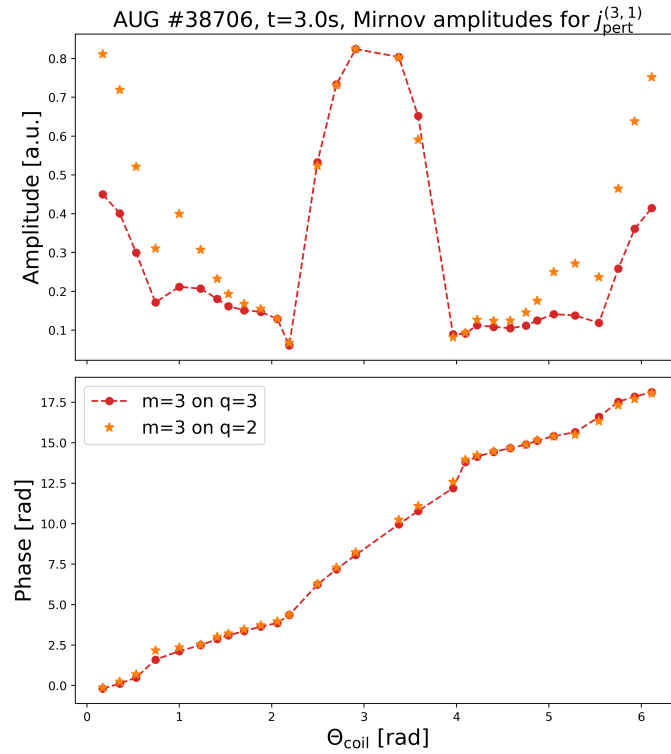


Figure 4.17: Simulated amplitudes and phases of the virtual Mirnov measurements for discharge 38706, at $t = 3.0$ s for poloidal harmonics $\mathbf{j}_{\text{pert}}^{(3,1)}$ on the $q = 3$ (red) and on the $q = 2$ surface (orange). The simulated amplitudes of $\mathbf{j}_{\text{pert}}^{(3,1)}$ on the $q = 3$ surface are multiplied by a factor so that the two maximal simulated amplitudes match.

The expected measurement for all coils k , $\tilde{\mathbf{B}}_{\text{sim},k}^{(m,1)}$, resulting from the model, form a vector space for the coil measurements. Determining the contribution of $m \in \{1, 2, 3, 4\}$ to the observed mode means finding the vector in this vector space that is closest to the measurement vector. This is defined by the minimum of

$$\|\tilde{\mathbf{B}}_{\text{meas}} - \sum_m \tilde{a}^{(m,1)} \tilde{\mathbf{B}}_{\text{sim}}^{(m,1)}\| \quad . \quad (4.36)$$

This linear problem is solved by the pseudoinverse as e.g. described in [22]. Naturally, the number of base modes must be smaller than the number of coils in order to get a unique solution with a deviation α .

As shown in section 4.4.4, an agreement of $\alpha = 26.9^\circ$ between Mirnov measurements and simulations was achieved for the basic model geometry with only wall and PSL for $\mathbf{j}_{\text{pert}}^{(2,1)}$, which was improved to $\alpha = 16.0^\circ$ by implementing the support bridges and the additional conducting structures on the HFS. Using $\mathbf{j}_{\text{pert}}^{(m,1)}$ with $m \in \{1, 2, 3, 4\}$, $\tilde{\mathbf{B}}_{\text{meas}}$ for the same discharge (cf. figure 4.13) is reproduced by the simulated Mirnov results with $\alpha = 8.81^\circ$ as shown in figure 4.18. Especially the measured phase is matched with $\mathbf{j}_{\text{pert}}^{(m,1)}$ and $m \in \{1, 2, 3, 4\}$.

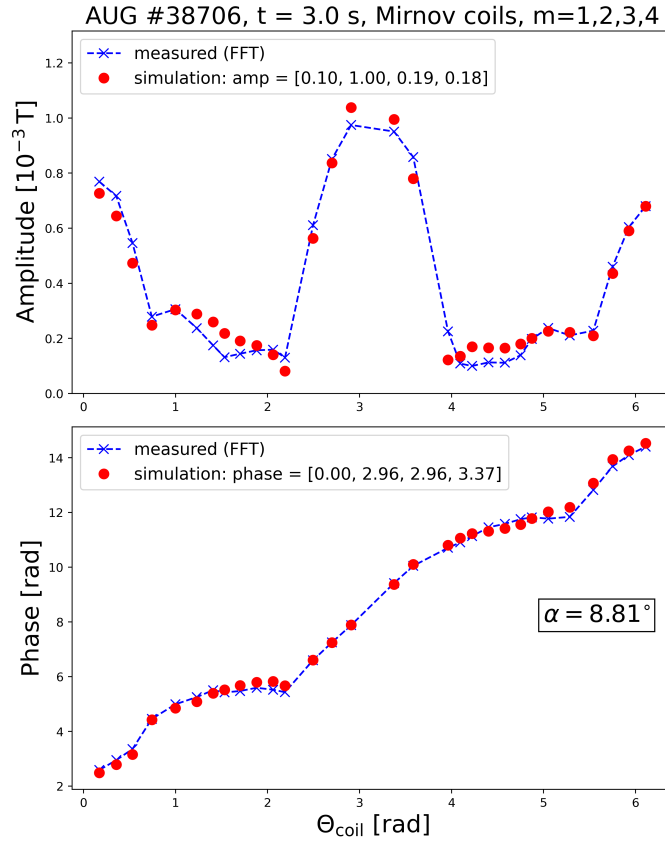


Figure 4.18: Comparison of simulated (red dots) to measured (blue crosses) Mirnov amplitudes and phases for discharge 38706 at $t = 3.0$ s where the tearing mode was rotating with a frequency $f = 719$ Hz. The relative amplitudes and phase relations of the poloidal harmonics of $\tilde{\mathbf{j}}_{\text{pert}}$ are given in the legend. α , as defined in equation 4.25, is given in the lower plot.

As it is common to present the measured amplitudes and phases separately, we introduce normalised deviations of amplitude (ε_A) and phase (ε_φ), even though equation 4.36 is minimised for the complex values. When calculating the minimum of equation 4.36 using the pseudoinverse, small signals, which are considered less reliable, are naturally given less weight. This also motivates the definition of ε_A and ε_φ of all N coils according to the 2-norm:

$$\varepsilon_A = \frac{1}{N} \sqrt{\sum_k \varepsilon_{A,k}^2} \quad \text{and} \quad \varepsilon_\varphi = \frac{1}{N} \sqrt{\sum_k \varepsilon_{\varphi,k}^2} \quad (4.37)$$

with the individual deviations of amplitude and phase for each coil k

$$\varepsilon_{A,k} = \frac{|a_{\text{meas},k} - a_{\text{sim},k}|}{a_{\text{mean}}} \quad \text{and} \quad \varepsilon_{\varphi,k} = \frac{|\varphi_{\text{meas},k} - \varphi_{\text{sim},k}|}{\pi} \quad (4.38)$$

where a_{mean} is the average measured amplitude and $a_{\text{sim},k}$ and $\varphi_{\text{sim},k}$ are the amplitudes and phases of the k th component of $\tilde{\mathbf{B}}_{\text{sim}} = \sum_m \tilde{a}^{(m,1)} \tilde{\mathbf{B}}_{\text{sim}}^{(m,1)}$. The phase difference $\varphi_{\text{meas},k} - \varphi_{\text{sim},k}$ is evaluated to be in the interval $[-\pi, \pi]$. This results in an individual phase deviation $\varepsilon_{\varphi,k}$ between 0 and 1, where 1 corresponds to the maximal phase deviation of $\pm\pi$. Figure 4.19 shows the individual deviations of amplitude and phase for the case shown in figure 4.18, where the individual phase errors are small for all coils and the total deviations are $\varepsilon_A = 0.0241$ and $\varepsilon_\varphi = 0.0099$.

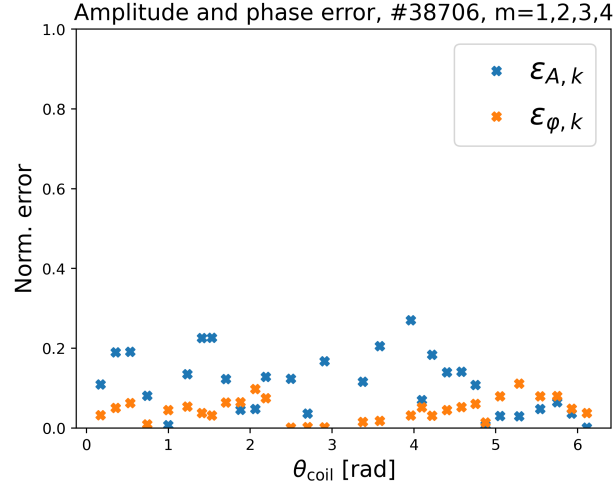


Figure 4.19: Individual deviations $\varepsilon_{A,k}$ (blue) and $\varepsilon_{\varphi,k}$ (orange) depending on the poloidal angle θ_{coil} of the coils k for the case shown in figure 4.18.

4.5.2 Agreement between simulated and measured Mirnov amplitudes and phases over a wide frequency range

The agreement between $\tilde{\mathbf{B}}_{\text{meas}}$ and $\tilde{\mathbf{B}}_{\text{sim}}$ is also tested for other discharges, listed in table 4.2, covering a wide frequency range.²⁶ Figure 4.20 shows the normalised errors, ε_A with a mean value of 0.0307 and ε_φ with a mean of 0.0217, which are comparably low for all discharges. As in the case of discharge 38706 (cf. figures 4.18 and 4.19), in most cases the measured phases can be better reproduced than the amplitudes.

Discharge	t [s]	f [Hz]
40488*	1.53	153
35667	5.17	251
38628	1.84	280
39661	5.70	448
40703	7.10	635
38706	3.00	719
35713	6.26	795
38926	2.00	1400
38761	2.70	1640
41417*	2.24	2400
34008*	3.65	3426
36234	1.80	4050
36171	5.61	4220
35667	1.66	5380
41091	6.05	9383

Table 4.2: Discharges and evaluated times. For the discharges marked with a star, the IDE code [34] was used for the equilibrium reconstruction.

²⁶The signal of coil 'C09-32' was excluded for discharges 35667, 35713, 36234 and 36171 as this coil did not work in these discharges. Coil 'C09-11' was additionally excluded for discharge 35667 for the same reason.

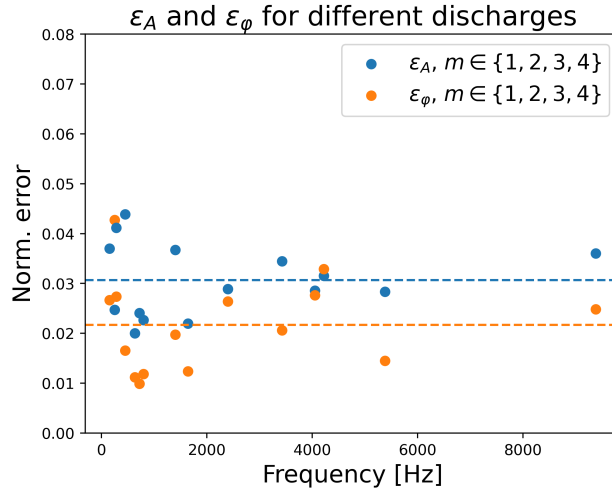


Figure 4.20: Normalised amplitude and phase deviations, ε_A and ε_φ , for different frequencies (cf. discharges listed in table 4.2) for simulations with $m \in \{1, 2, 3, 4\}$. The average values are shown as blue and orange dashed lines.

4.6 Calibration for consistent description of all coil types

In the previous section we showed that the measured amplitudes and phases of the Mirnov coils can be reproduced by the simulation when considering the relevant m components. The next step is to test the agreement of Mirnov coils with the B_r coils for different frequencies, which will be discussed in this section.

We determine the mode composition, i.e. $\tilde{a}^{(m,1)}$ with $m \in \{1, 2, 3, 4\}$, from the Mirnov coils (cf. equation 4.36) for discharges from table 4.2 and apply this to the B_r coils. If the model perfectly described all the details of the experimental setup, the plasma and all coils, and if the chosen m perfectly described the tearing mode, the simulation would perfectly reproduce all measurements. Thus, the complex measured amplitudes $\tilde{B}_{\text{meas},k}$ and the complex simulated amplitudes $\tilde{B}_{\text{sim},k} = \sum_m \tilde{a}^{(m,1)} \tilde{B}_{\text{sim},k}^{(m,1)}$ would always be identical for all coils k , regardless of the coil type. We introduce the complex ratio γ_B as a measure of the agreement between different coil types which compares the relation between $\tilde{B}_{\text{meas},k}$ and $\tilde{B}_{\text{sim},k}$ for coils k , labelled I and II, which can also be of different coil types:

$$\gamma_B = \frac{\frac{\tilde{B}_{\text{meas},\text{I}}(t)}{\tilde{B}_{\text{sim},\text{I}}(f(t))}}{\frac{\tilde{B}_{\text{meas},\text{II}}(t)}{\tilde{B}_{\text{sim},\text{II}}(f(t))}} \quad (4.39)$$

where $f(t)$ is the mode frequency at time t . A perfect representation would always result in $\gamma_B = 1$. Since no perfect model is expected due to approximated shapes of the conducting components (cf. section 4.4.2), γ_B is used to test the agreement, first between Mirnov and Ballooning coils (cf. section 4.6.1) and then between Mirnov and saddle coils. For the latter, there are free parameters in the model, which are determined by minimizing $|\gamma_B - 1|$ as discussed in section 4.6.2.

4.6.1 Correcting Mirnov with Ballooning coils

The Mirnov coils are installed in the welding flange of the AUG vacuum vessel (cf. figure 4.21), whereas in the model the wall is modelled toroidally symmetric,

as the actual flange geometry cannot be represented by toroidally extruded wall elements. It is necessary to check whether this missing detail in the conducting structures requires a correction. For this purpose we compare the Mirnov coils with the Ballooning coils²⁷ for the set of discharges listed in table 4.2. The latter are mounted with a clear distance to the wall and the conducting structures relevant for them are expected to be well captured in the model. The ratio γ_B is calculated as defined in equation 4.39, where coil I corresponds to a Ballooning coil and coil II to a Mirnov coil. We chose the Mirnov coils at similar poloidal angles as the Ballooning coils ('C09-01' and 'C09-32' cf. figure 3.4) to minimise the effect of errors in the resonant surface position (cf. section 4.4.5) and in the determination of $\tilde{a}^{(m,1)}$. For each pair of coils of different type γ_B is calculated and the average complex value is determined.

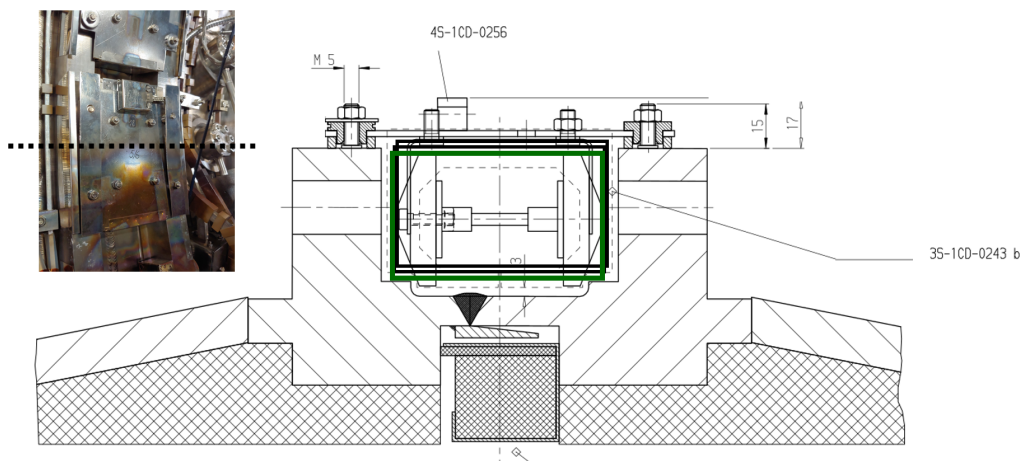


Figure 4.21: Technical drawing from [54], adapted to show the position of a Mirnov coil (black and green rectangles). The drawing plane is indicated by the dotted horizontal line in the inserted picture of the flange where the coils are installed.

The upper plot of figure 4.22 shows the absolute values of γ_B for different discharges and mode frequencies, revealing a frequency dependent factor between Ballooning and Mirnov coils. Towards zero frequency, where shielding currents vanish, $|\gamma_B|$ approaches 1. This indicates that mirror currents, presumably radial currents in the flange contour, lead to a reduction of the measured Mirnov coil amplitude for frequencies $f > 0$. To achieve agreement between Ballooning and Mirnov coils for frequencies $10\text{Hz} < f < 10\text{kHz}$, the simulated Mirnov amplitudes are corrected with the function (cf. figure 4.22)

$$h(f) = \left(-\frac{1}{f^{1/7}} + 1.7 \right)^{-1}. \quad (4.40)$$

The phase of γ_B is close to zero (cf. lower plot in figure 4.22), which indicates that model and measurement agree in terms of the relative phases between Mirnov and Ballooning coils. Thus, only the amplitude of the Mirnov coils is corrected. The simulations to find this correction are performed with an effective conductivity $\sigma_{\text{vessel,eff}} = 2.0 \cdot 10^5 \frac{1}{\Omega\text{m}}$ found by the scan described in the following section 4.6.2. Finding the Mirnov coil amplitude correction function was done iteratively with updated values of σ_{vessel} (determined by the scan described in section 4.6.2).

²⁷The Ballooning coil 'B31-40' has been excluded here as the position of the coil has changed between campaigns.

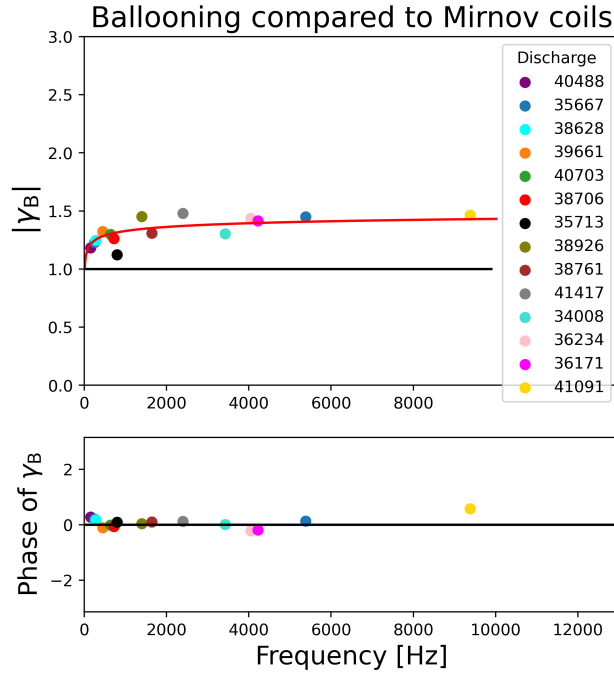


Figure 4.22: Absolute value (upper plot) and phase (lower plot) of γ_B calculated for different discharges as defined in equation 4.39, where coil I corresponds to the Ballooning coils and coil II to the Mirnov coils on the LFS. The red line in the upper plot is the inverse of $h(f)$ as defined in equation 4.40.

4.6.2 Optimization of free parameters: scan of R_{saddle} and σ_{vessel}

The model description requires some simplifications due to the toroidally extruded elements and in order to ensure an appropriate meshing of the wall. On the other side, also the AUG reality is not precisely known. This introduces free parameters for the model that have to be fixed before it can be used.

First, the vacuum vessel cannot be implemented with the exact geometry and resistivities of all materials present and electrical connections are not exactly known. This requires to introduce an effective conductivity of the wall, $\sigma_{\text{vessel,eff}}$. The second free parameter is the effective position of the saddle coil, $R_{\text{saddle,eff}}$, as the distance between the coil winding and the vacuum vessel, $\Delta R_{\text{saddle,wall}}$, varies in toroidal direction in AUG which is too complex to replicate in this framework (cf. figure 4.23). These effective parameters have to ensure the best possible agreement between Mirnov and saddle coils. To determine them, γ_B (cf. equation 4.39) is calculated for a matrix of $(\sigma_{\text{vessel,eff}}, R_{\text{saddle,eff}})$ pairs, with $1.0 \cdot 10^5 \frac{1}{\Omega\text{m}} < \sigma_{\text{vessel,eff}} < 5.0 \cdot 10^5 \frac{1}{\Omega\text{m}}$ and $0.96 \text{ m} < R_{\text{saddle,eff}} < 1.01 \text{ m}$. Here, coil I corresponds to the Mirnov coils 'C09-16' and 'C09-17' behind the saddle coil (cf. figure 3.4) and coil II to the saddle coil.²⁸ In order to find the best $(\sigma_{\text{vessel,eff}}, R_{\text{saddle,eff}})$ pair for all resonant surface geometries, mode compositions $(\tilde{a}^{(m,1)})$ and frequencies, γ_B is evaluated for time periods of different discharges with a strong $n = 1$ mode (cf. table 4.3), covering a wide frequency range.²⁹ For each discharge, poloidal mode number, and σ_{vessel} , a frequency scan is

²⁸In the calculation of γ_B , the measured mean saddle amplitude is taken and $\tilde{a}^{(m,1)}$ are determined from the Mirnov coils with an effective conductivity of the wall, $\sigma_{\text{vessel,eff}} = 2.0 \cdot 10^5 \frac{1}{\Omega\text{m}}$.

²⁹The equilibrium reconstruction for each discharge is evaluated at time points with small equilibrium changes, so that the same geometry is used for an entire time period.

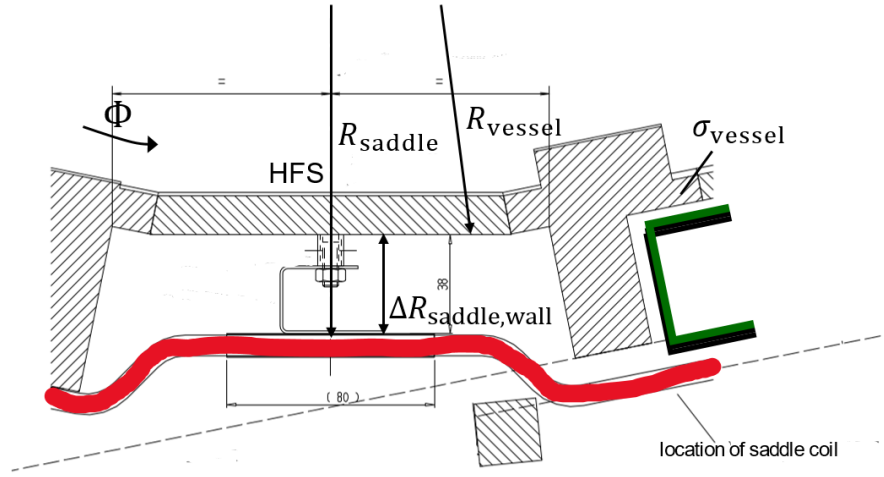


Figure 4.23: Excerpt from a technical drawing of a horizontal cut of the vacuum vessel on the HFS, where the location of a part of the saddle coil (red) is indicated. The distance to the conducting vessel varies with toroidal angle, Φ . In this figure, also a part of the Mirnov coil (black and green) is shown (adapted from [54]).

performed to calculate γ_B for the corresponding time points, i.e. frequencies.

Discharge	time period	frequency range
36234	1.705 - 1.895 s	3213 - 4893 Hz
38706	2.807 - 3.095 s	594 - 3503 Hz
38761	2.605 - 2.854 s	9289 - 1647 Hz
36171	5.605 - 5.681 s	925 - 4219 Hz
38926	1.602 - 2.256 s	904 - 2521 Hz
35667	1.369 - 1.997 s	556 - 5378 Hz
35667	5.013 - 5.289 s	251 - 406 Hz
34008	3.646 - 3.654 s	1877 - 3499 Hz

Table 4.3: Time periods used for the scan of R_{saddle} and σ_{vessel} .

Only the absolute value of γ_B is used and the phase is checked for the best pair of $\sigma_{\text{vessel,eff}}$ and $R_{\text{saddle,eff}}$. The requirement that $|\gamma_B| = 1$ for all frequencies can be divided into two conditions for γ_B , namely

$$\frac{\partial |\gamma_B|}{\partial f} = 0 \text{ and } \overline{\gamma_B} = 1 \quad (4.41)$$

with $\overline{\gamma_B}$ the average value of $|\gamma_B|$. Both conditions must be approximated simultaneously, which is described by the combined condition using the geometrical mean value:

$$\sqrt{|\overline{\gamma_B} - 1| \cdot d} = 0 \quad (4.42)$$

with d the absolute deviation of $\frac{\partial |\gamma_B|}{\partial f}$ from zero. To compute d , first a polynomial fit of degree 4 is determined for each $(\sigma_{\text{vessel,eff}}, R_{\text{saddle,eff}})$ pair for all discharges simultaneously to obtain $|\gamma_B|$ as a function of frequency. From this, the derivative $\frac{\partial |\gamma_B|}{\partial f}$ is calculated. The summed absolute deviation of $\frac{\partial |\gamma_B|}{\partial f}$ from zero is taken to also account for frequency dependent $|\gamma_B|$ with a mean value close to 1.

Figure 4.24 shows the frequency dependence of $|\gamma_B|$ for a pair of $(\sigma_{\text{vessel,eff}}, R_{\text{saddle,eff}})$, where the requirements are not fulfilled (figure a.1)) and the corresponding determi-

nation of d and $|\gamma_B| - 1$ in figure a.2). The values of the combined condition of equation 4.42 for different $(\sigma_{\text{vessel,eff}}, R_{\text{saddle,eff}})$, including the example in the top row, are shown as coloured dots in figure 4.24b). The minimum, i.e. the best pair of $(\sigma_{\text{vessel,eff}}, R_{\text{saddle,eff}})$, is found for $R_{\text{saddle}} = 0.98$ m, corresponding to $\Delta R_{\text{saddle,wall}} = 2.7$ cm, and $\sigma_{\text{vessel}} = 2.0 \cdot 10^5 \frac{1}{\Omega\text{m}}$. The frequency dependence of $|\gamma_B|$ for the best $(\sigma_{\text{vessel,eff}}, R_{\text{saddle,eff}})$ is shown in figure 4.24c). The analysis is done for discharges with primarily a dominant $m = 2$ tearing mode, but also the case with a dominant $m = 3$ mode (discharge 34008) obeys condition 4.42 for the correct $(\sigma_{\text{vessel,eff}}, R_{\text{saddle,eff}})$ with sufficient accuracy.

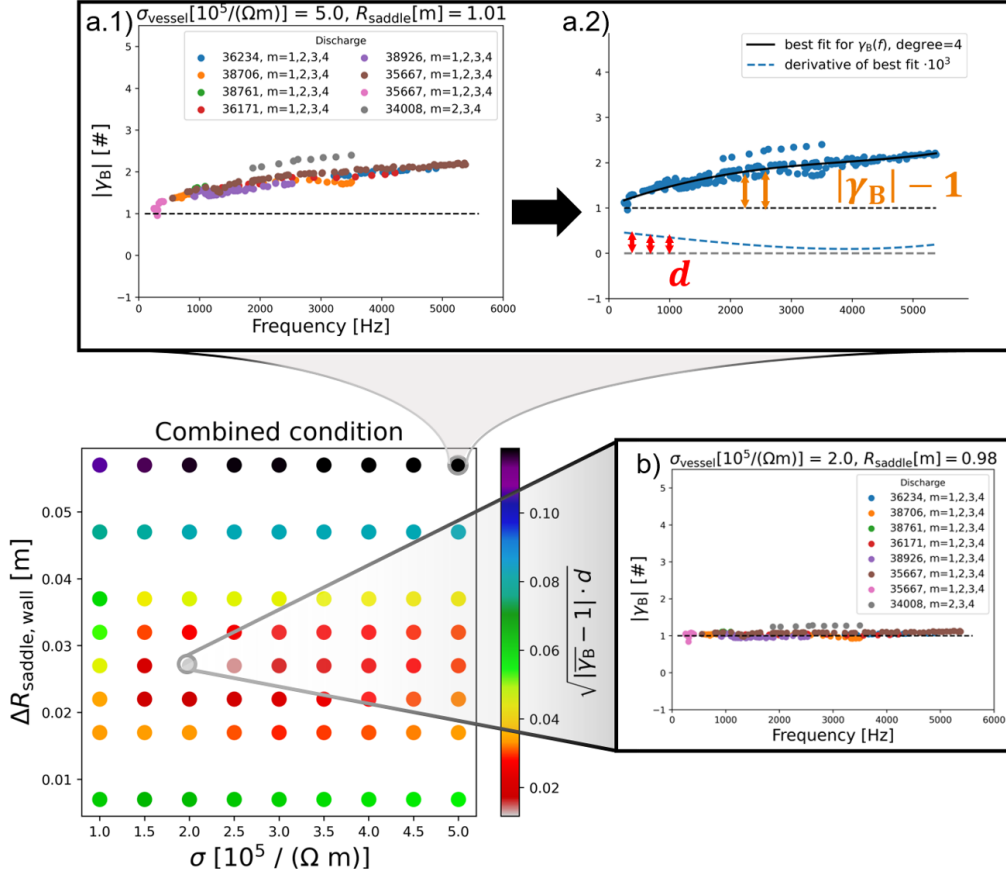


Figure 4.24: An example with a wrong effective conductivity $\sigma_{\text{vessel}} = 5 \cdot 10^5 \frac{1}{\Omega\text{m}}$ and a wrong saddle position $R_{\text{saddle}} = 1.01$ m is shown in the upper row where the calculation of $|d|$ and $|\gamma_B| - 1$ is demonstrated on the right. The lower left plot shows the requirements for γ_B , as defined in equation 4.42, calculated for different pairs of $(\sigma_{\text{vessel,eff}}, R_{\text{saddle,eff}})$. The effective distance between the saddle coil and the vessel, $\Delta R_{\text{saddle,wall}}$, is $R_{\text{saddle}} - R_{\text{wall}}$ with $R_{\text{wall}} = 0.953$ m at $z = 0$ on the HFS, according to table 4.1. The minimum values, i.e. the best values, are shown in grey, resulting in a best pair of $(\sigma_{\text{vessel,eff}}, R_{\text{saddle,eff}})$ (lower right plot). In most cases, there is a dominant $m = 2$ tearing mode (different colors for different discharges in the upper left and lower right plot), whereas one discharge (34008) contains a dominant $m = 3$ mode at the selected frequencies.

The angle of the complex ratio γ_B is evaluated for the discharge with the largest frequency coverage and the result for the best $(\sigma_{\text{vessel,eff}}, R_{\text{saddle,eff}})$ is shown in figure 4.25. The phase of γ_B is frequency independent but only approximately zero. A constant phase offset of -0.04π is observed between the Mirnov and saddle coils, which might be due to a toroidal shift between the nominal and actual positions of

the saddle coils in AUG. This small phase difference is neglected and $R_{\text{saddle}} = 0.98$ m and $\sigma_{\text{vessel}} = 2.0 \cdot 10^5 \frac{1}{\Omega\text{m}}$ are chosen as effective parameters for the simulation. Note that this effective conductivity is valid for a vacuum vessel thickness of $d_w = 6$ cm as defined in section 4.4.2. For the flange thickness of the vacuum vessel $d_w = 15$ mm,³⁰ this corresponds to an effective $\sigma_{\text{vessel}} = 8.0 \cdot 10^5 \frac{1}{\Omega\text{m}}$, which is – as expected – below the documented value of the primary wall material [83] $\sigma_{\text{vessel,theo}} = 1.4 \cdot 10^6 \frac{1}{\Omega\text{m}}$.

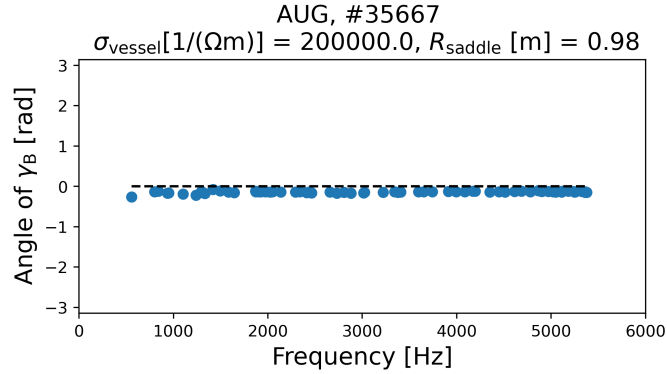


Figure 4.25: Phase of the complex ratio γ_B for $R_{\text{saddle}} = 0.98$ m and $\sigma_{\text{vessel}} = 2.0 \cdot 10^5 \frac{1}{\Omega\text{m}}$ calculated for discharge 35667.

4.7 Possible extensions to the model

As will be shown in section 6.3, the simulated complex measurements $\tilde{B}_{\text{sim},k}$ with complex amplitudes $\tilde{a}^{(m,1)}$ determined from the Mirnov coils are also in agreement with the measured amplitudes and phases of the saddle and Ballooning coils, which confirms an overall consistent description of the different coil types. However, the model still uses a simplified geometry that could be refined in the future. In AUG the B-coils are mounted on the PSL in a steel housing which is not implemented in the model. This is not relevant for the analysis of locked modes, but in the slowly rotating phase, if usable B-coil data are available (cf. section 5.2), the effect of the steel housing has to be considered. As described in section 4.4.2, the exact shape of the support bridges is not implemented, which might be relevant when considering other Ballooning coils at the LFS with $\theta_{\text{coil}} \neq 0$. Moreover, instead of correcting the amplitude of the Mirnov coils as described in section 4.6.1, the flange structure could be implemented in its exact geometry, which might require supplementary calculations in a geometry without toroidally extruded sections.

In addition, at very low frequencies, i.e. at a few Hz, an effect occurs that cannot be reproduced by the simulation. Figure 4.26 shows the simulated and measured Mirnov amplitudes and phases for discharge 40648 where a tearing mode was rotating at 2.7 Hz (figure b)). The measurements cannot be reproduced ($\alpha = 40.0^\circ$) due to the high amplitudes of the Mirnov coils behind the PSL, which are marked in yellow in figures a) and b)). The reason for the deviation between the simulated and measured results for the Mirnov coils behind the PSL at these low frequencies are probably external control coils (similar to the poloidal field coils in figure 1.2), which react to a presumed plasma motion in the vertical direction. In AUG there are two control coils ('CoIu' and 'CoIo') approximately at the poloidal position of the upper and lower PSL, which can cause an amplification of the measured Mirnov amplitudes and a

³⁰Here we assume that the skin depth is approximately equal to the wall thickness.

phase distortion at these poloidal positions. Figure 4.27 shows the time traces of the currents in the control coils and the magnetic field measured by two affected Mirnov coils, which are clearly correlated. The currents in these control coils could also be included in the model or the affected Mirnov coils behind the PSL are ignored for the determination of the poloidal mode composition in these cases.

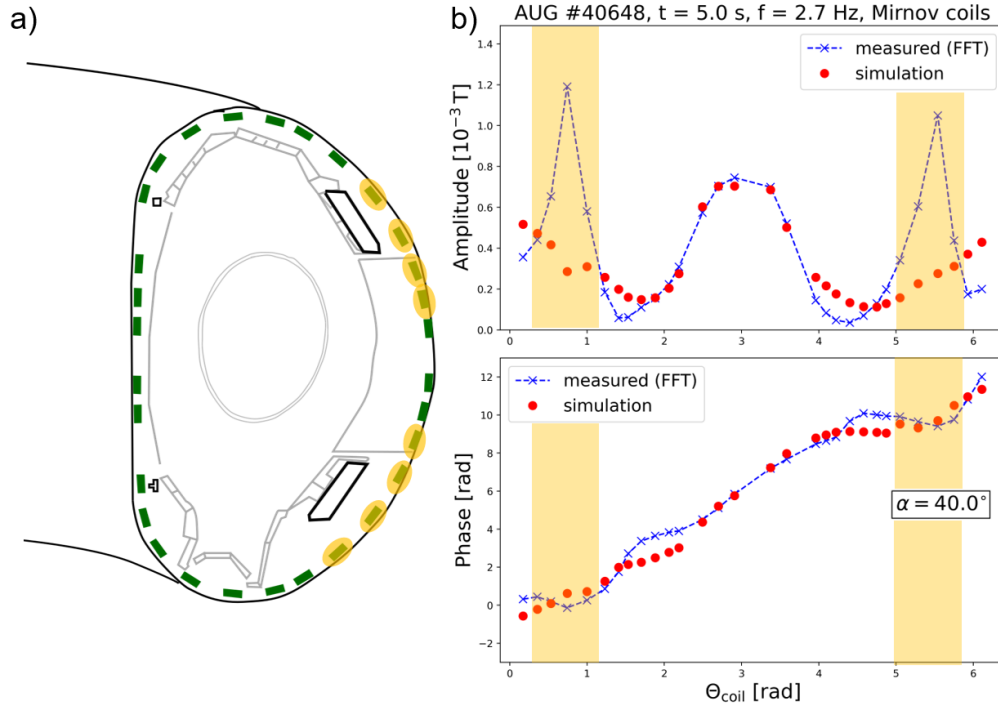


Figure 4.26: Poloidal cross section of the vessel, including in-vessel components and the geometry of a magnetic flux surface, with the Mirnov coils shown as green boxes (figure a). The affected Mirnov coils are marked in yellow. Figure b) shows the simulated and measured amplitudes and phases of a slowly rotating mode depending on the poloidal angle of the coil position θ_{coil} . The areas of θ_{coil} where the Mirnov coil measurements are expected to be affected are marked in yellow.

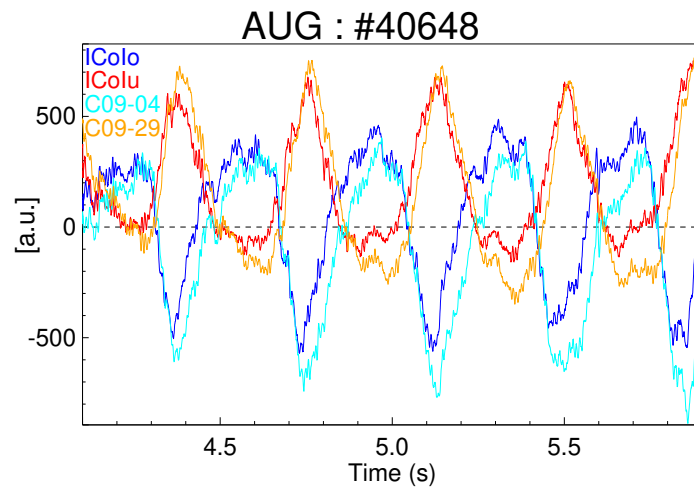


Figure 4.27: Time traces of the currents in the control coils 'CoIu' (red) and 'CoIo' (blue) and of the magnetic field measured by the Mirnov coils 'C09-04' (cyan) and 'C09-29' (orange).

5 Mode composition with radial field coils

Assuming usable B-coil data – at least in the case of locked modes, where shielding currents no longer play a role – radial field measurements at 4 different poloidal positions with one toroidal array each are available in AUG. These radial field coils have to be sufficient to determine the poloidal mode composition for locked modes, since the poloidal perturbation field of the mode can no longer be distinguished from the equilibrium magnetic field with enough accuracy, and thus the Mirnov measurements cannot be used for locked modes. The model developed in this work allows to investigate whether these radial field measurements are theoretically sufficient to distinguish the different poloidal mode numbers (cf. section 5.1). The use of the model to determine the poloidal mode composition for locked modes is outlined in section 5.2.

5.1 Theoretical distinguishability

The poloidal harmonics defined according to equation 4.21 form a vector space in which they are orthogonal as the product

$$(\mathbf{j}_{\text{pert}}^{(m,n)}, \mathbf{j}_{\text{pert}}^{(m',n')})_{\Omega} \sim \int_0^{2\pi} \int_0^{2\pi} e^{i(m\theta^* - n\phi)} \cdot e^{i(m'\theta^* - n'\phi)} d\theta^* d\phi = \delta_{mm'} \delta_{nn'} \quad . \quad (5.1)$$

The measurements also form a vector space, but the measurement vector of a single harmonic $\mathbf{j}_{\text{pert}}^{(m,n)}$ is not necessarily orthogonal to the measurements of the harmonic $\mathbf{j}_{\text{pert}}^{(m',n')}$ with $m \neq m'$, $n \neq n'$. Orthogonal measurement vectors are not necessary, but the measurement vectors must be sufficiently distinguishable to allow the mode composition to be inferred. To test the 'degree' of linear independence, we use the angle α as defined in equation 4.25.

The angle α between two simulated complex measurement arrays $\tilde{\mathbf{B}}_{\text{sim}}^{(m,1)}$ for $m \in \{1, 2, 3, 4\}$ is calculated separately for the Mirnov and the radial field coils for the discharges from table 4.2 to cover different resonant surface geometries and frequencies. Since only the simulated measurements are used in this analysis, the angle α gives an estimate of how well the two poloidal harmonics can theoretically be distinguished with the respective passive coils, independent of the uncertainties in the measured data and their reproducibility with the model. A value of $\alpha = 90^\circ$ would indicate perfect distinguishability. Since a value of $\alpha < 10^\circ$ corresponds to a very good agreement between measurement and simulation for the Mirnov coils (cf. e.g. figure 4.18), $\alpha = 10^\circ$ is used here as the limit for (non-)distinguishability: Values below $\alpha < 10^\circ$ indicate that the measurements of these poloidal harmonics are barely distinguishable, considering uncertainties in the measurements, in the model, and in the position of the resonant surface. For the poloidal array of 30 Mirnov coils, we have assumed that the poloidal harmonics are sufficiently distinguishable, as will be also shown below. For the radial field coils at only 4 poloidal positions, this is more critical and needs to be validated.

Figure 5.1 shows α between $\tilde{\mathbf{B}}_{\text{sim}}^{(1,1)}$ and $\tilde{\mathbf{B}}_{\text{sim}}^{(2,1)}$ in figure a), between $\tilde{\mathbf{B}}_{\text{sim}}^{(2,1)}$ and $\tilde{\mathbf{B}}_{\text{sim}}^{(3,1)}$ in figure b), between $\tilde{\mathbf{B}}_{\text{sim}}^{(1,1)}$ and $\tilde{\mathbf{B}}_{\text{sim}}^{(3,1)}$ in figure c), and between $\tilde{\mathbf{B}}_{\text{sim}}^{(2,1)}$ and $\tilde{\mathbf{B}}_{\text{sim}}^{(4,1)}$

in figure d) depending on the frequencies of the evaluated times (cf. table 4.2). The angles α between the simulated Mirnov coil measurements (full blue squares) are well above the line indicating $\alpha = 10^\circ$ (black dashed line) in all cases, as expected. For comparison with the radial field measurements, α is also calculated between the simulation arrays of only 4 simulated Mirnov measurements ('C09-01', 'C09-05', 'C09-17', 'C09-29'; open blue squares), which are at similar poloidal positions as the radial field coils. Although coils 'C09-05' and 'C09-29' are affected by the PSL, they are still used for this comparison as their poloidal position is similar to that of the B-coils. The value of α becomes smaller for the case with only 4 Mirnov coils, especially when comparing $\tilde{\mathbf{B}}_{\text{sim}}^{(1,1)}$ and $\tilde{\mathbf{B}}_{\text{sim}}^{(3,1)}$ (figure c)) and $\tilde{\mathbf{B}}_{\text{sim}}^{(2,1)}$ and $\tilde{\mathbf{B}}_{\text{sim}}^{(4,1)}$ (figure d)), indicating that the $m = 2$ and $m = 4$ poloidal harmonics are hardly distinguishable by magnetic measurements at these 4 poloidal positions. Indeed, α between $\tilde{\mathbf{B}}_{\text{sim}}^{(2,1)}$ and $\tilde{\mathbf{B}}_{\text{sim}}^{(4,1)}$ (figure d)) for the simulated radial field coils 'B31-01', 'Bu1', 'SATew' and 'B11' (full orange circles) is also very low for all frequencies. In the case of figure c), the values of α for the radial field coils are not very high either. Figures a) and b) show that α increases for lower frequencies for the radial field coils, indicating that the damping due to mirror currents in the conducting structures leads to more similar measurements, which would not be a problem in the locked case. However, as the calculation of α weights a larger amplitude more than a smaller one, a normalisation could be introduced if all signals are considered equally reliable, taking into account that for the radial field coils we additionally have different coil types. A weighting factor would improve the distinguishability, as can be seen in figures a) to d), where the largest simulated amplitude, i.e. the amplitude of the Ballooning coil 'B31-01', is weighted by a factor of 0.25 (open orange circles), which is only a rough estimate to demonstrate the effect. Using this weighting before calculating α increases the value of α for the radial field coils. A weighting factor might also be useful for calculating the poloidal mode composition with the radial field coils using the pseudoinverse.

Although it will probably be difficult to distinguish the $m = 2$ from the $m = 4$ poloidal harmonic with the radial field coils, the $m = 2$ harmonic can be distinguished – in particular for low frequencies – from the $m = 3$ poloidal harmonic, which are expected to be the most important modes. As will be shown in section 6.2, the $m = 1$ poloidal harmonic is not relevant for determining the phase relation between an $m = 2$ and an $m = 3$ tearing mode, and thus the distinctiveness between the $m = 2$ and $m = 3$ components should be sufficient.

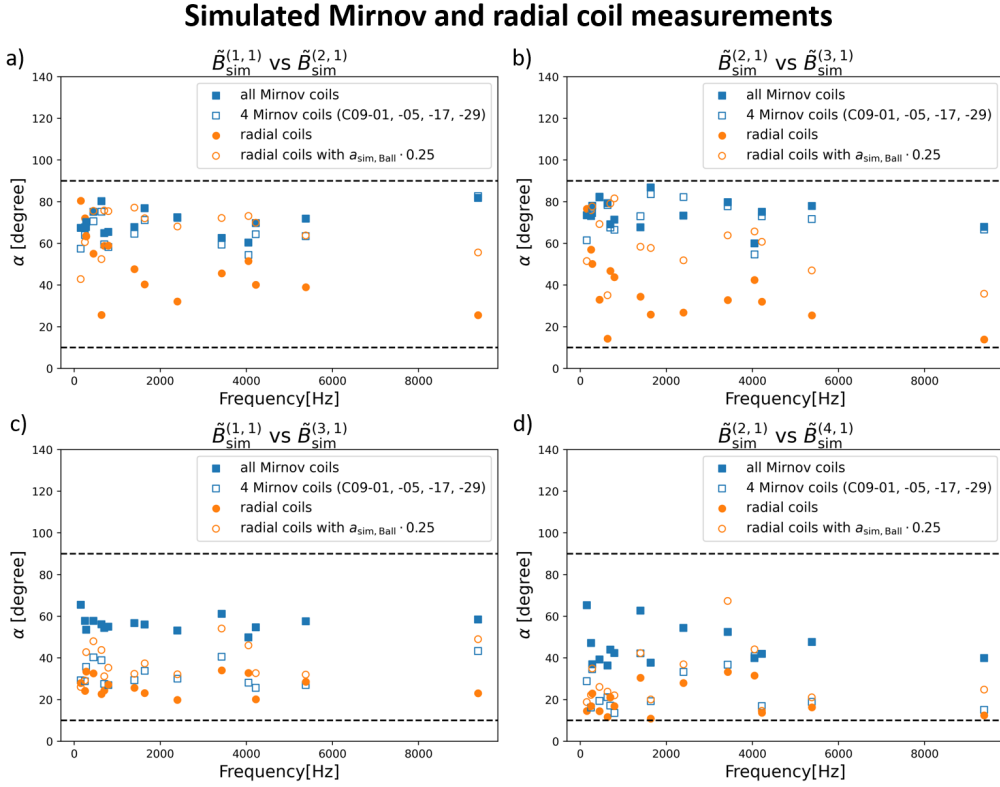


Figure 5.1: α between 2 simulations $\tilde{B}_{\text{sim}}^{(m_1,1)}$ and $\tilde{B}_{\text{sim}}^{(m_2,1)}$ with $m_1 = 1$ and $m_2 = 2$ in figure a), with $m_1 = 2$ and $m_2 = 3$ in figure b), with $m_1 = 1$ and $m_2 = 3$ in figure c), and with $m_1 = 2$ and $m_2 = 4$ in figure d), calculated for the cases listed in table 4.2 and sorted by frequency. α is calculated separately for the Mirnov coils (full blue squares), for only 4 Mirnov coils (open blue squares), for the radial field coils 'B31-01', 'Bu1', 'SATew' and 'B11' (full orange circles) and for these radial field coils but with a weighting factor of 0.25 of the simulated amplitude of the Ballooning coil 'B31-01', $a_{\text{sim,Ball}}$. The values $\alpha = 10^\circ$ and $\alpha = 90^\circ$ are marked with dashed black lines.

5.2 Extension for locked modes

The model is capable of calculating the electromagnetic problem with non-conducting structures, corresponding to the case where the tearing mode is locked with respect to the laboratory frame and hence the vacuum vessel. In the case of non-conducting structures, the mode frequency is irrelevant, allowing the simulation in the frequency domain at any frequency.

A method for determining the mode composition in the locked phase is derived in [53]. While for rotating modes the measured amplitude, $a_{\text{meas},k}$, and phase, $\varphi_{\text{meas},k}$, can be determined from a single coil k at $\theta_{\text{coil},k}$ via FFT, for locked modes, $a_{\text{meas},k}$ and $\varphi_{\text{meas},k}$ must first be determined from a toroidal array of coils at $\theta_{\text{coil},k}$. Assuming a toroidal array of coils k at $\theta_{\text{coil},k}$ with the radial position $r_{\text{coil},k}$, equation 4.36 evaluated at the same toroidal coil position can also be used for locked modes. If, as with the Ballooning coils, there is a toroidal array with different $r_{\text{coil},k}$ (and slightly different tilt angles), a correction for the differences has to be made before using the algorithm of [53] to determine $a_{\text{meas},k}$ and $\varphi_{\text{meas},k}$ for locked modes.

Another method of obtaining the mode composition of locked modes is to directly

compare the real part of the simulation with the measurements. Finding the minimum of the equation 4.36 corresponds to the best solution of

$$\tilde{\mathbf{B}}_{\text{sim}} \tilde{\mathbf{a}} = \tilde{\mathbf{B}}_{\text{meas}} \quad (5.2)$$

where $\tilde{\mathbf{B}}_{\text{sim}}$ is the simulation matrix containing $\tilde{\mathbf{B}}_{\text{sim}}^{(m,1)}$ as columns and $\tilde{\mathbf{a}}$ is the m dimensional vector of $\tilde{a}^{(m,1)}$. This equation must also be satisfied for the real part:

$$\text{Re} \left(\tilde{\mathbf{B}}_{\text{sim}} \tilde{\mathbf{a}} \right) = \text{Re} \left(\tilde{\mathbf{B}}_{\text{meas}} \right) \quad , \quad (5.3)$$

which is the same as

$$\text{Re} \left(\left(\tilde{\mathbf{B}}_{\text{sim,Re}} + i \tilde{\mathbf{B}}_{\text{sim,Im}} \right) \left(\tilde{\mathbf{a}}_{\text{Re}} + i \tilde{\mathbf{a}}_{\text{Im}} \right) \right) = \tilde{\mathbf{B}}_{\text{meas,Re}} \quad , \quad (5.4)$$

where the subscripts Re and Im denote the real and imaginary parts, respectively. Thus, equation 5.4 becomes

$$\tilde{\mathbf{B}}_{\text{sim,Re}} \tilde{\mathbf{a}}_{\text{Re}} - \tilde{\mathbf{B}}_{\text{sim,Im}} \tilde{\mathbf{a}}_{\text{Im}} = \tilde{\mathbf{B}}_{\text{meas,Re}} \quad , \quad (5.5)$$

which can be written in matrix notation:

$$\left(\tilde{\mathbf{B}}_{\text{sim,Re}} \quad - \tilde{\mathbf{B}}_{\text{sim,Im}} \right) \begin{pmatrix} \tilde{\mathbf{a}}_{\text{Re}} \\ \tilde{\mathbf{a}}_{\text{Im}} \end{pmatrix} = \tilde{\mathbf{B}}_{\text{meas,Re}} \quad (5.6)$$

and solved by the pseudoinverse. The amplitudes $a^{(m,1)}$ and phases $\varphi^{(m,1)}$ can then be determined from $\tilde{\mathbf{a}}_{\text{Re}}$ and $\tilde{\mathbf{a}}_{\text{Im}}$.

In order to test the determination of $\tilde{\mathbf{a}}$ by solving equation 5.6, synthetic data with specified amplitudes and phases are used instead of measured data and must be reproduced. As explained earlier, locked modes require toroidally distributed passive radial field coils and hence the real part of all toroidally distributed radial field coils, i.e. the vector $\tilde{\mathbf{B}}_{\text{meas,Re}}$ consists here of 25 entries (7 Ballooning coils, 2 saddle coil signals and 16 B-coils). The simulated amplitudes and phases are calculated directly for all toroidally distributed Ballooning coils, the saddle coil signal corresponding to 'SATew' and the B-coil signals 'B11', 'Bu1', 'B18', 'Bu8' (cf. section 4.4.3). The remaining virtual B-coil measurements have to be calculated – assuming $n = 1$ modes – by adding $-\frac{\pi}{4}l \cdot n$, where $l \in \{1, \dots, 6\}$, to the phase of 'B11' and 'Bu1'. Similarly, by adding $\frac{\pi}{2}n$ to the phase of 'SATew', the virtual measurement of 'SATns' is derived. Figure 5.2 shows that the amplitudes $a^{(1,1)} = 1$, $a^{(2,1)} = 2$, $a^{(3,1)} = 3$ and the phases $\varphi^{(1,1)} = -1$, $\varphi^{(2,1)} = 3$, $\varphi^{(3,1)} = 2$ of the synthetic data can be determined from the radial field coils using equation 5.6, so that the fitted data matches the synthetic data. The coil index in figure 5.2 describes the position in the vector $\tilde{\mathbf{B}}_{\text{meas,Re}}$.

As shown in section 5.1, a weighting factor can improve the distinguishability of two simulated measurement vectors of different poloidal harmonics if the individual simulated coil amplitudes are of different magnitude. Here, the number of coils of the same type is also different. Thus, an additional weighting by the number of coils of the same type could be considered.

For slowly rotating $n = 1$ tearing modes, where the mode is visible in the difference signal of two B-coils toroidally separated by an angle of π , the amplitudes determined from FFT of all difference signals of two opposing upper (and lower) B-coils should be equal as long as the mode rotates. However, this is not the case as shown in figure 5.3 for a very slowly rotating mode ($f = 2.7$ Hz), where the amplitudes of the difference signals differ significantly. The steel casing surrounding the B-coils, not implemented

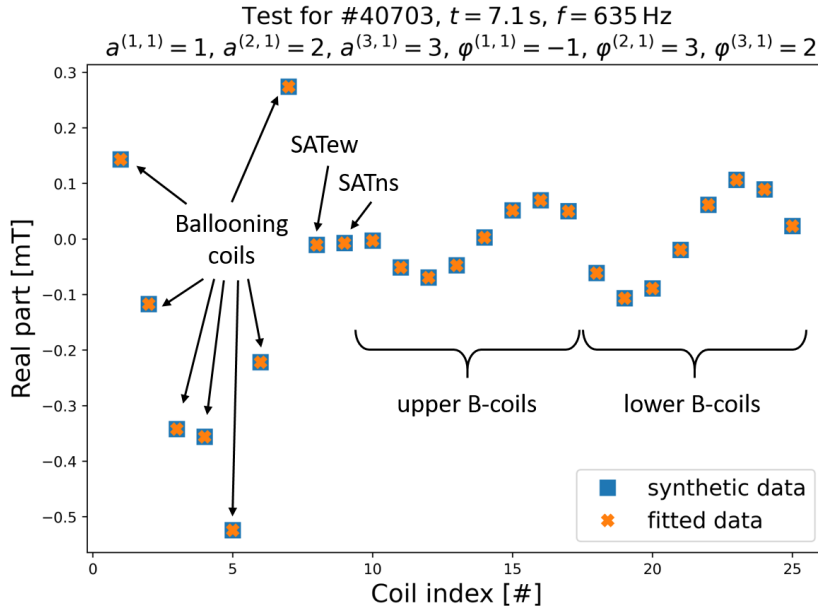


Figure 5.2: Test of equation 5.6 using synthetic data of radial field coils for discharge 40703 at $t = 7.1$ s and $f = 635$ Hz with given amplitudes $a^{(1,1)} = 1$, $a^{(2,1)} = 2$, $a^{(3,1)} = 3$ and phases $\varphi^{(1,1)} = -1$, $\varphi^{(2,1)} = 3$, $\varphi^{(3,1)} = 2$ (blue squares) which can be reproduced by the fitted data (orange crosses), where the poloidal mode composition $\tilde{\mathbf{a}}$ is determined from the radial field coils using equation 5.6. The names of the coil signals to which the coil indices (on the x-axis) belong are given in the figure.

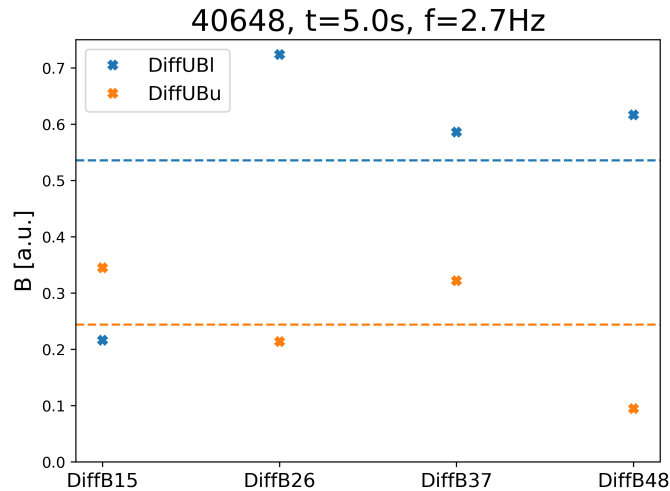


Figure 5.3: Amplitudes of the difference signals 'DiffUBl' of the lower B-coils (blue) and 'DiffUBu' of the upper B-coils (orange) for the B-coils toroidally separated by an angle of π for discharge 40648 at about $t = 5.0$ s, where the mode was rotating at $f = 2.7$ Hz. The name of the difference signal, e.g. 'DiffB15', is taken from the coil labels of the two B-coils involved. The dashed lines show the mean values with the corresponding colours.

in the model (cf. section 4.7), cannot explain the different amplitudes, as the damping should be similar for all B-coils, which is not observed. Thus, the integrated B-coil data required in the locked phase cannot be guaranteed to be correct.

The present work provides the basis for combining the different coil types so that

the magnetic measurements in the rotating and locked phases can be interpreted, although the cause of the uncertainty in the B-coil data must first be clarified before the measurements can be used.

6 Application of the model

The model described in section 4.4 can now be used to determine the poloidal mode composition (cf. section 4.5) from the Mirnov coils and thus to analyse several cases. We first consider two examples, where the $m = 2$ and $m = 3$ tearing modes are decoupled and can therefore be analysed separately (cf. section 6.1), then the phase relation between coupled modes and between a tearing mode and its poloidal sidebands is analysed in section 6.2. Although a tearing mode in the perturbation current density formulation used in this work is composed of a dominant poloidal harmonic and its poloidal sidebands, we use the term tearing mode to describe the dominant poloidal harmonic. In section 6.3, the mode composition obtained from the Mirnov coils is applied to the simulated measurements of the radial field coils to prove a consistent description.

6.1 Characterisation of poloidal sidebands of tearing modes

In order to demonstrate the necessity and to study the characteristics of the poloidal sidebands with the description of the perturbation current density according to equation 4.21, an uncoupled tearing mode, e.g. a pure $m = 2$ mode, is required. Since an $m = 3$ tearing mode is not always visible in the ECE data (the example shown in figure 3.1 represents an exception) due to the applied settings or an incomplete temperature flattening at the $q = 3$ surface, the existence of and thus the coupling to an $m = 3$ tearing mode cannot be excluded in general. Thus, two cases are evaluated where the $m = 2$ and $m = 3$ tearing modes exist, but rotate at different frequencies and are hence known to be uncoupled. Note that in this section the term sidebands corresponds to the poloidal harmonics with $\Delta m = \pm 1$ with respect to the dominant poloidal harmonic, called tearing mode, at the selected frequency.

Figure 6.1 shows the spectrograms of the discharges 34008 and 33980 between $t = 3.16$ s and 3.65 s and between $t = 5.53$ s and 5.64 s respectively. It can be seen in figure 6.1 a) that the coupled modes separate at about $t = 3.4$ s, until they couple again at about $t = 3.44$ s (indicated by the white box). In the case of discharge 33980 (figure 6.1 b)) there also exists a phase (white box) where the modes rotate at different frequencies until they couple at about $t = 5.58$ s. As described in section 3.4, a separate analysis at the dominant frequencies is possible in the period when the modes are uncoupled.

Table 6.1 gives the relevant discharge parameters for the selected times. The decoupling of the $m = 2$ and $m = 3$ tearing modes in discharge 33980 occurs during the ramp-down of the plasma current, i.e. at a lower value of I_p . Since the toroidal magnetic field B_ϕ is the same in both cases (cf. table 6.1), the q values at the plasma edge are therefore different. In addition, the heating power P_{heat} of discharge 33980 at $t = 5.555$ s is only 40% of P_{heat} of discharge 34008 at $t = 3.41$ s.

Since we consider poloidal sidebands with $\Delta m = \pm 1$, the poloidal harmonics $\mathbf{j}_{\text{pert}}^{(m,1)}$ with $m \in \{1, 2, 3\}$ and with $m \in \{2, 3, 4\}$ are simulated for the $m = 2$ and $m = 3$ tearing modes, respectively. The poloidal mode composition is then determined from the Mirnov coils for the dominant frequencies of the $m = 2$ and $m = 3$ tearing modes separately. Contrary to the procedure described in section 4.5 and used in the rest of this work, where each poloidal harmonic $\mathbf{j}_{\text{pert}}^{(m,1)}$ – except for $\mathbf{j}_{\text{pert}}^{(1,1)}$ – is simulated on its $q = m$ surface, the poloidal sidebands with $\Delta m = \pm 1$ are now simulated on

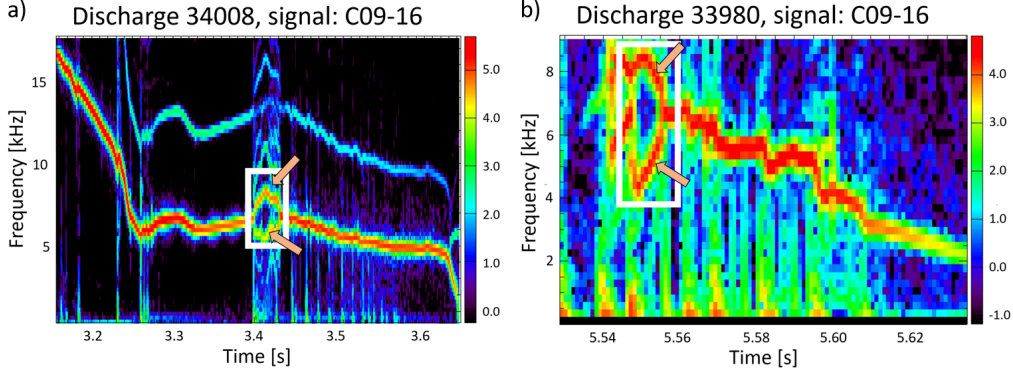


Figure 6.1: Spectrograms of the Mirnov coil signal 'C09-16' on the HFS for discharges 34008 in figure a) and 33980 in figure b). The phases in which the $m = 2$ and $m = 3$ tearing modes are decoupled are marked with white boxes in both figures. The selected frequencies $f = 7700$ Hz and $f = 5600$ Hz of the $m = 2$ and $m = 3$ tearing mode, respectively, at $t = 3.410$ s (figure a)) as well as $f = 7900$ Hz and $f = 5580$ Hz of the $m = 2$ and $m = 3$ tearing mode, respectively, at $t = 5.555$ s (figure b)) are indicated by arrows.

Parameter	34008 at $t = 3.410$ s	33980 at $t = 5.555$ s
I_p	0.8 MA	0.6 MA
B_ϕ	-2.5 T	-2.5 T
P_{heat}	6.4 MW	2.6 MW
β_p	0.67	0.68

Table 6.1: Discharge parameters for discharges 34008 at $t = 3.410$ s and 33980 at $t = 5.555$ s.

the resonant surface of the tearing mode to which they belong to (cf. figure 2.7), to account for the differences in resonant surface geometries and θ^* (cf. figure 4.17 and thus obtain the correct amplitudes. Therefore, the amplitudes $a^{(3,1)}$ of $\mathbf{j}_{\text{pert}}^{(3,1)}$ simulated on the $q = 2$ surface and $a^{(4,1)}$ of $\mathbf{j}_{\text{pert}}^{(4,1)}$ simulated on the $q = 3$ surface will be larger than in the simulations where $\mathbf{j}_{\text{pert}}^{(m,1)}$ is simulated on the $q = m$ surface: As the $m = 3$ and $m = 4$ poloidal harmonics are simulated on a resonant surface further inside, their amplitudes at the simulated measurement position $a_{\text{sim},k}^{(m,1)}$ are smaller and therefore larger amplitudes $a^{(m,1)}$ are required for the same measured amplitudes.

Tables 6.2 and 6.3 show the amplitudes $a^{(m,1)}$ of the poloidal sidebands and the relative phases

$$\varphi_{m=ij} = \varphi^{(i,1)} - \varphi^{(j,1)} \quad , \quad (6.1)$$

where i and j are the poloidal mode numbers with i being the dominant poloidal harmonic, for the discharges 34008 at $t = 3.41$ s and 33908 at $t = 5.555$ s for the frequencies of the $m = 2$ and $m = 3$ tearing modes. In the case of the $m = 2$ tearing mode (table 6.2), the amplitude $a^{(3,1)}$ is considerably larger than $a^{(1,1)}$ for both discharges. Especially the large value of $a^{(3,1)}$ for discharge 33980, which describes the $m = 3$ sideband, might indicate the contribution of an $m = 3$ kink mode (cf. section 3.3) in resonance with the $m = 3$ component. The phase relation between the $m = 1$ and $m = 2$ Fourier components appears to be close to π , while the relative phases $\varphi_{m=23}$ are quite different. The amplitudes of the poloidal sidebands of the

$m = 3$ tearing mode (table 6.3) are more similar, particularly in the case of discharge 33980. The phase relations of the $m = 2$ sideband to the $m = 3$ poloidal harmonic are similar for both discharges with $\varphi_{m=32} \approx 3/4\pi$, while $\varphi_{m=34}$ are quite different in the case of the $m = 3$ tearing mode.

Discharge	t [s]	f [Hz]	$a^{(1,1)}$	$a^{(3,1)}$	$\varphi_{m=21}$	$\varphi_{m=23}$
34008	3.410	7700	0.07	0.30	0.91 π	-0.30 π
33980	5.555	7900	0.07	0.78	0.89 π	0.89 π

Table 6.2: Normalised amplitudes, i.e. the dominant mode amplitude (here $a^{(2,1)}$) is 1.0, and relative phases of the poloidal sidebands of a (2, 1) rotating tearing mode.

Discharge	t [s]	f [Hz]	$a^{(2,1)}$	$a^{(4,1)}$	$\varphi_{m=32}$	$\varphi_{m=34}$
34008	3.410	5600	0.14	0.33	0.69 π	-0.14 π
33980	5.555	5580	0.20	0.21	0.83 π	-0.65 π

Table 6.3: Normalised amplitudes and relative phases of the poloidal sidebands of a (3, 1) rotating tearing mode. Here, the dominant mode amplitude is $a^{(3,1)} = 1.0$.

The analysis of SXR data shows the presence of a $m = 1$ mode – presumably a kink mode – phase-locked to the $m = 2$ mode in both cases, which cannot be separated from the contribution of the $m = 1$ sideband simulated on the $q = 2$ surface. Note that, as mentioned above, the amplitude $a^{(1,1)}$ determined for the $m = 1$ poloidal harmonic is smaller than the one that would be obtained for an $m = 1$ mode on the $q = 1$ surface further in. This might explain the fact that the amplitudes $a^{(1,1)}$ are not large compared to $a^{(3,1)}$ in the two cases of table 6.2.

The importance of considering the poloidal sidebands of any kind is particularly apparent in the case of discharge 33980. The measured amplitudes $a_{\text{meas},k}$ cannot be reproduced by the $m = 2$ poloidal harmonic $j_{\text{pert}}^{(2,1)}$ alone, as shown in figure 6.2, where $a_{\text{meas},k}$ and the phases $\varphi_{\text{meas},k}$ of the Mirnov coils at the frequencies $f = 7900$ Hz, corresponding to the $m = 2$ mode, and $f = 5580$ Hz, corresponding to the $m = 3$ mode, are shown together with the simulated Mirnov amplitudes and phases. The consideration of the poloidal sidebands improves the agreement from $\alpha = 24.2^\circ$ to $\alpha = 9.54^\circ$ for the $m = 2$ tearing mode and from $\alpha = 21.5^\circ$ to $\alpha = 8.73^\circ$ for the $m = 3$ tearing mode.

The improvement in the agreement between measurement and simulation results by considering the poloidal sidebands is less significant for the case of discharge 34008 as shown in figure 6.3. The addition of sidebands with $\Delta m = \pm 1$ improves α from 18.7° to 14.5° for the $m = 2$ tearing mode and from $\alpha = 18.7^\circ$ to $\alpha = 14.1^\circ$ for the $m = 3$ tearing mode.

Given these cases, it is difficult to conclude on a general rule for the amplitudes of the poloidal sidebands resulting from the formulation according to equation 4.21 and the phase relations of these sidebands to the tearing modes. Although we are confident that the $m = 2$ and $m = 3$ tearing modes are decoupled, there could still be an ideal kink response contributing to the poloidal sidebands of the dominant m component in addition to the sidebands arising from the perturbation current density formulation. In particular, the amplitudes of the poloidal sidebands seem to differ significantly between cases. The phase relation between a tearing mode and its poloidal sidebands is further investigated in the following section 6.2.

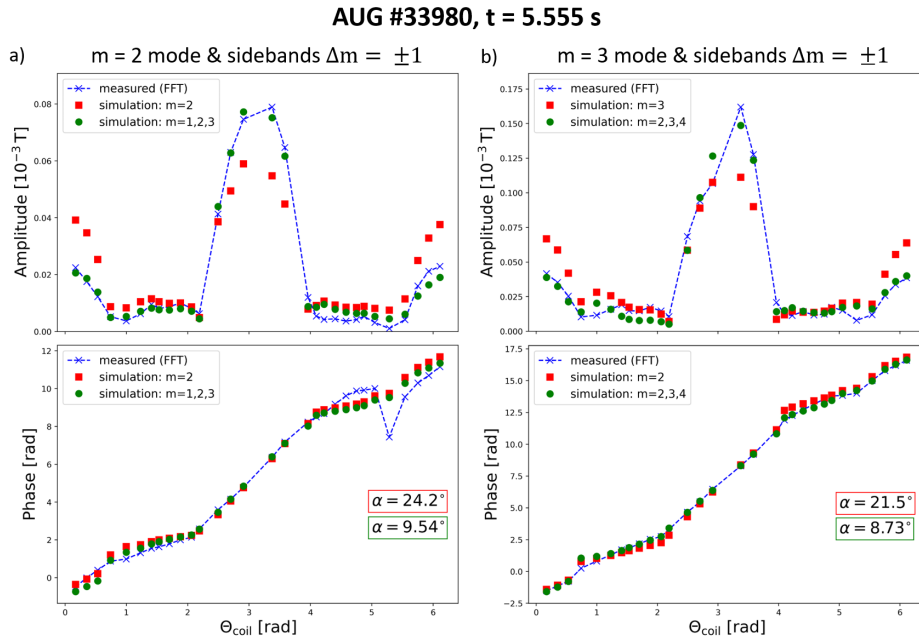


Figure 6.2: Measured amplitudes and phases of the Mirnov coils (blue crosses) at the $m = 2$ mode frequency $f = 7900$ Hz (figure a)) and at the $m = 3$ mode frequency $f = 5580$ Hz (figure b)), where the dashed blue line is only for guidance, together with the simulated amplitudes and phases for $j_{\text{pert}}^{(2,1)}$ (figure a)) and for $j_{\text{pert}}^{(3,1)}$ (figure b)) alone (red squares) and for $j_{\text{pert}}^{(m,1)}$ with $m \in \{1, 2, 3\}$ (figure a)) and $m \in \{2, 3, 4\}$ (figure b)) (green dots). The values of α are given in the lower right corner of figures a) and b), where the upper value corresponds to the simulation with only one and the lower value corresponds to the simulation with three Fourier components.

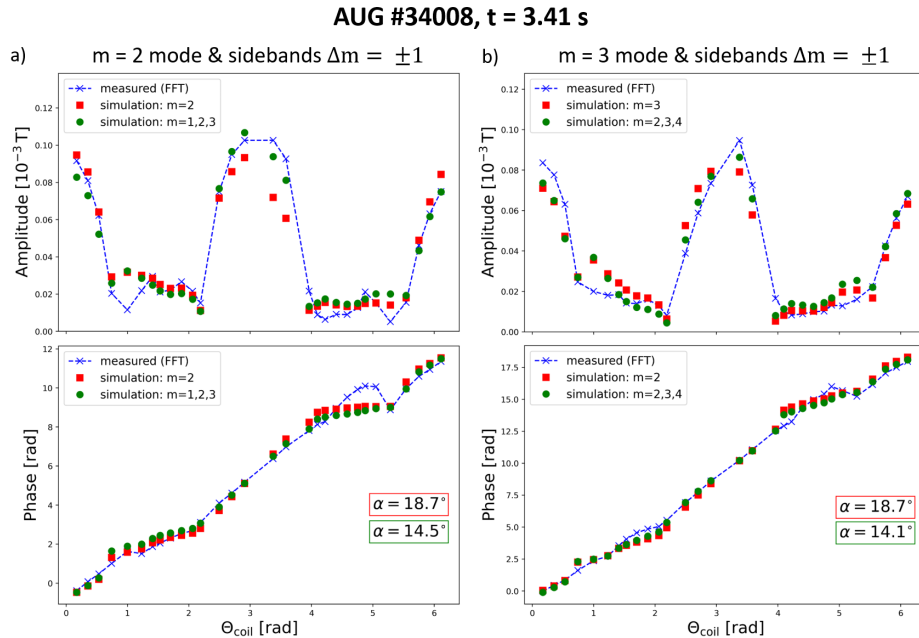


Figure 6.3: Measured and simulated amplitudes and phases of the Mirnov coils as in figure 6.2. In discharge 34008 at $t = 3.41$ s, the $m = 2$ mode frequency is $f = 7700$ Hz (figure a)) and the $m = 3$ tearing mode rotates at $f = 5600$ Hz (figure b)).

6.2 Determination of mode composition for different β

As shown in section 6.1, the description of the perturbation current density according to 4.21 requires the consideration of poloidal sidebands. Thus, to study the phase relations between coupled modes and a single mode and its sidebands, we need to distinguish between cases where a (3, 1) mode is present on the $q = 3$ surface and cases where the $m = 3$ component corresponds to a poloidal sideband of the $m = 2$ mode on the $q = 2$ surface.

This is achieved using several discharges analysed in [22], where coupled $m = 2$ and $m = 3$ modes are visible in the ECE data which are listed in table 6.4. Determining the mode composition of these discharges from Mirnov data, as described in section 4.5, gives a normalised $m = 3$ mode amplitude $a^{(3,1)} > 0.25$ in each case.

Coupled $m = 2$ and $m = 3$ modes:

Discharge	t [s]	β_p	f [Hz]
34536	7.56	0.25	479
33193	4.71	0.97	751
34635	1.85	0.30	759
31967	7.05	0.26	1060
35794	3.41	0.29	1300
35750	8.16	0.15	1550
34683	1.44	0.22	1732
33656	6.94	0.46	1967
34590	6.38	0.545	2019
34590	6.28	1.11	2251
35723	6.30	0.54	3249
34904	5.14	0.96	5189
34800	5.37	0.895	5802
33570	7.20	1.09	6857
34800	5.66	1.26	7225
34800	5.76	1.39	8030
34154	3.00	2.14	8441
34810	5.76	1.34	8721
34110	3.60	1.10	9201
33570	6.67	0.92	9247
34158	2.96	1.52	9550
33570	8.17	1.31	9832
34154	5.342	1.37	10094
34154	5.00	1.68	11333

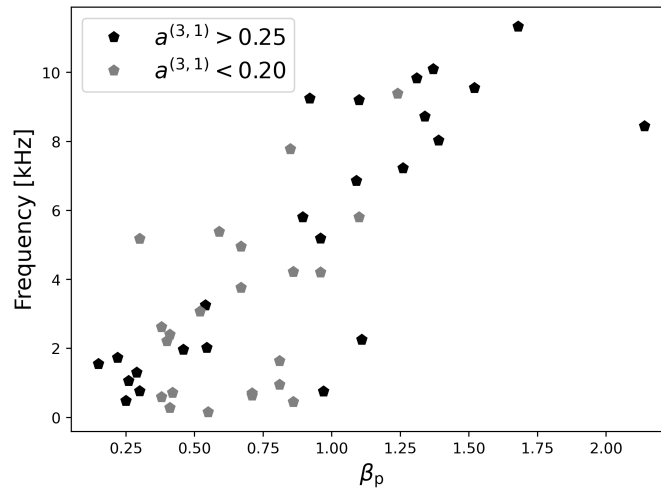
Table 6.4: Discharges with coupled $m = 2$ and $m = 3$ modes and their times, analysed (among others) in [22], together with the mode frequencies and β_p .

Moreover, cases with a dominant $m = 2$ mode and a small amplitude of the $m = 3$ poloidal harmonic, $a^{(3,1)} < 0.20$, were taken (cf. table 6.5) to analyse the phase relation of a (2, 1) mode to its sidebands in the description used in this work. Since the rotation of the plasma in AUG is mainly due to the NBI injection, which increases the plasma β , there is an almost linear dependence between the poloidal plasma beta, β_p , and the mode frequency, as shown in figure 6.4.

As mentioned in section 2.4.5, tearing modes were expected to couple constructively at the LFS [50], since the magnetic flux surfaces have a smaller distance on the LFS and parallel currents are attracted by the $\mathbf{j} \times \mathbf{B}$ force (cf. equation 2.2). In

Dominant $m = 2$ mode and small $a^{(3,1)}$:

Discharge	t [s]	β_p	f [Hz]
40488	1.53	0.55	153
38628	1.84	0.41	280
39661	5.70	0.86	448
34776	2.48	0.38	593
40703	7.10	0.71	635
41417	3.17	0.71	698
38706	3.00	0.42	719
41417	3.50	0.81	946
38761	2.70	0.81	1640
41117	2.12	0.40	2211
41417	2.24	0.41	2400
35354	3.60	0.38	2621
41417	4.46	0.52	3075
34776	2.36	0.67	3757
41417	3.82	0.96	4207
36171	5.61	0.86	4220
35354	3.41	0.67	4952
32388	2.50	0.30	5177
35667	1.66	0.59	5380
41417	4.15	1.10	5804
41417	1.81	0.85	7779
41091	6.05	1.24	9383

Table 6.5: Discharges with a dominant $m = 2$ mode and small $a^{(3,1)} < 0.20$ and their times, mode frequencies and β_p .**Figure 6.4:** Dependence of the mode frequency on β_p for discharges listed in table 6.5, where the relative amplitude $a^{(3,1)} < 0.20$, and table 6.4, where the relative amplitude $a^{(3,1)} > 0.25$.

[22] it was shown, by analysing the phase relation with ECE data and the model developed in [29] using Mirnov data, that the phase relation between the $m = 2$ and $m = 3$ tearing modes in AUG can vary from 0, i.e. constructive coupling on the LFS, to π , i.e. constructive coupling on the HFS, depending on the plasma pressure and rotation velocity. Using Mirnov measurements and the model developed in this work,

the results of [22] are confirmed. This is shown in figure 6.5, where the relative phases between $m = 2$ and $m = 3$, denoted according to equation 6.1, are compared with the phase relation determined from ECE and modelled magnetic data in [22]. Note that in [22], the poloidal harmonics $m \in \{2, 3, 4, 5\}$ instead of $m \in \{1, 2, 3, 4\}$ were used to infer the poloidal mode composition, which however gives a similar result for $\varphi_{m=32}$, indicating that – for large amplitudes $a^{(3,1)}$ – the $m = 1$ Fourier component can be ignored for determining the phase relation between coupled $m = 2$ and $m = 3$ tearing modes. As figure 6.5 shows, it is possible to derive information about the poloidal mode structure, in particular the phase relation between coupled modes, using only magnetic measurements, which are always available, and the model described in this work.

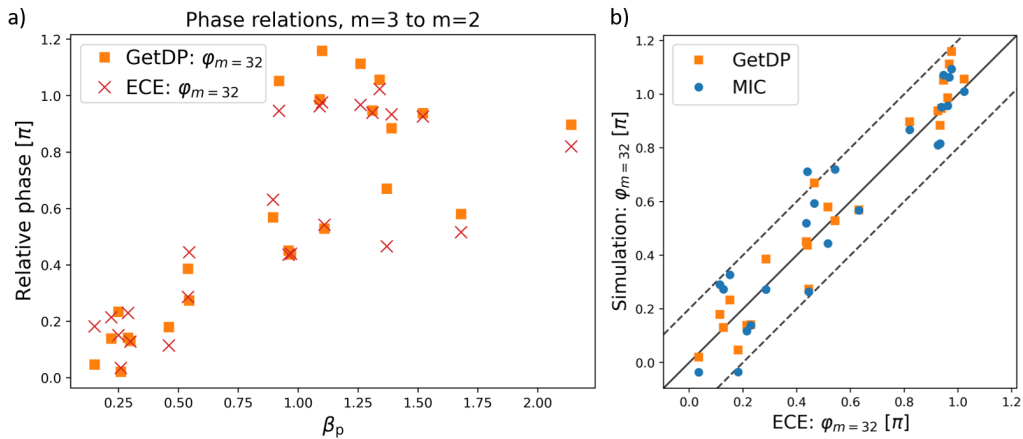


Figure 6.5: Figure a) shows the phase relations $\varphi_{m=32}$ determined from ECE data in [22] (red crosses) and using the model described in section 4.4 (orange squares) for the discharges listed in table 6.4 in dependence of β_p . The direct comparison between the phases is shown in figure b) (orange squares), where the phase relations determined in [22] using the MIC code [29] are also shown (blue dots). The solid and dashed black lines represent the identity and the identity line shifted by $\pm 0.20\pi$, respectively.

If the poloidal sidebands represent a correction to the description of the perturbation current density that is independent of β_p , a fixed relation of the sidebands to the mode is expected. We assume that the $m = 1$ component is always a poloidal sideband, so that all phases, $\varphi^{(1,1)}$, determined for the cases listed in both tables 6.4 and 6.5 are taken for the evaluation of the phase relation between a tearing mode and its sideband. As only cases with a dominant $m = 2$ mode or coupled $m = 2$ and $m = 3$ modes were selected, the $m = 2$ component always describes a tearing mode on the $q = 2$ surface. In the cases, where the mode amplitude $a^{(3,1)} < 0.20$, listed in table 6.5, the $m = 3$ component is presumably a poloidal sideband of the $m = 2$ mode. We use the phases $\varphi^{(4,1)}$ determined for the cases of table 6.4, where an $m = 3$ mode is present on the $q = 3$ surface and the $m = 4$ component is assumed to correspond to its $\Delta m = +1$ sideband. In order to see the dominant phase relations, the relative phases $\varphi_{m=12}$, $\varphi_{m=32}$ and $\varphi_{m=43}$ (cf. equation 6.1) are shown in figure 6.6. Figure a) shows the relative phases depending on β_p , figures 6.6 b), c) and d) show histograms of $\varphi_{m=12}$, $\varphi_{m=32}$ and $\varphi_{m=43}$, respectively. The phase relation between the $m = 1$ and $m = 2$ poloidal harmonics is close to π , especially for higher β_p , with a mean value of $\varphi_{m=12}$ of 0.98π (cf. figure 6.6 b)). Figure 6.6 c) shows that the phase relation $\varphi_{m=32}$ has no clear peak at a certain value, which could be

partly explained by the fact that in some cases there might be an $m = 3$ mode on the $q = 3$ surface, which is considered here as a sideband and has a phase relation that depends on β_p (cf. figure 6.5). Figure 6.6 d) suggests that the phase relation of $\varphi_{m=43}$ has a peak at about $-\pi/4$ or slightly shifted further to the negative, with a mean value of -0.18π . However, this peak is not as clear as in the case of figure b) and would need to be confirmed with more data. Cases with $\beta_p \leq 0.5$ are marked by lighter colours in figures b), c) and d) to show where there is scatter in the phase relations at low β_{pol} .

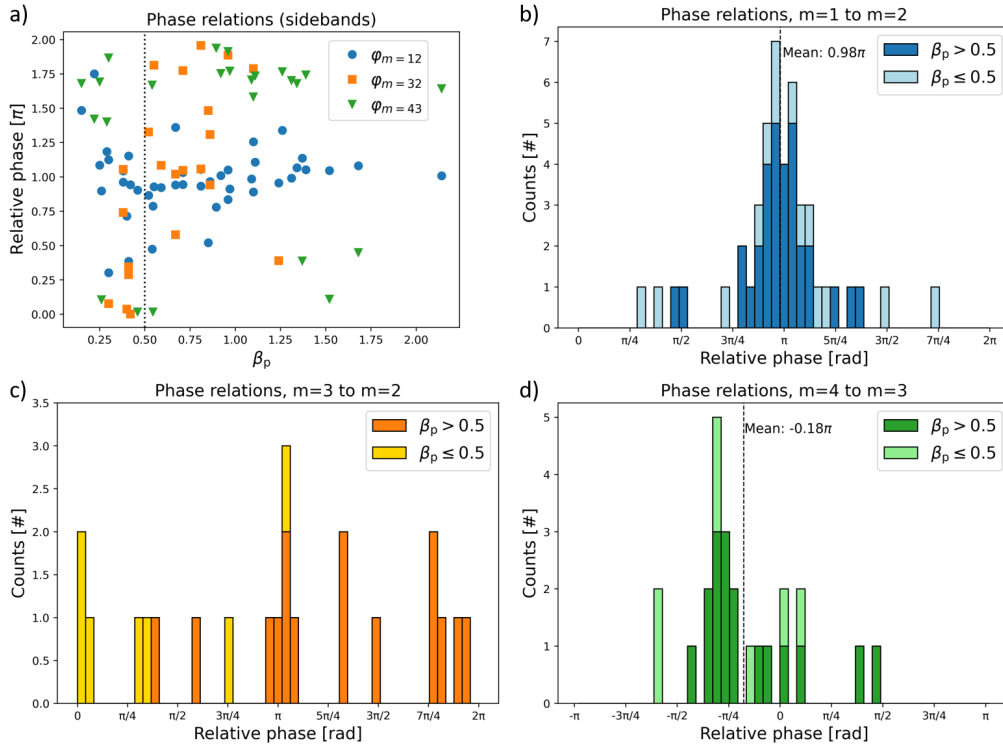


Figure 6.6: Phase relations $\varphi_{m=12}$ (blue), $\varphi_{m=32}$ (orange) and $\varphi_{m=43}$ (green). Figure a) shows $\varphi_{m=12}$ (blue dots), $\varphi_{m=32}$ (orange squares) and $\varphi_{m=43}$ (green triangles) depending on β_p , where $\beta_p = 0.5$ is marked by a vertical dashed line; figure b), c) and d) show histograms of the individual phase relations, where values with $\beta_p \leq 0.5$ are marked with lighter colours. The mean value is given in figures b) and d), where a peak is visible in the histogram.

The phase relations between the $m = 2$ tearing mode and its poloidal sidebands with $\Delta m = \pm 1$ determined in figure 6.6 are compared with the phase relations determined using the CASTOR3D [36] calculations presented in figure 2.7 (cf. section 2.4.2), where an $m = 2$ tearing mode was found. Figure 6.7 shows the phases of the poloidal harmonics $m = 1$, $m = 2$ and $m = 3$ at the resonant $q = 2$ surface. As described in section 2.4.1, the solution of the tearing mode equation 2.32 describes a perturbation current density which changes sign at the resonant surface as shown in figure 2.4. This is also the case for the CASTOR3D calculations of figure 2.7 and can be seen by the phase jump of π in figure 6.7. The phase difference between the $m = 2$ tearing mode and its poloidal sidebands is π , which corresponds to the phase relations $\varphi_{m=12}$ shown in figure 6.6 b). The phase relation can be changed by the existence of another resonant surface in the plasma and potentially a (small) tearing mode on that resonant surface. As there is a $q = 3$ and a $q = 4$ surface in the discharges used for this evaluation, the phase differences $\varphi_{m=32}$ and $\varphi_{m=43}$ can be

different from π as it is the case in figure 6.6 c) and d).

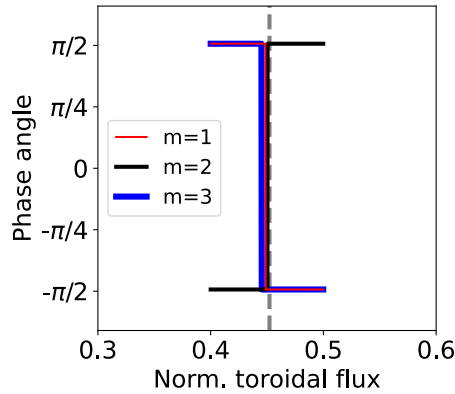


Figure 6.7: Phase angle of the $m = 1$ (red), $m = 2$ (black) and $m = 3$ (blue) poloidal harmonics shown in figure 2.7 at the resonant $q = 2$ surface at a normalised toroidal flux of 0.45. (Figure: courtesy of Jonas Puchmayr, MPI for Plasma Physics)

The assumption that at higher frequencies, and thus higher differential rotation between the $q = 2$ and $q = 3$ surfaces, the contribution at the $q = 3$ surface no longer plays a role and the phase relation $\varphi_{m=32}$ between the $m = 2$ tearing mode and its $m = 3$ sideband approaches π could not be confirmed. However, the result from the linear MHD calculation that the tearing mode is in antiphase to its sidebands could be reproduced for the phase relation between the $m = 1$ and $m = 2$ poloidal harmonics.

6.3 Simultaneous application to Mirnov and radial field coils

Parts of the content, figures and text of this section are included in a publication accepted by Plasma Physics and Controlled Fusion (DOI 10.1088/1361-6587/adc0bd), of which the author of this thesis is the first author.

After correcting the simulated amplitudes of the Mirnov coils to account for the lack of radial currents in the vessel flange structure (cf. section 4.6.1) and with the effective parameters $\sigma_{\text{vessel,eff}}$ and $R_{\text{saddle,eff}}$ determined in section 4.6.2, the model can be used to interpret the magnetic measurements of the different coil types in AUG. The simulated complex measurements $\tilde{B}_{\text{sim},k}$, with the complex amplitudes $\tilde{a}^{(m,1)}$ (cf. equation 4.36) determined from the Mirnov coils, should also agree with the measured complex amplitudes $\tilde{B}_{\text{meas},k}$ for radial field coils k . We will show below that this is the case for Ballooning and saddle coils.

Figures 6.8 and 6.9 show the comparison between $\tilde{B}_{\text{sim},k}$ and $\tilde{B}_{\text{meas},k}$ for different coils k with $\tilde{a}^{(m,1)}$ determined from the Mirnov coils for the discharges 38761 and 40703 at the frequencies $f = 1640$ Hz and $f = 635$ Hz, respectively. The plots a) show \tilde{B}_{meas} of the Mirnov coils as blue crosses. The dashed blue line connecting the measured values is intended as a guide for the eye. \tilde{B}_{sim} of the Mirnov coils are shown as red dots in the plots a). The relative amplitudes and phases of $\tilde{j}_{\text{pert}}^{(m,1)}$ with $m \in \{1, 2, 3, 4\}$ are given in the legend. The complex coefficients $\tilde{a}^{(m,1)}$ determined from the Mirnov coils are used to calculate $\tilde{B}_{\text{sim},k}$ for the Ballooning coils, the B-coils and the saddle coils (red dots in plots b) and c)) which are compared with $\tilde{B}_{\text{meas},k}$ (blue crosses in plots b) and c)).

The amplitudes of the measured saddle and B-coils in the plots c) are determined from the difference signals of the coil pairs that are $\Delta\Phi_{\text{coil}} = \pi$ apart, which is already

done in hardware for the saddle coils (cf. section 3.3). Two measured difference signals of the same coil types, e.g. 'SATew' and 'SATns', should have the same amplitudes for rotating tearing modes, which is not exactly the case. Therefore, error bars are introduced in the plots c) that represent the deviations of the measured amplitudes of the difference signals of the same coil type. For the B-coils, large error bars are present in both cases and the simulated mean B-coil amplitudes do not match the measured ones. Owing to the limited availability of usable B-coil data for rotating modes, as discussed in section 5.2, and the fact that the B-coils are surrounded by additional structures that are difficult to replicate and are therefore not included in the model, the B-coil data is shown here only for the sake of completeness.

As explained earlier, only the radial measurements are available for locked modes. This means that $\tilde{B}_{\text{meas},k}$ of the toroidal arrays of the Ballooning, saddle and B-coils alone must be used to determine $\tilde{a}^{(m,1)}$ of locked modes, which is more challenging than in the rotating phase due to the limited number of toroidally distributed coils at different poloidal positions. As previously mentioned, the procedure for determining the measured amplitudes $a_{\text{meas},k}$ and phases $\varphi_{\text{meas},k}$ at one poloidal position from a toroidal array of coils is described in [53], the extension for using toroidally distributed Ballooning coils at different minor radii and tilting angles is shown in section 5.2. The limited availability of $\tilde{B}_{\text{meas},k}$ for radial field coils k is illustrated here for the rotating case, where toroidally distributed coils are not required. The plots a) of figures 6.8 and 6.9 show the simulated (green dots) and measured (black crosses) results of the Ballooning coil 'B31-01', the B-coils 'Bu1' and 'Bl1' and the saddle coil signal 'SATew' in addition to the Mirnov results. As expected and consistent with the measured amplitudes, the amplitudes of these radial coils are smaller than or equal to the Mirnov amplitudes due to the effect of the conducting structures even if Ballooning and B-coils are closer to the resonant surface. The phase in plot a) is shifted for comparison by the different toroidal coil positions via

$$n (\Phi_{\text{coil},r} - \Phi_{\text{coil},\theta})$$

with $\Phi_{\text{coil},r}$ the toroidal positions of the radial field coils 'B31-01', 'Bu1', the signal 'SATew' and 'Bl1'. The angle $\Phi_{\text{coil},\theta}$ denotes the toroidal position of the poloidal array of the Mirnov coils 'C09' (cf. section 3.3). There is an expected phase difference of approximate $\frac{\pi}{2}$ between the radial and the poloidal perturbation field components, which is reproduced by the simulation.

Figures 6.8 and 6.9 show that there is agreement for all coil types that can be used in the rotating phase, i.e. the measured amplitudes and phases (blue crosses) can be reproduced by the simulation (red dots) for the radial and the poloidal field coils. $\tilde{a}^{(m,1)}$ obtained from the Mirnov coils are also valid for the other coil types, confirming a consistent description of the measurements from the different coil types for rotating modes with the model described here. The small deviations between \tilde{B}_{sim} and \tilde{B}_{meas} of the Ballooning coils could be due to the poloidal tilt not being accurately documented, which might be investigated in future research. The measured complex amplitudes of the B-coils cannot be determined with sufficient accuracy, at least in the rotating case. As discussed in section 5.2, the reasons for this must be found and, if possible, eliminated before the integrated B-coil data can be used for the purpose of studying locked modes.

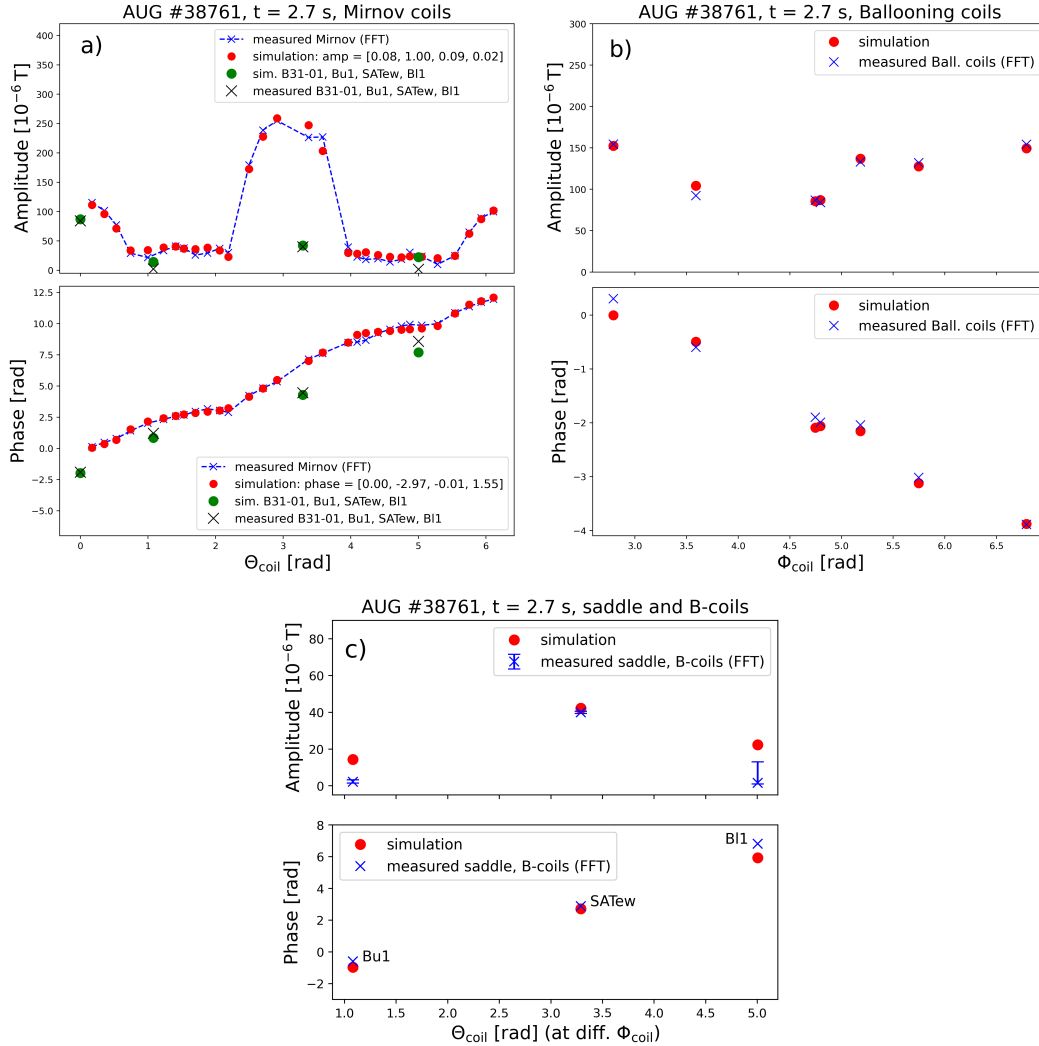


Figure 6.8: Comparison of simulated (red dots) and measured (blue crosses) amplitudes and phases for discharge 38761 at $t = 2.7$ s, where the tearing mode was rotating at a frequency $f = 1640$ Hz. $\tilde{a}^{(m,1)}$ with $m \in \{1, 2, 3, 4\}$ determined from the Mirnov coils (plot a)) are used to calculate the simulated amplitudes and phases for the toroidal Ballooning coils in the toroidal direction (plot b)) and for the B-coils and saddle coils in poloidal direction (plot c)). The complex amplitudes of the radial field coils are also shown in plot a) as green dots for the simulated values and black crosses for the measured values.

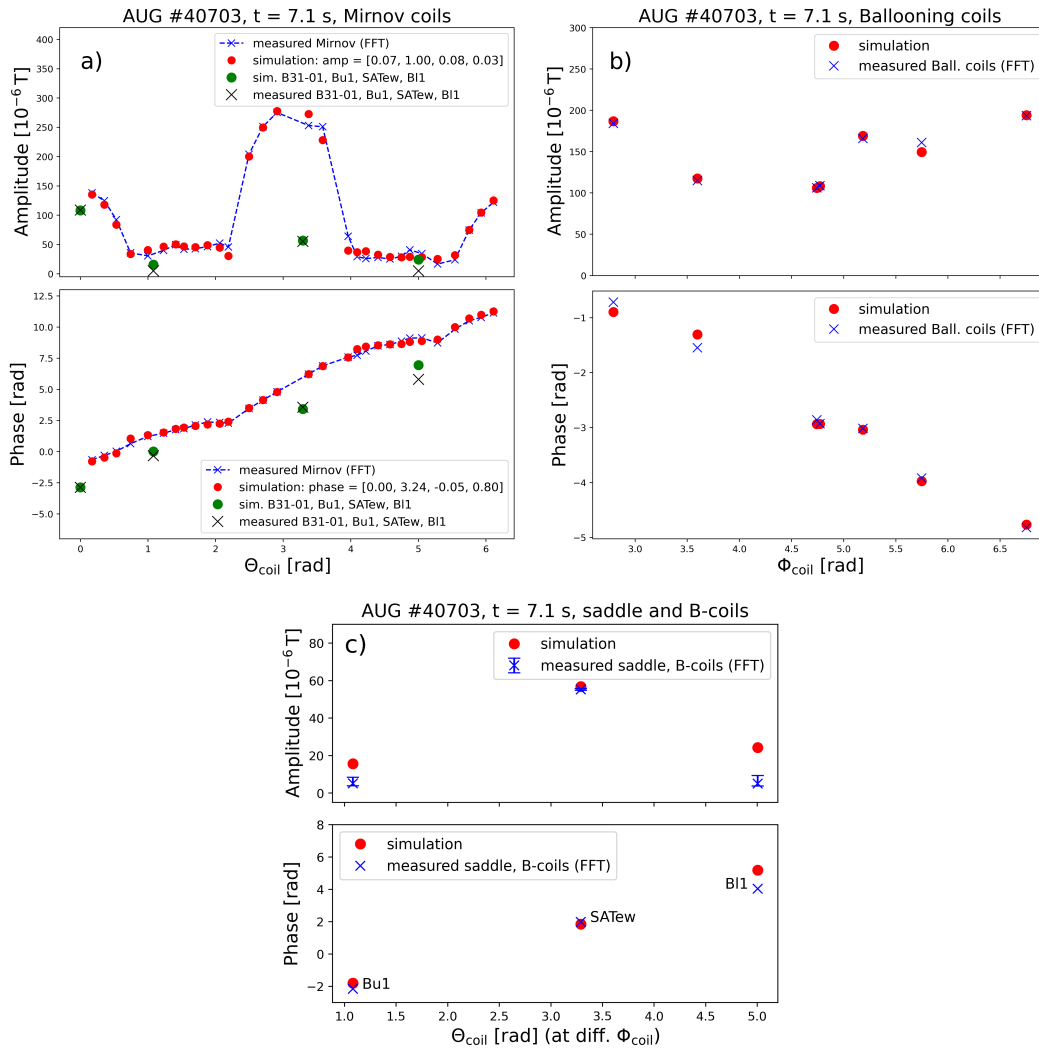


Figure 6.9: Same plots as in figure 6.8 for discharge 40703 at $t = 7.1$ s, for a tearing mode with $f = 635$ Hz.

7 Summary and outlook

Tearing modes, a resistive MHD instability, with a toroidal mode number $n = 1$ pose a significant challenge to the operation of large tokamaks planned in the future for the generation of usable energy via nuclear fusion. In particular, toroidally coupled modes, i.e. tearing modes with different poloidal mode numbers m rotating at the same frequency, lead to a confinement degradation and potentially to a disruption, a sudden loss of the thermal energy and the plasma current, which can severely damage the machine. The analysis of (coupled) tearing modes is therefore important for a physical understanding and for the initiation of countermeasures. For this purpose, the poloidal mode composition of the tearing modes, i.e. the complex amplitudes with amplitudes $a^{(m,1)}$ and phases $\varphi^{(m,1)}$ of the poloidal harmonics, must be determined, which requires magnetic measurements of the tearing modes and a model that calculates the expected measurements for each poloidal harmonic.

In the ASDEX Upgrade (AUG) tokamak, different types of passive coils are installed, which are differently affected by the frequency dependent shielding currents in the conducting structures induced by a rotating mode. For rotating modes, a poloidally arranged array of Mirnov coils is used to measure (mainly) the poloidal perturbation field of the mode. For locked modes, i.e. modes that are no longer rotating with respect to the laboratory frame, the integrated measurement of the radial field component is required, since the poloidal perturbation field component can no longer be distinguished from the poloidal equilibrium magnetic field with sufficient precision. Thus, Mirnov coils cannot be utilised for locked modes, while most radial field coils cannot be used for fast rotating modes due to the damping of the radial field component in front of conducting structures. In order to analyse the poloidal mode composition for all mode frequencies, i.e. rotating and locked modes, it is necessary to combine the radial and poloidal field measurements in a consistent manner. This requires a comparison in the low frequency range where all coils are available and where shielding currents, flowing in the vacuum vessel and other conducting structures, which might be non-toroidally symmetric, are important. An analytical formula for the influence of mirror currents on the perturbation magnetic field in front of a conducting wall in cylindrical approximation is not sufficient for an accurate description. Therefore, a three-dimensional model using FEM and implemented in the GetDP code [59] has been developed, which calculates the expected virtual measurements generated by a perturbation current density of a single helicity, so that the poloidal mode composition, i.e. $a^{(m,1)}$ and $\varphi^{(m,1)}$ for different poloidal mode numbers, can be determined due to the linearity of the problem.

The perturbation current density describing a tearing mode is set to flow parallel to the equilibrium magnetic field on the resonant surface, which is defined with a varying thickness according to the different distances between neighbouring magnetic flux surfaces. In a torus, the perturbation current density has poloidal sidebands with $\Delta m = \pm 1$. The plasma in the model is treated as vacuum, which introduces uncertainties in the determination of the mode composition that need to be considered. Relevant conducting structures affecting the measurements of the coils in AUG are implemented to include the effect of the frequency dependent shielding currents on the magnetic measurements. The frequency dependence of the virtual measurements of the poloidal and radial field components in front of a conducting wall, expected from the analytical cylindrical approximation, is shown to be modified in toroidal geometry. The distribution of the perturbation current density in a

torus according to the straight field line angle θ^* , instead of θ in a periodic cylinder, gives a non-monotonic frequency dependence of the perturbation magnetic field in front of a resistive wall on the high field side. In addition, the implementation of the support bridges of the passive stabilisation loop (PSL) is shown to be necessary to obtain a loop between the PSL and the support bridges, and thus for the observed attenuation of the measured Mirnov coil amplitudes behind the PSL. The evaluation of the integrated toroidal current in the vacuum vessel gives a resistive time scale of the wall of 5 ms, which is in agreement with values from the literature [82]. By comparing the ratio of simulated to measured results from magnetic measurements of different coil types, a correction to the amplitudes of the virtual Mirnov coil measurements and effective parameters are determined. The model provides a consistent description of the expected magnetic measurements of different coil types for all frequencies. Agreement between simulated and measured Mirnov amplitudes and phases was shown for different discharges covering a wide frequency range.

For locked modes, where only radial magnetic field measurements at far fewer poloidal positions are available, it is necessary to validate that these poloidal positions are sufficient to determine the poloidal mode composition. By comparing the complex vectors of the virtual radial field measurements for two different poloidal harmonics, it is shown that the $m = 2$ poloidal harmonic can be distinguished with the radial field coils from the $m = 3$ poloidal harmonic, which are supposed to be the most relevant tearing modes in terms of disruptions. The model is capable of calculating the electromagnetic problem with non-conducting structures, corresponding to the case of a locked mode. A method is presented to determine the poloidal mode composition directly from toroidally and poloidally distributed magnetic measurements using the real part of the simulation result, which is particularly useful for measurement coils installed at the same poloidal positions but at different radial positions with different tilting angles.

In this work, we apply the model to rotating modes, where more magnetic measurements are available at different poloidal positions. Two discharges, where the $m = 2$ and $m = 3$ tearing modes are known to be decoupled, show the importance of considering the poloidal sidebands with $\Delta m = \pm 1$. In order to conclude a general phase relation between the different poloidal harmonics, multiple discharges are analysed, distinguishing between the $m = 3$ poloidal harmonic describing a tearing mode and a poloidal sideband belonging to the $m = 2$ tearing mode. The result found in [22], that the phase relation between coupled $m = 2$ and $m = 3$ tearing modes can vary between 0 and π depending on the plasma β , is confirmed. The phase relation between the $m = 1$ poloidal sideband and the $m = 2$ poloidal harmonic is shown to be π as expected from theory, while the relative phase between the $m = 3$ ($m = 4$) poloidal sideband and the $m = 2$ ($m = 3$) poloidal harmonic has no clear relation and is presumably influenced by the resonant $q = 3$ ($q = 4$) surface in the plasma.

Moreover, to proof a consistent description of the different coil types, the amplitudes $a^{(m,1)}$ and phases $\varphi^{(m,1)}$ are determined from the Mirnov coils to calculate the simulated virtual measurements $\tilde{B}_{\text{sim},k}$ for all coil types. The resulting complex amplitudes $\tilde{B}_{\text{sim},k}$ are found to agree with their corresponding measured values not only for the Mirnov coils but also for radial field coils, confirming a consistent description of the different magnetic measurements.

This work provides a tool for analysing the poloidal mode structure, which can be used for all mode frequencies and magnetic measurements of different coil types. Future work could simulate the poloidal sidebands with $\Delta m = \pm 1$ on the resonant surface of the $q = m/1$ surface in addition to the simulation on the $q = m + \Delta m$

surface, or even use the radial profiles of the perturbation current density determined from stability calculations, as described in [35], to resolve the vacuum approximation. Moreover, this model might also be used in the future as a tool for determining suitable coil positions in AUG that are planned for installation in the future. Possible extensions to the model by improving the properties of and implementing new additional conducting structures could be made and are discussed in this work.

For locked mode analysis, the inconsistencies in the measured B-coil data found in this work must first be understood and, if possible, corrected before these coils can be used to determine the poloidal mode composition of locked modes using the model described here. Since locked modes inherently have the same frequency, toroidal mode coupling is thought to play an important role, which might be verified in the future. Once the B-coil data can be used, the poloidal mode structure can be analysed in (fast) rotating, locking and locked phases, so that the evolution towards a disruption, during which rotating modes often become locked, can be studied due to the consistent description of the different coil types. This will allow to analyse the relevance of mode coupling for disruptions.

The present work is an important contribution to this goal, as a consistent description of the poloidal and radial field coils is achieved by identifying and implementing the relevant conducting structures that affect the measured perturbation field. The phase relation between coupled rotating $m = 2$ and $m = 3$ tearing modes in AUG is shown to depend on β_{pol} and thus on the rotation frequency, which might indicate a preferred phase relation between locked $m = 2$ and $m = 3$ tearing modes. The use and development of the model allowed several cases to be analysed and lessons to be learnt. As Einstein said, "the joy of looking and understanding is the most beautiful gift of nature".

A Appendix

As described in section 4.4.3, the virtual coils are described via a post-calculation where the magnetic vector potential is integrated along the coil winding. For the B-coils, the points on the contour of the centre winding are taken directly from the B-coil position documentation, the saddle coil is described by two segments of a circle with radius R_{saddle} and a vertical connection between them. The contours describing the windings of the Mirnov and Ballooning coils are more complicated and described in the following sections A.1 and A.2. The calculation of the B-coil area can be found in section A.3.

A.1 Mirnov contour

Starting point is the centre of a Mirnov coil at $\phi = 0$

$$\begin{pmatrix} x_0 \\ y_0 \\ z_0 \end{pmatrix},$$

where the coordinate system introduced in section 4.2 is used. A corner point is then described by

$$\begin{pmatrix} x_0 \\ y_0 \\ z_0 \end{pmatrix} + \begin{pmatrix} \cos(d\theta) & -\sin(d\theta) & 0 \\ \sin(d\theta) & \cos(d\theta) & 0 \\ 0 & 0 & 1 \end{pmatrix} \cdot \begin{pmatrix} \Delta y \cdot N \\ \pm \frac{\Delta x}{2} \\ \pm \frac{\Delta z}{2} \end{pmatrix} = \begin{pmatrix} x_0 \mp \frac{\Delta x}{2} \cdot \sin(d\theta) + \Delta y \cdot N \cdot \cos(d\theta) \\ y_0 \pm \frac{\Delta x}{2} \cdot \cos(d\theta) + \Delta y \cdot N \cdot \sin(d\theta) \\ z_0 \pm \frac{\Delta z}{2} \end{pmatrix},$$

where $\Delta x = 45$ mm is the width of a Mirnov coil, $\Delta y = 1$ mm is the vertical distance between 2 windings, $N \in [-65, 65]$ is the number of a specific winding, $\Delta z = 61.647$ mm is the effective length of a coil and $d\theta$ is the coil orientation relative to the horizontal. The vectors connecting the corner points at $\phi = 0$ are

$$\begin{pmatrix} \cos(d\theta) & -\sin(d\theta) & 0 \\ \sin(d\theta) & \cos(d\theta) & 0 \\ 0 & 0 & 1 \end{pmatrix} \cdot \begin{pmatrix} 0 \\ \mp \Delta x \\ 0 \end{pmatrix} = \begin{pmatrix} \pm \Delta x \cdot \sin(d\theta) \\ \mp \Delta x \cdot \cos(d\theta) \\ 0 \end{pmatrix} \text{ and } \begin{pmatrix} 0 \\ 0 \\ \mp \Delta z \end{pmatrix}.$$

As the Mirnov coils are located at $\phi_{\text{eval}} \neq 0$, the corner points and the connecting vectors have to be rotated around the y -axis by

$$R_y(\phi_{\text{eval}}) = \begin{pmatrix} \cos(\phi_{\text{eval}}) & 0 & \sin(\phi_{\text{eval}}) \\ 0 & 1 & 0 \\ -\sin(\phi_{\text{eval}}) & 0 & \cos(\phi_{\text{eval}}) \end{pmatrix}$$

. Using the parameterisation, the 4 lines of the contour are defined as follows:

$$R_y(\phi_{\text{eval}}) \cdot \begin{pmatrix} x_0 + A \cdot \sin(d\theta) + \Delta y \cdot N \cdot \cos(d\theta) \\ y_0 - A \cdot \cos(d\theta) + \Delta y \cdot N \cdot \sin(d\theta) \\ z_0 + \frac{\Delta z}{2} \end{pmatrix} =$$

$$\begin{pmatrix} \cos(\phi_{\text{eval}}) \cdot (x_0 + A \cdot \sin(d\theta) + \Delta y \cdot N \cdot \cos(d\theta)) + \sin(\phi_{\text{eval}}) \cdot (z_0 + \frac{\Delta z}{2}) \\ y_0 - A \cdot \cos(d\theta) + \Delta y \cdot N \cdot \sin(d\theta) \\ -\sin(\phi_{\text{eval}}) \cdot (x_0 + A \cdot \sin(d\theta) + \Delta y \cdot N \cdot \cos(d\theta)) + \cos(\phi_{\text{eval}}) \cdot (z_0 + \frac{\Delta z}{2}) \end{pmatrix}$$

with $A \in [-\frac{\Delta x}{2}, \frac{\Delta x}{2}]$,

$$R_y(\phi_{\text{eval}}) \cdot \begin{pmatrix} x_0 + \frac{\Delta x}{2} \cdot \sin(d\theta) + \Delta y \cdot N \cdot \cos(d\theta) \\ y_0 - \frac{\Delta x}{2} \cdot \cos(d\theta) + \Delta y \cdot N \cdot \sin(d\theta) \\ z_0 - A \end{pmatrix} =$$

$$\begin{pmatrix} \cos(\phi_{\text{eval}}) \cdot (x_0 + \frac{\Delta x}{2} \cdot \sin(d\theta) + \Delta y \cdot N \cdot \cos(d\theta)) + \sin(\phi_{\text{eval}}) \cdot (z_0 - A) \\ y_0 - \frac{\Delta x}{2} \cdot \cos(d\theta) + \Delta y \cdot N \cdot \sin(d\theta) \\ -\sin(\phi_{\text{eval}}) \cdot (x_0 + \frac{\Delta x}{2} \cdot \sin(d\theta) + \Delta y \cdot N \cdot \cos(d\theta)) + \cos(\phi_{\text{eval}}) \cdot (z_0 - A) \end{pmatrix}$$

with $A \in [-\frac{\Delta z}{2}, \frac{\Delta z}{2}]$,

$$R_y(\phi_{\text{eval}}) \cdot \begin{pmatrix} x_0 - A \cdot \sin(d\theta) + \Delta y \cdot N \cdot \cos(d\theta) \\ y_0 + A \cdot \cos(d\theta) + \Delta y \cdot N \cdot \sin(d\theta) \\ z_0 - \frac{\Delta z}{2} \end{pmatrix} =$$

$$\begin{pmatrix} \cos(\phi_{\text{eval}}) \cdot (x_0 - A \cdot \sin(d\theta) + \Delta y \cdot N \cdot \cos(d\theta)) + \sin(\phi_{\text{eval}}) \cdot (z_0 - \frac{\Delta z}{2}) \\ y_0 + A \cdot \cos(d\theta) + \Delta y \cdot N \cdot \sin(d\theta) \\ -\sin(\phi_{\text{eval}}) \cdot (x_0 - A \cdot \sin(d\theta) + \Delta y \cdot N \cdot \cos(d\theta)) + \cos(\phi_{\text{eval}}) \cdot (z_0 - \frac{\Delta z}{2}) \end{pmatrix}$$

with $A \in [-\frac{\Delta x}{2}, \frac{\Delta x}{2}]$,

$$R_y(\phi_{\text{eval}}) \cdot \begin{pmatrix} x_0 - \frac{\Delta x}{2} \cdot \sin(d\theta) + \Delta y \cdot N \cdot \cos(d\theta) \\ y_0 + \frac{\Delta x}{2} \cdot \cos(d\theta) + \Delta y \cdot N \cdot \sin(d\theta) \\ z_0 + A \end{pmatrix} =$$

$$\begin{pmatrix} \cos(\phi_{\text{eval}}) \cdot (x_0 - \frac{\Delta x}{2} \cdot \sin(d\theta) + \Delta y \cdot N \cdot \cos(d\theta)) + \sin(\phi_{\text{eval}}) \cdot (z_0 + A) \\ y_0 + \frac{\Delta x}{2} \cdot \cos(d\theta) + \Delta y \cdot N \cdot \sin(d\theta) \\ -\sin(\phi_{\text{eval}}) \cdot (x_0 - \frac{\Delta x}{2} \cdot \sin(d\theta) + \Delta y \cdot N \cdot \cos(d\theta)) + \cos(\phi_{\text{eval}}) \cdot (z_0 + A) \end{pmatrix}$$

with $A \in [-\frac{\Delta z}{2}, \frac{\Delta z}{2}]$.

A.2 Ballooning coil contour

Similar to the contour of the Mirnov coils, the Ballooning coils are described by a path consisting of 4 lines. We use the outer winding of the meander structure of the Ballooning coils. The 4 lines are described by the following equations³¹:

$$R_y(\phi_{\text{eval}}) \cdot \begin{pmatrix} x_0 + A \cdot \sin(d\theta) \\ y_0 - A \cdot \cos(d\theta) \\ \frac{\Delta x}{2} \end{pmatrix} =$$

$$\begin{pmatrix} \cos(\phi_{\text{eval}}) \cdot (x_0 + A \cdot \sin(d\theta)) + \sin(\phi_{\text{eval}}) \cdot (\frac{\Delta x}{2}) \\ y_0 - A \cdot \cos(d\theta) \\ -\sin(\phi_{\text{eval}}) \cdot (x_0 + A \cdot \sin(d\theta)) + \cos(\phi_{\text{eval}}) \cdot (\frac{\Delta x}{2}) \end{pmatrix} ,$$

$$R_y(\phi_{\text{eval}}) \cdot \begin{pmatrix} x_0 + \frac{\Delta x}{2} \cdot \sin(d\theta) \\ y_0 - \frac{\Delta x}{2} \cdot \cos(d\theta) \\ -A \end{pmatrix} =$$

³¹Here $\Delta x = 74.8$ mm is the width of the (quadratic) Ballooning coil.

$$\begin{aligned} & \begin{pmatrix} \cos(\phi_{\text{eval}}) \cdot (x_0 + \frac{\Delta x}{2} \cdot \sin(d\theta)) - \sin(\phi_{\text{eval}}) \cdot A \\ y_0 - \frac{\Delta x}{2} \cdot \cos(d\theta) \\ -\sin(\phi_{\text{eval}}) \cdot (x_0 + \frac{\Delta x}{2} \cdot \sin(d\theta)) - \cos(\phi_{\text{eval}}) \cdot A \end{pmatrix} , \\ & R_y(\phi_{\text{eval}}) \cdot \begin{pmatrix} x_0 - A \cdot \sin(d\theta) \\ y_0 + A \cdot \cos(d\theta) \\ -\frac{\Delta x}{2} \end{pmatrix} = \\ & \begin{pmatrix} \cos(\phi_{\text{eval}}) \cdot (x_0 - A \cdot \sin(d\theta)) + \sin(\phi_{\text{eval}}) \cdot (-\frac{\Delta x}{2}) \\ y_0 + A \cdot \cos(d\theta) \\ -\sin(\phi_{\text{eval}}) \cdot (x_0 - A \cdot \sin(d\theta)) + \cos(\phi_{\text{eval}}) \cdot (-\frac{\Delta x}{2}) \end{pmatrix} , \\ & R_y(\phi_{\text{eval}}) \cdot \begin{pmatrix} x_0 - \frac{\Delta x}{2} \cdot \sin(d\theta) \\ y_0 + \frac{\Delta x}{2} \cdot \cos(d\theta) \\ A \end{pmatrix} = \\ & \begin{pmatrix} \cos(\phi_{\text{eval}}) \cdot (x_0 - \frac{\Delta x}{2} \cdot \sin(d\theta)) + \sin(\phi_{\text{eval}}) \cdot A \\ y_0 + \frac{\Delta x}{2} \cdot \cos(d\theta) \\ -\sin(\phi_{\text{eval}}) \cdot (x_0 - \frac{\Delta x}{2} \cdot \sin(d\theta)) + \cos(\phi_{\text{eval}}) \cdot A \end{pmatrix} \end{aligned}$$

with $A \in [-\frac{\Delta x}{2}, \frac{\Delta x}{2}]$.

A.3 Calculation of the B-coil area

The area of the B-coils can be calculated by the difference of the cone mantle surfaces, M_{min} and M_{max} , where the B-coils lie. The surfaces M_{min} and M_{max} are

$$M_{\text{min}} = \pi R_{\text{min}} s_{\text{min}}$$

$$M_{\text{max}} = \pi R_{\text{max}} s_{\text{max}}$$

where R_{min} and R_{max} are the major radial coordinates of the cone mantle surfaces and s_{min} and s_{max} are the cone mantle lines which are calculated according to

$$s_{\text{min}} = \sqrt{h_{\text{min}}^2 + R_{\text{min}}^2} \text{ or rather } s_{\text{max}} = \sqrt{h_{\text{max}}^2 + R_{\text{max}}^2} ,$$

where the heights h_{min} and h_{max} are calculated with the help of the ray theorem:

$$\frac{R_{\text{min}}}{R_{\text{max}}} = \frac{h_{\text{min}}}{h_{\text{max}}} \quad (\text{A.1})$$

and the known difference

$$\Delta h = h_{\text{max}} - h_{\text{min}} , \quad (\text{A.2})$$

so that

$$h_{\text{min}} = \frac{\Delta h}{\frac{R_{\text{max}}}{R_{\text{min}}} - 1}$$

and h_{max} can be calculated by using equation A.2. The area of the B-coils is then

$$A_{\text{Bcoil}} = \frac{\Delta\phi_{\text{Bcoil}}}{2\pi} \cdot (M_{\text{max}} - M_{\text{min}}) ,$$

where $\Delta\phi_{\text{Bcoil}}$ is the toroidal expansion of the B-coils. This results in an area of

$$A_{\text{Bu}} = 0.3386 \text{ m}^2$$

for the upper B-coils and

$$A_{\text{Bl}} = 0.3596 \text{ m}^2$$

for the lower B-coils.

Acronyms

AUG	ASDEX Upgrade: Tokamak in Garching near Munich
VDE	Vertical Displacement Event
PSL	Passive Stabilisation Loop: copper structure to mitigate VDEs
LFS	Low Field Side: outboard side of a tokamak
HFS	High Field Side: inboard side of a tokamak
MHD	magnetohydrodynamic
NTM	Neoclassical Tearing Modes
FEM	Finite Element Method
ECE	Electron Cyclotron Emission spectroscopy
SXR	Soft X-Ray
SOL	Scrape-Off Layer
TF	Toroidal Field
LOS	Line of Sight
ELM	Edge Localised Mode
H-mode	High confinement mode
NBI	Neutral Beam Injection
FFT	Fast Fourier Transform

Symbols

Variable	Explanation
$\mathbf{j}_{\text{pert,cyl}}$	perturbation current density in a periodic cylinder
\mathbf{j}_{pert}	total perturbation current density in a torus
$\mathbf{j}_{\text{pert}}^{(m,n)}$	(m, n) component of \mathbf{j}_{pert}
$\tilde{a}^{(m,n)}$	complex amplitude of $\mathbf{j}_{\text{pert}}^{(m,n)}$
$a^{(m,n)}$	amplitude of $\mathbf{j}_{\text{pert}}^{(m,n)}$
$\varphi^{(m,n)}$	phase of $\mathbf{j}_{\text{pert}}^{(m,n)}$
$\tilde{B}_{\text{meas},k}$	complex amplitude of the measured perturbation field of coil k
$a_{\text{meas},k}$	amplitude of the measured perturbation field of coil k
$\varphi_{\text{meas},k}$	phase of the measured perturbation field of coil k
$\tilde{\mathbf{B}}_{\text{meas}}$	vector of complex amplitudes of the measured perturbation field of k coils
$\tilde{B}_{\text{sim},k}^{(m,n)}$	complex amplitude of the simulated perturbation field of coil k generated by $\mathbf{j}_{\text{pert}}^{(m,n)}$
$a_{\text{sim},k}^{(m,n)}$	amplitude of the simulated perturbation field of coil k generated by $\mathbf{j}_{\text{pert}}^{(m,n)}$
$\varphi_{\text{sim},k}^{(m,n)}$	phase of the simulated perturbation field of coil k generated by $\mathbf{j}_{\text{pert}}^{(m,n)}$
$\tilde{\mathbf{B}}_{\text{sim}}^{(m,n)}$	vector of complex amplitudes of the simulated perturbation field of k coils generated by $\mathbf{j}_{\text{pert}}^{(m,n)}$
$\tilde{\mathbf{B}}_{\text{sim}}$	vector of complex amplitudes of the simulated perturbation field of k coils generated by \mathbf{j}_{pert}
$\tilde{\mathbf{a}}$	vector of complex amplitudes $\tilde{a}^{(m,n)}$

References

- [1] S. Hühn, “Albert Einstein: Die besten Zitate und Weisheiten.”
- [2] H. A. Bethe, “Energy production in stars,” *Physical Review*, vol. 55, no. 5, pp. 434–456, 1939.
- [3] E. G. Adelberger, A. García, R. G. H. Robertson, K. A. Snover, A. B. Balantekin, K. Heeger, M. J. Ramsey-Musolf, D. Bemmerer, A. Junghans, C. A. Bertulani, J.-W. Chen, H. Costantini, P. Prati, M. Couder, E. Uberseder, M. Wiescher, R. Cyburt, B. Davids, S. J. Freedman, M. Gai, D. Gazit, L. Gialanella, G. Imbriani, U. Greife, M. Hass, W. C. Haxton, T. Itahashi, K. Kubodera, K. Langanke, D. Leitner, M. Leitner, P. Vetter, L. Winslow, L. E. Marcucci, T. Motobayashi, A. Mukhamedzhanov, R. E. Tribble, K. M. Nollett, F. M. Nunes, T.-S. Park, P. D. Parker, R. Schiavilla, E. C. Simpson, C. Spitaleri, F. Strieder, H.-P. Trautvetter, K. Suemmerer, and S. Typel, “Solar fusion cross sections. ii. the pp chain and cno cycles,” *Rev. Mod. Phys.*, vol. 83, pp. 195–245, Apr 2011.
- [4] M. Kikuchi and Internationale Atomenergie-Organisation, eds., *Fusion physics*. No. 1562 in Publication / Division of Scientific and Technical Information, International Atomic Energy Agency, International Atomic Energy Agency, 2012.
- [5] S. Atzeni and J. Meyer-Ter-Vehn, *The Physics of Inertial Fusion: Beam Plasma Interaction, Hydrodynamics, Hot Dense Matter*, ch. 1 - Nuclear fusion reactions. Oxford: Clarendon Press, 2004.
- [6] J. Wesson and D. J. Campbell, *Tokamaks*. No. 149 in Oxford science publications, Oxford University Press, 4th ed ed., 2011.
- [7] S. E. Wurzel and S. C. Hsu, “Progress toward fusion energy breakeven and gain as measured against the Lawson criterion,” *Physics of Plasmas*, vol. 29, no. 6, p. 062103, 2022.
- [8] M. Kaufmann, *Plasmaphysik und Fusionsforschung*. Springer Fachmedien Wiesbaden, 2013.
- [9] K. Miyamoto, *Inertial Confinement*, pp. 337–352. Springer Berlin Heidelberg, 2005.
- [10] H. D. Blank, “Guiding center motion,” *Fusion Science and Technology*, vol. 45, no. 2, pp. 47–54, 2004.
- [11] V. M. A. Artigues, *Multi-Class and Cross-Tokamak Disruption Prediction using Shapelet-Based Neural Networks*. Phd thesis, TUM School of Computation, Information and Technology, Munich, 2023.
- [12] V. Igochine, ed., *Active Control of Magneto-hydrodynamic Instabilities in Hot Plasmas*, vol. 83 of *Springer Series on Atomic, Optical, and Plasma Physics*. Springer Berlin Heidelberg, 2015.
- [13] H. Zohm, *Magnetohydrodynamic Stability of Tokamaks*. Wiley-VCH, 2015.
- [14] U. Stroth, *Plasmaphysik: Phänomene, Grundlagen und Anwendungen*. Springer Berlin Heidelberg, 2018.

- [15] R. Schramm, A. Bock, E. Fable, J. Stober, M. Maraschek, M. Reisner, R. Fischer, H. Zohm, and the ASDEX-Upgrade Team, “Development and application of a predictive model for advanced tokamak scenario design,” *Nuclear Fusion*, vol. 64, no. 3, p. 036013, 2024.
- [16] S. Konovalov, P. Aleynikov, Y. Gribov, A. Ivanov, A. Kavin, R. Khayrutdinov, V. Leonov, V. Lukash, A. Loarte, S. Medvedev, *et al.*, “Characterization of runaway electrons in iter,” in *Proceedings of the 23rd International Conference on Fusion Energy, Daejeon*, 2010.
- [17] ITER Physics Expert Group on Disruptions, Plasma Control, and MHD and ITER Physics Basis Editors, “Chapter 3: MHD stability, operational limits and disruptions,” *Nuclear Fusion*, vol. 39, no. 12, pp. 2251–2389, 1999.
- [18] P. De Vries, M. Johnson, B. Alper, P. Buratti, T. Hender, H. Koslowski, and V. Riccardo, “Survey of disruption causes at JET,” *Nuclear Fusion*, vol. 51, no. 5, p. 053018, 2011.
- [19] S. Günter, A. Gude, M. Maraschek, Q. Yu, and T. A. U. Team, “Influence of neo-classical tearing modes on energy confinement,” *Plasma Physics and Controlled Fusion*, vol. 41, no. 6, pp. 767–774, 1999.
- [20] W. Suttrop, K. Buchl, J. Fuchs, M. Kaufmann, K. Lackner, M. Maraschek, V. Mertens, R. Neu, M. Schittenhelm, M. Sokoll, and H. Zohm, “Tearing mode formation and radiative edge cooling prior to density limit disruptions in ASDEX upgrade,” *Nucl. Fusion*, vol. 37, no. 1, pp. 119–125, 1997.
- [21] V. Klevarová, H. Zohm, G. Pautasso, G. Tardini, R. McDermott, G. Verdoolaege, J. Snipes, P. C. D. Vries, M. Lehnen, the EUROfusion MST1 team, and the ASDEX Upgrade team, “Validation of a tearing mode locking model using a database of disruptive plasmas at ASDEX upgrade,” *Plasma Phys. Control. Fusion*, vol. 62, no. 2, p. 025024, 2020.
- [22] A. Gude, M. Maraschek, V. Igochine, B. Sieglin, M. Willensdorfer, and H. Zohm, “Phase relation between rotating phase locked (2, 1) and (3, 1) tearing modes in ASDEX upgrade,” *Plasma Physics and Controlled Fusion*, vol. 63, no. 4, p. 045018, 2021.
- [23] J. M. Greene and J. L. Johnson, “Interchange instabilities in ideal hydromagnetic theory,” *Plasma Physics*, vol. 10, no. 8, pp. 729–745, 1968.
- [24] J. Puchmayr, M. Dunne, and E. Strumberger, “An intuitive form of the energy functional for resistive plasma perturbations,” *Journal of Plasma Physics*, vol. 88, no. 5, p. 905880512, 2022.
- [25] R. Fitzpatrick, *Tearing Mode Dynamics in Tokamak Plasmas*. IOP Publishing, 2023.
- [26] G. Bateman, *MHD instabilities*. Cambridge, Mass. : MIT Press, 1978.
- [27] P. H. Rutherford *et al.*, “Nonlinear growth of the tearing mode,” *Physics of Fluids*, vol. 16, no. 11, p. 1903, 1973.
- [28] H. P. Furth, P. H. Rutherford, and H. Selberg, “Tearing mode in the cylindrical tokamak,” *The Physics of Fluids*, vol. 16, no. 7, pp. 1054–1063, 1973.
-

- [29] M. Schittenhelm and H. Zohm, “Analysis of coupled MHD modes with mirnov probes in ASDEX upgrade,” *Nuclear Fusion*, vol. 37, no. 9, pp. 1255–1270, 1997.
- [30] M. Schittenhelm, *Investigation of tearing modes in asymmetric elongated plasmas in the ASDEX Upgrade tokamak*. Phd thesis, 1995.
- [31] W. D. D’haeseleer, W. N. G. Hitchon, J. D. Callen, and J. L. Shohet, *Flux Coordinates and Magnetic Field Structure*. Springer Berlin Heidelberg, 1991.
- [32] V. G. Merezkin, “Structure of the magnetic-field perturbations in the disruptive instability in the t-6 tokamak,” *Soviet Journal of Plasma Physics*, 1978.
- [33] P. J. Mc Carthy and ASDEX Upgrade Team, “Identification of edge-localized moments of the current density profile in a tokamak equilibrium from external magnetic measurements,” *Plasma Physics and Controlled Fusion*, vol. 54, no. 1, p. 015010, 2012.
- [34] R. Fischer and ASDEX Upgrade Team, “Coupling of the flux diffusion equation with the equilibrium reconstruction at asdex upgrade,” *Fusion Science and Technology*, vol. 69, no. 2, pp. 526–536, 2016.
- [35] V. Igochine, S. Günter, M. Maraschek, and T. A.U. Team, “Investigation of complex MHD activity by a combined use of various diagnostics,” *Nuclear Fusion*, vol. 43, no. 12, pp. 1801–1812, 2003.
- [36] E. Strumberger and S. Günter, “CASTOR3D: linear stability studies for 2D and 3D tokamak equilibria,” *Nuclear Fusion*, vol. 57, no. 1, p. 016032, 2017.
- [37] A. G. Peeters, “The bootstrap current and its consequences,” *Plasma Physics and Controlled Fusion*, vol. 42, no. 12, pp. B231–B242, 2000.
- [38] H. Zohm, G. Gantenbein, F. Leuterer, M. Maraschek, E. Poli, L. Urso, and the ASDEX Upgrade Team, “Control of NTMs by ECCD on ASDEX upgrade in view of ITER application,” *Plasma Physics and Controlled Fusion*, vol. 49, no. 12, pp. B341–B347, 2007.
- [39] R. Fitzpatrick, “Helical temperature perturbations associated with tearing modes in tokamak plasmas,” *Physics of Plasmas*, vol. 2, no. 3, pp. 825–838, 1995.
- [40] O. Sauter, R. J. La Haye, Z. Chang, D. A. Gates, Y. Kamada, H. Zohm, A. Bondeson, D. Boucher, J. D. Callen, M. S. Chu, T. A. Gianakon, O. Gruber, R. W. Harvey, C. C. Hegna, L. L. Lao, D. A. Monticello, F. Perkins, A. Pletzer, A. H. Reiman, M. Rosenbluth, E. J. Strait, T. S. Taylor, A. D. Turnbull, F. Waelbroeck, J. C. Wesley, H. R. Wilson, and R. Yoshino, “Beta limits in long-pulse tokamak discharges,” *Physics of Plasmas*, vol. 4, no. 5, pp. 1654–1664, 1997.
- [41] A. H. Glasser, J. M. Greene, and J. L. Johnson, “Resistive instabilities in general toroidal plasma configurations,” *The Physics of Fluids*, vol. 18, no. 7, pp. 875–888, 1975.
- [42] H. R. Wilson, M. Alexander, J. W. Connor, A. M. Edwards, D. Gates, O. Grüber, R. J. Hastie, C. C. Hegna, T. C. Hender, R. J. L. Haye, L. L. Lao, A. W. Morris, C. M. Roach, E. J. Strait, T. S. Taylor, M. Valovic, and H. Zohm, “The collisionality dependence of tokamak -limits,” *Plasma Physics and Controlled Fusion*, vol. 38, no. 12, pp. A149–A163, 1996.
-

- [43] R. Fitzpatrick, “Interaction of tearing modes with external structures in cylindrical geometry (plasma),” *Nuclear Fusion*, vol. 33, no. 7, pp. 1049–1084, 1993.
- [44] H. Zohm, “Stabilization of neoclassical tearing modes by electron cyclotron current drive,” *Physics of Plasmas*, vol. 4, no. 9, pp. 3433–3435, 1997.
- [45] S. Fietz, *Influence of plasma rotation on tearing mode stability on the ASDEX Upgrade Tokamak*. PhD thesis, Ludwig-Maximilians-Universität München, December 2013.
- [46] V. Klevarová, *Multi-device study of characteristics of disruptive magnetohydrodynamic modes in tokamaks*. PhD thesis, Ludwig-Maximilians-Universität München, October 2020.
- [47] M. Maraschek, S. Fietz, A. Gude, S. Günter, R. Koslowski, K. Lackner, K. Lüders, T. Lunt, G. Pautasso, E. Strumberger, *et al.*, “Measurement and impact of the $n=1$ intrinsic error field at asdex upgrade,” in *40th EPS Conference on Plasma Physics*, European Physical Society, 2013.
- [48] V. Igochine, P. Piovesan, I. Classen, M. Dunne, A. Gude, P. Lauber, Y. Liu, M. Maraschek, L. Marrelli, R. Mc Dermott, M. Reich, D. Ryan, M. Schneller, E. Strumberger, W. Suttrop, G. Tardini, and H. Zohm, “MHD limits and plasma response in high-beta hybrid operations in ASDEX upgrade,” *Nuclear Fusion*, vol. 57, no. 11, p. 116027, 2017.
- [49] R. J. La Haye, R. Fitzpatrick, T. C. Hender, A. W. Morris, J. T. Scoville, and T. N. Todd, “Critical error fields for locked mode instability in tokamaks,” *Physics of Fluids B: Plasma Physics*, vol. 4, no. 7, pp. 2098–2103, 1992.
- [50] R. Sweeney, W. Choi, M. Austin, M. Brookman, V. Izzo, M. Knolker, R. La Haye, A. Leonard, E. Strait, F. Volpe, and The DIII-D Team, “Relationship between locked modes and thermal quenches in DIII-d,” *Nuclear Fusion*, vol. 58, no. 5, p. 056022, 2018.
- [51] B. Tobias, M. Chen, I. G. J. Classen, C. W. Domier, R. Fitzpatrick, B. A. Grierson, N. C. Luhmann, C. M. Muscatello, M. Okabayashi, K. E. J. Olofsson, and C. Paz-Soldan, “Rotation profile flattening and toroidal flow shear reversal due to the coupling of magnetic islands in tokamaks,” *Physics of Plasmas*, vol. 23, no. 5, p. 056107, 2016.
- [52] J. S. Kim, D. H. Edgell, J. M. Greene, E. J. Strait, and M. S. Chance, “MHD mode identification of tokamak plasmas from mirnov signals,” *Plasma Physics and Controlled Fusion*, vol. 41, no. 11, pp. 1399–1420, 1999.
- [53] F. Klossek, “Generic determination of rotating and locked mhd mode amplitudes on asdex upgrade,” Master’s thesis, LMU Munich, Munich, Germany, April 2020.
- [54] J. Gernhardt, *Magnetic Diagnostic on ASDEX Upgrade with Internal and External Pick-up Coils*. Bericht / 1: Bericht, Max-Planck-Inst. für Plasmaphysik, 1992.
- [55] L. Giannone, R. Fischer, A. Kappatou, G. Tardini, M. Weiland, C. Angioni, E. Fable, M. Griener, R. McDermott, B. Sieglin, A. Jansen Van Vuuren, R. Bilato, M. Dunne, A. Gude, A. Kallenbach, J. Kurz, M. Maraschek, D. Rittich, F. Ryter, P. Schneider, K. Schuhbeck, U. Stroth, H. Zohm, and The Asdex
-

- Upgrade Team, “Measurements and modelling of diamagnetic flux in ASDEX upgrade,” *Nuclear Fusion*, vol. 61, no. 6, p. 066021, 2021.
- [56] W. Suttrop, “Design of in-vessel saddle coils for MHD control in ASDEX upgrade,” *35th EPS Conference on Plasma Phys.*, vol. ECA Vol.32D, pp. P-4.075, 2008.
- [57] F. Wagner, G. Becker, K. Behringer, D. Campbell, A. Eberhagen, W. Engelhardt, G. Fussmann, O. Gehre, J. Gernhardt, G. V. Gierke, G. Haas, M. Huang, F. Karger, M. Keilhacker, O. Klüber, M. Kornherr, K. Lackner, G. Lisitano, G. G. Lister, H. M. Mayer, D. Meisel, E. R. Müller, H. Murmann, H. Niedermeyer, W. Poschenrieder, H. Rapp, H. Röhr, F. Schneider, G. Siller, E. Speth, A. Stäbler, K. H. Steuer, G. Venus, O. Vollmer, and Z. Yü, “Regime of improved confinement and high beta in neutral-beam-heated divertor discharges of the ASDEX tokamak,” *Physical Review Letters*, vol. 49, no. 19, pp. 1408–1412, 1982.
- [58] H. Zohm, “Edge localized modes (ELMs),” *Plasma Physics and Controlled Fusion*, vol. 38, no. 2, pp. 105–128, 1996.
- [59] P. Dular, C. Geuzaine, F. Henrotte, and W. Legros, “A general environment for the treatment of discrete problems and its application to the finite element method,” *IEEE Trans. Magn.*, vol. 34, no. 5, pp. 3395–3398, 1998.
- [60] Y. Okumoto, Y. Takeda, M. Mano, and T. Okada, eds., *Design of Ship Hull Structures*. Springer Berlin Heidelberg, 2009.
- [61] J. Dankert and H. Dankert, *Technische Mechanik: Statik, Festigkeitslehre, Kinetik/Kinetik; mit 128 Übungsaufgaben, zahlreichen Beispielen und weiteren Abbildungen im Internet*. Lehrbuch, Springer Vieweg, 7., erg. Aufl ed., 2013.
- [62] A. Hrennikoff, “Solution of problems of elasticity by the framework method,” *Journal of Applied Mechanics*, vol. 8, no. 4, pp. A169–A175, 1941.
- [63] R. Courant, “Variational methods for the solution of problems of equilibrium and vibrations,” *Bulletin of the American Mathematical Society*, vol. 49, pp. 1–23, 1943.
- [64] D. Mchenry, “A LATTICE ANALOGY FOR THE SOLUTION OF STRESS PROBLEMS,” *Journal of the Institution of Civil Engineers*, vol. 21, no. 2, pp. 59–82, 1943.
- [65] W. Prager and J. L. Synge, “Approximations in elasticity based on the concept of function space,” *Quarterly of Applied Mathematics*, vol. 5, no. 3, pp. 241–269, 1947.
- [66] J. L. Synge and W. C. Rheinboldt, “The hypercircle in mathematical physics,” *Physics Today*, vol. 10, no. 10, pp. 45–46, 1957.
- [67] R. W. Clough, “The finite element method in plane stress analysis,” in *The Finite Element Method in Plane Stress Analysis*, 1960.
- [68] W. K. Liu, S. Li, and H. S. Park, “Eighty years of the finite element method: Birth, evolution, and future,” *Archives of Computational Methods in Engineering*, vol. 29, no. 6, pp. 4431–4453, 2022.
-

- [69] W. Ritz, “Über eine neue Methode zur Lösung gewisser Variationsprobleme der mathematischen Physik.,” *Journal für die reine und angewandte Mathematik*, vol. 1909, no. 135, pp. 1–61, 1909.
- [70] B. A. Finlayson and L. E. Scriven, “The method of weighted residuals — a review,” *Appl. Mech. Rev.*, vol. 19, no. 9, pp. 735–748, 1966.
- [71] P. D. Lax and A. N. Milgram, *IX. Parabolic Equations*, pp. 167–190. Princeton University Press, 1955.
- [72] J. N. Reddy and D. K. Gartling, *The finite element method in heat transfer and fluid dynamics*. CRC series in computational mechanics and applied analysis, CRC Press, 3rd ed ed., 2010. OCLC: ocn213318287.
- [73] G. Meunier, ed., *The finite element method for electromagnetic modeling*. ISTE ; Wiley, 2008. OCLC: ocn180989643.
- [74] D. Raabe, “9 - finite elements for microstructure evolution,” in *Computational Materials Engineering* (K. G. JANSSENS, D. RAABE, E. KOZESCHNIK, M. A. MIODOWNIK, and B. NESTLER, eds.), pp. 317–333, Burlington: Academic Press, 2007.
- [75] D. Dinkler and U. Kowalsky, *Introduction*, pp. 3–17. Springer Fachmedien Wiesbaden, 2024.
- [76] E. Creusé, P. Dular, and S. Nicaise, “About the gauge conditions arising in finite element magnetostatic problems,” *Computers & Mathematics with Applications*, vol. 77, no. 6, pp. 1563–1582, 2019.
- [77] A. A. Rodríguez and A. Valli, *Eddy Current Approximation of Maxwell Equations*, vol. 4 of *MS&A*. Springer Milan, 2010.
- [78] V. Girault and P.-A. Raviart, *Finite Element Methods for Navier-Stokes Equations*, vol. 5 of *Springer Series in Computational Mathematics*. Springer Berlin Heidelberg, 1986.
- [79] C. Geuzaine, F. Henrotte, E. Marchandise, J.-F. Remacle, P. Dular, and R. Sabariego, “Onelab: Open numerical engineering laboratory,” *Proceedings of the 7th European Conference on Numerical Methods in Electromagnetism (NUMELEEC2012)*, 01 2012.
- [80] C. Geuzaine and J. Remacle, “Gmsh: A 3-d finite element mesh generator with built-in pre- and post-processing facilities,” *Numerical Meth Engineering*, vol. 79, no. 11, pp. 1309–1331, 2009.
- [81] M. Bauer, “Three-dimensional finite element modelling of magnetic measurements of tearing modes in asdex upgrade,” Master’s thesis, LMU Munich, Munich, Germany, May 2021.
- [82] H. Preis, “Die Berechnung von Wirbelströmen und magnetischen Kräften in Kernfusions-Experimenten,” *Archiv für Elektrotechnik*, vol. 69, no. 5, pp. 359–365, 1986.
- [83] ASDEX Upgrade Project Team, *ASDEX Upgrade project proposal phase II. Bericht / 1. Bericht*, Max-Planck-Inst. für Plasmaphysik, 1983.
-

Acknowledgements

First of all, I would like to express my heartfelt gratitude to my academic supervisor, **Hartmut Zohm**, who not only guided me from meteorology to plasma physics and thus to IPP, but also helped me constantly with valuable discussions. Thank you for always taking the time and supporting me!

A very big thank you also goes to my daily supervisor **Marc Maraschek**, who I could always ask for help and who was always there to give me advice and support, as well as **Anja Gude**, who officially had no supervisory role, but who still gave me great support. Your time, advice and help are highly appreciated.

I am deeply grateful to **Wolfgang Suttrop**, from whom I learned a lot. He helped me setting up the FEM model and answered every question I had about GetDP, FEM or even completely different topics. Many thanks also to **Louis Giannone** and **Bernhard Sieglin** for your support and discussions on a wide range of topics. I would also like to thank **Matthias Hölzl** not only for the exciting race during the company outing, but also for answering my questions about tearing modes and for introducing me to JOREK and helping me run it. I wish to extend my gratitude to **Erika Strumberger** for helpful discussions about sidebands and to **Irene Zammuto** for answering every question about the structure of AUG. I am grateful to **Valentin Igochine** for the discussions and explanations about tearing modes and to **Gabriella Pautasso** for the discussions about the resistive time scale of the wall.

I would also like to thank **Gerald Sellmair**, **Horst Eixenberger** and the **team of the electronics workshop** for helping us with measurements on various coils and answering all my questions.

I would also like to express my gratitude to **Mike Dunne** for explaining the equilibrium reconstruction, to **Rainer Fischer** for calculating the IDE shotfiles, to **Christoph Fuchs** for helping me with all sorts of IT issues and to **Matthias Wilensdorfer** for the special settings of the ECE diagnostic for our discharges.

I have always felt very comfortable at IPP and would therefore like to express my sincere thanks to all IPP employees, with whom I was able to spend a great time at Ringberg or even just exchanged a quick smile in the corridor. Many thanks especially to the **lunch group** (Felix Albrecht, Michael Bergmann, Tabea Gleiter, Michael Griener, Vanessa Harnisch, Paul Heinrich, Manuel Herschel, Lea Hollendonner, Sebastian Hörmann, Joey Kalis, Felix Klossek, Simon Krumm, David Kulla, Hannah Lindl, Michaela Mayer, Alessandro Mancini, Jonas Puchmayr, Raphael Schramm, Christian Schuster, Michael Sieben, Fabian Solfronk, Bojana Stefanoska, Beatrice Tosto, Markus Weiland, Daniel Wendler and Benedikt Zimmermann) for the great atmosphere. Above all, I would like to thank **Tabea Gleiter** and **Jonas Puchmayr**, who have always supported me both professionally and personally, for which I am incredibly grateful to you! I am profoundly thankful to **Felix Klossek**, who always took the time to answer my questions, to **David Kulla**, who was the best office mate you could wish for, and to **Daniel Wendler**, who always encouraged me.

Many thanks also to everyone I have not mentioned by name. The list would just be way too long. Even though I never really planned to do a PhD, I really enjoyed the time with all of you and I definitely do not regret it! I am proud to have been part of the AUG team!